Fatigue damage accumulation under torsion and non-proportional push-pull interruption loading.

WHEELHOUSE, Keith.

Available from the Sheffield Hallam University Research Archive (SHURA) at:

http://shura.shu.ac.uk/20522/

A Sheffield Hallam University thesis

Fatigue Damage Accumulation under Torsion and Non-Proportional Push-Pull Interruption Loading

Keith Wheelhouse

BEng (Hons) C.Eng. MIMechE

A thesis submitted in partial fulfilment of the
requirements of
Sheffield Hallam University
for the degree of Doctor of Philosophy

January 2002

ProQuest Number: 10701169

All rights reserved

INFORMATION TO ALL USERS
The quality of this reproduction is dependent upon the quality of the copy submitted.

In the unlikely event that the author did not send a complete manuscript
and there are missing pages, these will be noted. Also, if material had to be removed,
a note will indicate the deletion.
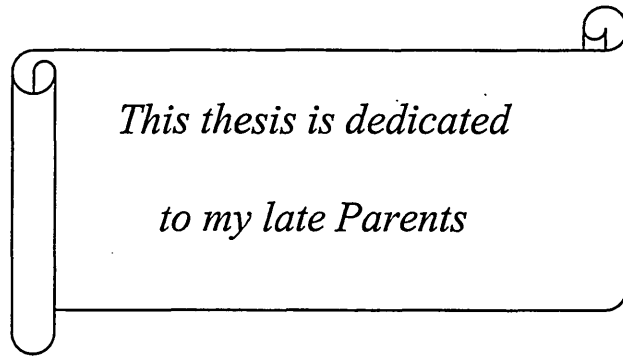
This thesis is dedicated

to my late Parents

Preface

I declare that this thesis is based on the findings of research carried out in the School of Engineering, Sheffield Hallam University.

The content of the thesis is original except where specific references are made to other work.

No part of this thesis has been submitted to any other University.

Keith Wheelhouse
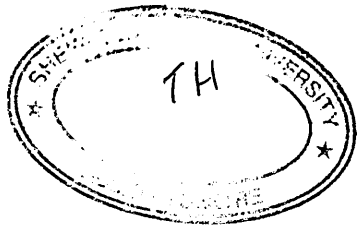
Acknowledgements

I would like to express my gratitude to Sheffield Hallam University for the opportunity to undertake the postgraduate study and the financial support given. My past working experience in the mining industry was associated with the failure of engineering components, where fatigue and fracture played a dominant role and therefore this research study was particularly interesting to me, although as many have experienced before it was very demanding requiring a lot of personal dedication.

I am particularly indebted to my Director of Studies Dr. U. S. Fernando for his guidance and constructive criticism to keep me focused on the critical issues of the research work. I am also grateful for the advice and assistance from my other supervisors Mr. D. E. Eaton and Professor J. D. Atkinson during the course of this work.

I would like to express my thanks to Mr. K. Wright, Mr R Wainwright, Mr. B. Didsbury, Mr. R. Tingle, Mr. M. Jackson and Mr. J. Ross-Smith for their assistance with the laboratory apparatus and the manufacture of test equipment. I express my thanks also to Mr. P. Slingsby and Mr. J. Muirhead for their help in the Materials Research Institute laboratories and use of the SEM equipment.

Finally, I would like to thank my wife for her support and encouragement during the course of my work.

The effects of non-proportional loading on the torsional fatigue life

for a medium carbon steel

K. Wheelhouse U. S. Fernando and D. E. Eaton
(School of Engineering, Sheffield Hallam University)

Presented at the Sixth International Conference on

Biaxial/Multiaxial Fatigue & Fracture

25-28 June 2001 - Lisbon Portugal

The effects of push-pull interruption on the torsional fatigue life

of medium carbon steel

K. Wheelhouse and U. S. Fernando
(School of Engineering, Sheffield Hallam University)

Presented at the International Conference - Life Assessment and

Management for Structural components

6-9 June 2000 - Kiev, Ukraine

CONTENTS

Chapter 3

Chapter 6

Chapter 7

Appendices

Appendix 1

Taylor Hobson Surface Measuring Machine

Appendix 2

Societe Genovoise MU-214B Universal Measuring Machine

Appendix 3

Detail design drawings of components

Appendix 4

Computer Program for Multi-Phase Loading

Appendix 5

Model computed results for push-pull and torsion for constant amplitude loading

Appendix 6

Model computed results multi-phase loading $\Delta\sigma$ (600 MPa and 640 MPa)

Appendix 7

Model computed results for multi-phase loading $\Delta\sigma$ (760 MPa and 820 MPa)

Abstract

A new testing facility for fully reversed tension-torsion high cycle fatigue testing has been designed. The specimens used for the test programme were solid and made from a medium carbon steel. The test programme involved a tension-torsion multiaxial non-proportional loading sequence i.e. fully reversed torsion followed by a push-pull load interruption and then the continuation of the same torsion loading to failure. The push-pull load interruption represented a significantly low damage i.e. 4% damage according to Miner's linear damage theory, and was applied after different prior torsion cycle ratios. The tests were conducted with various interruption stress amplitudes all of which had fatigue lifetimes in the high cycle fatigue region.

The torsion fatigue life was found to change significantly due to the application of push-pull load interruption which was considered to cause only a minor damage due to Miner's rule. Miner's linear damage theory cannot account for the predicted cumulative fatigue damage ($\Sigma n/N_f$) for the push-pull interrupted torsion fatigue loading sequences used in the current test programme. The fatigue life was markedly enhanced when the interruption was applied at an early stage of torsion loading whilst the effect was less prominent when the interruption was applied at a later stage of torsion loading. At higher interruption stress amplitudes the torsion fatigue lifetime was reduced considerably and the damage summation was well below the unity predicted by the Miner's rule. The inability to predict damage accumulation by Miner's rule can be attributed to the complexity in the crack growth associated with the application of push-pull interruption.

Crack growth equations to represent microstructural short crack (MSC) and the physically small crack (PSC) growth were determined for the material of the form;

$$\text{MSC} - \quad da/dN = C_m(d_i - a) \quad \dots\dots\dots\dots\dots\dots\dots(1)$$

and

$$\text{PSC} - \quad da/dN = C_p\, a - D \quad \dots\dots\dots\dots\dots\dots\dots(2)$$

Material parameters for the models were derived using torsion and uniaxial constant amplitude fatigue S-N data, no crack coalescence, branching or re-initiation was considered.

The crack growth model was able to predict the fatigue life in loading cases which were dominated by an uninterrupted crack growth. However, such a model was shown to significantly underestimate the torsion fatigue life in situations where the fatigue life was affected by secondary crack initiation due to the push-pull load interruption.

Notation

a = crack length

a_o = initial crack length (or surface roughness)

a_s = short crack length

a_t = transition crack length between short and long cracks

a_f = failure crack length

da/dN = crack growth rate

d = microstructural length parameter

A, B, D, m, n = material constants

α, β = constants

C, m = empirical constants

n = number of cycles

N_f = number of cycles to failure

$\Delta\sigma$ = normal stress range

$\Delta\sigma_{eq}$ = equivalent normal stress range

$\Delta\tau$ = shear stress range

$\Delta\tau_{eq}$ = equivalent shear stress range

ΔT = torque range

$\Delta\varepsilon_p$ = plastic strain range

ΔK = stress intensity factor range

ΔKth = threshold stress intensity factor range

r_p = plastic zone size

$r_{p(s)}$ = plastic zone for microstructural short crack (MSC)

R = stress ratio

Chapter 1

Introduction

The fatigue behaviour of an engineering component can be very difficult to resolve under multiaxial loading, especially where the influence of crack-load interaction has a significant effect on fatigue life. Why therefore should research and expenditure be committed to understand the complexity of fracture under such conditions. Many answers could obviously be given, but now probably none are more pertinent than to seek sustainability and the efficient use of materials and energy.

The sustainability and efficient use of materials and energy is an issue emphasised strongly today, because of the noticeable increase in natural disasters globally that are associated with climatic change. The uncertainties surrounding this phenomenon have promoted increasing pressure internationally, to limit environmental damage and reduce the use of natural resources. Engineering is at the forefront of this requirement since the economies of the developed and developing countries are driven by technology. The European Council for Automotive Research (EUCAR) recently published a summary document outlining the need to aim for high efficiency of energy use, by promoting intensive research into major improvements in all power train and vehicle characteristics. This is obviously an objective in principle that can be applied to most industries and supporting institutions that undertake research for whatever application.

The research programme undertaken here which involves fatigue damage assessment under multiaxial loading for a common engineering material is one such area of research that can play a vital role in understanding problems that can adversely affect the efficient use of engineering components. Substantiating that sustainability and fatigue although seemingly diverse terms are not inseparable, since endurance and fatigue failure are directly related in an engineering context.

Fatigue failure occurs by various mechanisms attributed to the many different applications of engineering components and structures. Where today, customer demands, competitiveness of the global work place, and the increasing sophistication of engineering designs have necessitated materials to be taken to further limits of endurance. Understandably failure of engineering components and structures over the years, has driven research to find answers to these problems. The results of that have promoted a greater understanding of fatigue behaviour that enables it to be largely controlled today, rather than be left to chance. Certainly different from the early experiences of fatigue damage where failures were not so predictable, but nevertheless these failures became a very important starting point on the 'long road' to understand fatigue behaviour.

Braithwaite mentioned the term 'fatigue' for the first time in 1845 [1], to describe the failure of engineering components according to Schutz [2]. Although the reported history of fatigue began in 1837 with a German mining engineer Albert [3], who carried out the first recorded study of metal fatigue, as a result of in service cage suspension chain failures. Since then to the present time there have been numerous fatigue failures that has demanded adequate explanations. None more so to me

personally than the fatigue failure of a winding engine brake rod that was responsible for the fatal injuries of 18 miners [4], as I was employed at that time in the mining industry and not so aware of the underlying dangers that fatigue presented. Also the events leading to very recent fatal train accident at Hadfield, reportedly caused by fatigue failure as a result of the so-called 'gauge corner cracking' of the rails, another fatigue mechanism that is still not fully understood [5].

Obviously the fatigue of critical engineering components can have devastating effects, but in more general terms fatigue has been a problem for over 150 years and continues to be so. However, despite some significant advances over the years, there are still several problem areas [6], especially engineering components subjected to complex loading systems. Conditions that can influence the fatigue behaviour considerably, which is a feature of the research work presented here.

The current work relates to an investigation of torsion-tension multiaxial non-proportional sequential loading of how the torsion fatigue lifetime and crack growth behaviour are affected, when the specimen is subjected to a push-pull load interruption at various stages of the torsion fatigue life. It is widely accepted that certain changes in the stress/strain field can affect the fatigue life of an engineering component. The degree of influence is dependent on the interactive nature of the different loading and the effect it has on crack growth. But, there are still unanswered questions of how torsion fatigue life is affected where multiaxial loading is concerned, since the effects from the variability of loading and modes of loading have not been fully investigated and are as yet not complete.

Engineers however, need information on how different loading systems affect the integrity of engineering components. In some instances the applied loading may create the conditions for assisting a dominant crack to progress more easily or to the contrary and assist in the retardation of crack growth. The micro-mechanisms of fatigue crack growth are generally complex as a result of changes in the stress/strain state, conditions that are frequently encountered in engineering components. This is especially so for high cycle fatigue (HCF) where the growth of short cracks play a significant role in the fatigue life of engineering components. A specific case in question is the current work, which involves multiaxial and multi-phase loading conditions in the HCF regime.

The literature review examines how previous work has approached the problems of analysing fatigue crack growth under uniaxial and multiaxial loading and the summation of fatigue damage and how this may be considered to interact with the current work.

The main objectives of the test programme were,

1. To examine fatigue damage accumulation under multiaxial non-proportional multi-phase loading, which focuses on the effects on the torsion fatigue lifetime of specimens, as a result of a change in stress state by the introduction of a push-pull load interruption. The push-pull load interruption selected intentionally represents a significantly low fatigue damage i.e. 4% damage according to Miner's linear damage theory (LDR). But, more importantly what is the effect of the crack-load

4

interaction and how does this influence the summation fatigue damage compared to the LDR.

2. To design a new experimental facility for applying the fully reversed torsion and push-pull loading, loading which could be applied individually or simultaneously which is discussed in Chapter 3.

3. To conduct constant amplitude and multi-phase tests as outlined in Chapter 3. Initially the fatigue characteristics of the material for pure torsion and pure push-pull fully reversed loading are determined. The multi-phase test programme involved multiaxial loading sequences of torsion (Phase1) followed by push-pull load interruption (Phase2) and then the continuation of the same Phase 1 torsion loading to failure (Phase 3). In total 33 tests are carried out, which includes 17 multi-phase tests. The material used for this research programme is 0.42% carbon steel to BS 970 080A42 and supplied as 25mm diameter cold finished bright bar manufactured to BS EN ISO 9002:1994.

4. To use crack growth models to obtain a best-fit to torsion constant amplitude S-N fatigue and develop the model to predict fatigue damage accumulation under push-pull and multi-phase loading as discussed in Chapter 5. The models represent two phases of crack growth, firstly, microstructural short crack (MSC) and secondly, physically small crack (PSC). MSC growth is the initial Stage I crack growth that is significantly influenced by the microstructure in addition to the loading condition, whereas the PSC growth is Stage II crack growth which is less sensitive to microstructural influences. The cumulative affect of these two

separate and distinctive crack growth behaviours reflect crack growth associated with the HCF regime, which is a feature of the current work.

5. To examine crack growth patterns found on the surface of specimens, the crack growth patterns of sectioned specimens and the examination of the fracture surfaces of specimens for the different multi-phase loading using a scanning electron microscope (SEM). The observations are discussed in Chapter 6.

It is concluded that the introduction of a push-pull load interruption can significantly affect the torsion fatigue life. The Miner's linear damage theory ($\Sigma n/N_f = 1$) was found to give non-conservative results for some of the non-proportional loading sequences used in the multi-phase test programme.

The crack growth model was capable of predicting the fatigue lifetimes of push-pull constant amplitude tests, and multi-phase tests for the more damaging loading sequences that encouraged uninterrupted crack growth. The crack growth model also gave conservative predictions for all the multi-phase loading tests carried out.

As discussed in Chapter 3 for the material, cracks were found to initiate in the softer ferrite grains whilst the stronger pearlite regions promoted the apparent retardation or arrest of Stage I crack growth creating non-propagating cracks.

The density of Stage I cracks significantly increased where crack growth was interrupted, whereas Stage I cracks were less densely populated, but, longer where crack growth was uninterrupted.

Chapter 2

Literature Review

2.1 Multiaxial Fatigue

Multiaxial fatigue is a term used to describe a fatigue process under a multiaxial state of stress where two or more principal stresses, of the stress state, vary with time. Whereas for uniaxial fatigue only one principal stress exists that varies with time. Therefore, the physical fatigue mechanisms involved with multiaxial fatigue and the analysis to account for crack growth can be more complex, since the nucleation of cracks may have different orientations and grow on different planes depending on the applied stress state. Although, the growth rate of cracks is considered one of the most important aspects of multiaxial fatigue crack growth since this is the determining factor for the endurance of an engineering component.

Fatigue behaviour in engineering components is predominantly controlled by a localised stress state at or near the surface which is almost always biaxial, as is the case for most structural components where most fatigue cracks propagate in biaxial stress or mixed mode conditions [7]. In some cases triaxial stress systems can be generated by the application of a high hydrostatic pressure, but, even in this case the stress normal to the surface is always a principal stress which provides simplification to stress analysis because two of the three shear stresses are zero [8] i.e the shear stresses in the surface plane are zero.

Machine components can experience a complex state of stress because generally they are not of simple geometry or as a result of multiaxial stress fields that develop due to the application of two or more loads which can be applied either simultaneously or in sequence. Such circumstances are still a cause for concern for designers who are confronted by 'real' life problems on industrial component [9]. Since multiaxial stress fields can result from some particular design feature that may include the presence and shape of notches on the component. For instance the stress at a constrained round notch in a thick plate that experiences plane strain conditions [8].

Multiaxial fatigue is concerned with the influence of the stress and strain state on particular fatigue fracture features such as the orientation of cracks, the direction of crack growth and the growth rate, and crack shape and how these affect the fatigue life. Therefore, fatigue behaviour under multiaxial loading is best understood by the examination of crack propagation mechanics, since it is arguably correct that the physical growth of cracks controls the accumulation of fatigue damage. The crack mechanistic approach is to focus on the mechanics of fracture and to describe engineering failures in terms of generation and growth of fatigue cracks.

2.2 Generation and Growth of Fatigue Cracks

2.2.1 Introduction

It is understandable that fatigue concepts developed from the 1950s involving the generation and growth of fatigue cracks have been widely accepted since cracks are a visible form of fatigue damage and are a precursor to failure. The understanding of

the fatigue process has been greatly enhanced by the development of various techniques to observe fatigue cracks, especially short fatigue cracks [10]. The advent of new technology has provided sophisticated tools and techniques which have enabled the measurement and observation of very small cracks of the order of $1\mu m$. De Lange [11] in 1964 used a plastic replica technique to study crack propagation, a method that is commonly used today. This technique has the uniqueness to measure several surface cracks on each replication, and can also refer crack length to the surrounding microstructure as well as observing crack interactions. Also, even though the method is somewhat protracted because the test machine has to be stopped periodically to take a replica and has the disadvantage of not being able to measure crack depth, its simplicity and affordability make it a very useful technique.

Other techniques such as electrical potential drop (PD) measurement [12] and acoustic emission (AE) [13] have the ability to continuously record crack growth during testing. However, the PD technique is not readily used for monitoring short crack growth (Stage I cracks) unlike the AE technique that has been widely developed over the last three decades and reportedly [13] can detect microscopic events in a material, crack initiation and propagation. AE is also claimed to be sensitive to frictional processes i.e. monitoring crack-face contact during crack closure, a process synonymous with torsion loading, but normally difficult to monitor.

Obviously differing crack measuring and observation techniques established over the years appear to be best suited for selective stages of crack development. For instance, for crack initiation, Haworth et al [14] used holographic techniques, and Baxter [15]

used laser beam technology, to observe topographic changes such as slip band development, microcracking and crack propagation. Fisher and Sherratt [16] used a highly sensitive eddy-current detection technique together with microscopic observations, and postulated the possibility of identifying a point in the fatigue life at which the rate of damage accumulation or microcrack growth increases very rapidly. More recently Doquet [17] examined the development of fatigue damage of thin tubular specimens by observing crack initiation mechanisms in torsion fatigue, using square metallic microgrids with a 5μm mesh size laid on the electropolished surface of the specimens. Where reportedly [17] the localised distortion of the microgrids clearly highlighted the grain boundary regions where slip intensifies to ensure strain compatibility between neighbouring grains.

However, fatigue in most engineering components is concerned with the birth of a fatigue crack from an origin at the surface or within the material and the progressive process of crack development. Forsyth [18] divided the fatigue fracture process into three distinct phases namely,

(1) Crack Initiation

(2) Stage I crack growth

(3) Stage II crack growth

2.2.2 Crack Initiation

Fatigue crack initiation in metals is a very complex process and depends largely on the microstructural properties of the material, the surrounding environment, loading conditions and the engineering constraints of the component geometry. However, the role of microstructure at this stage of crack development is considered of primary importance [19]. The more complex the microstructure, the more pronounced the effect on fatigue life, since the development of cracks by slip along crystallographic planes is influenced by the local differences in microstructure [20]. Therefore the time taken for the development of a micocrack to reach the macro crack stage will vary accordingly.

The initial effect from the application of constant low-medium stress amplitude in a ductile metal usually produces microscopic deformation of the metal surface. This is caused by atoms moving along particular crystallographic planes and is referred to as slip involving the movement of dislocations in crystals or grains in the material [21]. The dislocations are line defects in the metal lattice and their movement produces slip and interaction that are responsible for strain hardening and dislocation accumulation. Fatigue loading results in the formation of slip bands [18], orientation along slip plane (45° to tensile axis). These slip bands generally appear after a few cycles and broaden into persistent slip bands (PSB) [22]. The movement of dislocations intersecting the free surface of the material along slip bands, cause microscopic surface discontinuities which are known as extrusions or intrusions or slip band pits depending on the operative slip direction in relation to the metal surface [18] as shown schematically in Fig.2.1. Extrusions are thin bands, which are extruded out of the surface of the material, and intrusions are small crevices, which

11

penetrate into the surface of the material along planes of the maximum resolved shear stress.

Since surface grains are the only part of a polycrystalline structure that are not wholly restrained by adjoining grains they will therefore deform plastically more readily than the grains constrained in the body of the metal [20]. The reduced bulk constraint effect on these grains is the obvious place for the initiation of slip and usually this becomes the most vulnerable location for crack initiation in the largest grain. Although, difficulties in distinguishing some crack nuclei in slip bands may arise by the observation of surface micrographs alone and Neumann and Tonnessen [23] considered it to be very important to section specimens perpendicular to the original surface in order to detect crack nuclei reliably.
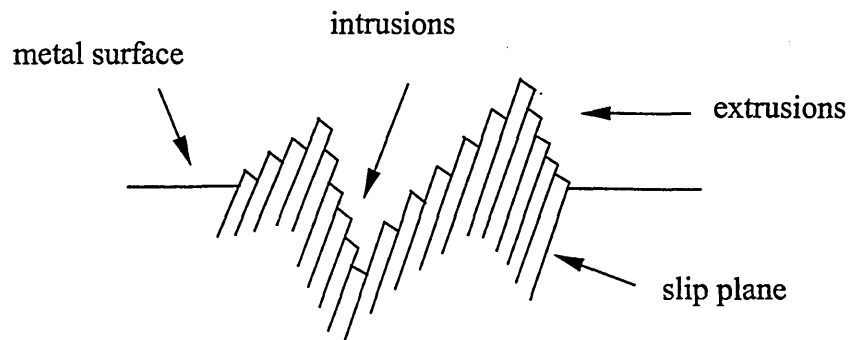
Fig. 2.1 Schematic representation of slip band formation - cyclic stress [18]

The mechanisms of crack initiation for high strength metals may not involve the formation of slip bands and crack initiation can occur at other sites such as grain boundaries and at discontinuities like inclusions, voids and second phase particles [24] [25] [26]. These discontinuities are weak spots or points of stress concentration

and are normally referred to as 'defects'. The debonding of inclusions from the matrix can also promote crack initiation, which is caused by the break down of the inclusion from the onset of fatigue cycling [24]. Although it is important to have metals free of inclusions to prevent crack initiation at these sites, the efforts to produce 'cleaner' metals to eliminate inclusions cannot increase the fatigue strength indefinitely since crack initiation in slip bands is still operative. Generally though in clean and sound ductile metals (metals clean enough to avoid major inclusions), which are subjected to low or intermediate stress amplitudes, the initiation of cracks usually occurs in localised slip bands within the single grain [27] [23].

In torsion loading it has been suggested that persistent slip bands do not intersect the free surface and extrusions and intrusions are not able to form in the same manner as for uniaxial loading. Kompek et al [28] conducted some torsion experiments on smooth specimens and observed almost no signs of deformation and suggested that the deformation process was very localised in well spaced out fatigue bands similar to that of fatigue in monotonic tension. Whereas in other tests [28] on notched specimens, slip bands were shown to form on the maximum shear planes at the root notch, coincident with the higher strain region.

The differences between tensile and torsion fatigue lives are very pronounced for some alloys and it is considered that purely mechanical reasons do not entirely explain these differences and that the fatigue lives may be affected by the different crack initiation mechanisms under torsion loading [17].

2.2.3 Stage I Crack Growth

There is probably universal acceptance that the onset of crack formation is generally by the deepening of the slip band groove by an atomic process of dislocation movement, with crack growth occurring in the slip plane, resulting from a shear dominant fracture mechanism. This mode of crack growth is termed Stage I crack growth after Forsyth [18]. Stage I cracks in a polycrystalline metal are considered to form on those planes aligned with the maximum shear-stress directions and are therefore controlled by the maximum shear strain range ($\Delta\gamma_{max}$) of the applied stress state [29].

The cracking mechanism of Stage I crack growth can persist for an appreciable proportion of the endurance. This can result in the formation of non-propagating cracks especially at stress levels below the fatigue limit, where Stage I cracks grow in relation to the extent of the localised plasticity of the order of a microstructural unit [30], but will eventually be arrested by a microstructural feature. Although, Miller *et al* [30] also found that Stage I cracks arrested at stress levels below the fatigue limit can have a significant effect on any subsequent damage accumulation at stress levels just above the fatigue limit. Stage I crack however can propagate below the air fatigue limit by extraneous factors such as aggressive environment [26] [59].

Stage I crack growth is also dependent on the grain size and the yield strength of the material for cracks developing in both smooth surfaces and notched components [31]. This is because small-grains introduce more physical barriers i.e. grain boundaries to restrict crack growth, since grain boundaries are positions of mis-orientation of slip systems, and materials with a higher yield strength the reverse plasticity required to propagate the crack is of a lesser extent [32].

The fatigue limit of smooth specimens can be considered to be the limit at which Stage I crack growth is contained by the strength of the microstructural barriers of the material. This microstructural-threshold reflects a boundary condition for the limit of propagation of cracks, where the stress levels are not sufficient to overcome the microstructural barriers of the material [33], and as a consequence cracks are arrested i.e. the crack growth rate $da/dN = 0$. Therefore, for such a crack to propagate a greater strain intensification at the crack tip is required for the subsequent transition to the next phase of crack growth referred to as Stage II crack growth.

2.2.4 Stage II Crack Growth

The transition to this next stage of crack growth is dependent on the magnitude of the maximum principal stress operating in the component or specimen in the region of the crack tip. This mode of crack growth represents what is considered a rational division from that of Stage I crack growth and is termed Stage II crack growth [18]. Consequently with the extension of crack length within the grains there is an increase in the stress intensity at the crack tip that favours the activation of new slip systems. The new shear planes associated with the crack advance are now not limited to the initial maximum shear planes previously existent in the surface grains. Unlike Stage I crack growth that is confined to only one active slip system the new slip system involves simultaneous or alternating flow along two separate slip planes [34], as shown in Fig 2.2.

The attendant crack growth process for Stage II crack growth continues with the increment of crack extension for each loading cycle. This new active slip system is

usually related to the formation of striations on the fracture surface in push-pull loading once stable crack growth occurs and their presence is proof that failure was fatigue dominant [35]. The microcrack transition from Stage I shear-dominated to Stage II normal stress-dominated occurs after attaining a length in excess of several grains [33] [36]. However, the precise dependence of this transition phenomenon on grain size, slip planarity and local microstructural detail is still not fully understood [37].

slip bands
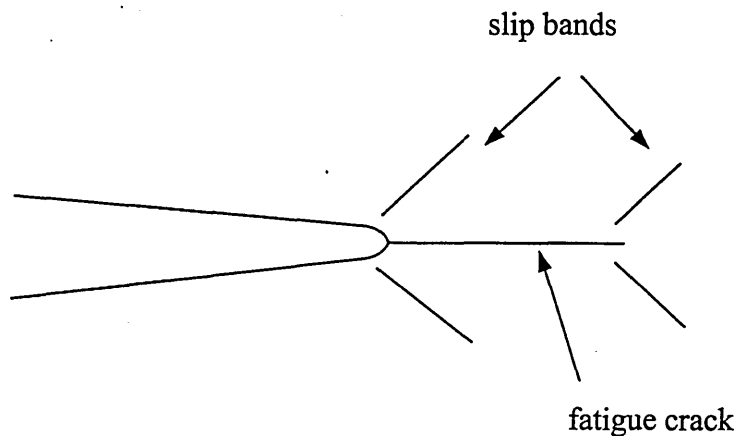
fatigue crack

Fig. 2.2 The idealisation of Stage II fatigue crack growth [34]

The length of time that Stage I cracks grow along slip planes before the transition to a Stage II crack is dependent on several factors, such as the applied strain range, strain biaxiality, environment effects and microstructural features [20]. Although when a fatigue crack nucleates at inclusions in high strength alloys, Stage I crack growth is not always apparent and the transition to Stage II crack growth can occur even within one-grain [38].

16

2.2.5 Multiaxial Fatigue Crack Growth Mechanisms

Since the present work involves complex loading conditions, the crack growth mechanisms associated with these loading systems need to be considered. Therefore, the development of multiaxial crack growth theories are examined, with the emphasis on multiaxial HCF which is a feature of this work.

The study of fatigue behaviour under combined stresses has been ongoing since the early part of the last century, culminating in a number of theories which present various criteria for predicting fatigue strength under complex stress-strain systems [39]. For HCF of ductile materials, the criteria most often used include the maximum shear theory or Tresca and the distortion energy criterion or Von Mises, whilst for brittle materials the Rankine principal stress criterion is used. Although these theories offer good correlation to experimental data for proportional loading, they have not been found to be successful for non-proportional loading [40]. Also, neither the Tresca nor Von Mises can account for the influence of superimposed hydrostatic pressure, a condition that is known to affect fatigue lifetime [39].

The early work of Gough and Pollard [41] demonstrated that the effective stress amplitude was insufficient to correlate HCF under combined bending and torsion and proposed the ellipse quadrant and ellipse arc concepts for ductile and brittle materials, respectively. An historical common form which has been used to distinguish fatigue crack initiation behaviour of a number of stress states [42] is given by,

$$\sigma_{eff} + g(\sigma_h) = C \dots\dots\dots\dots\dots\dots\dots\dots\dots\dots\dots\dots\dots\dots (2.1)$$

where σ_{eff} is the Von Mises effective stress amplitude, g is a stress related parameter, σ_h is the mean value of hydrostatic stress over a cycle, and C is a constant for a given fatigue life. The 'fatigue life' in this instance represents the development of a crack of the order of 1mm.

Although these modified effective stress concepts have been used as the basis for some engineering HCF design practice during the past four decades, they do not however, reflect the physics of crack initiation and propagation and as a consequence do not agree with experimental data [42].

The later work by Guest [43], Stulen and Cummings [44] and Findley [45] proposed the earliest forms of the so-called critical plane approaches. Where the effects of maximum shear stress amplitude $\Delta\tau_{max}/2$ is modified by the influence of the amplitude of normal stress with respect to that plane $\Delta\sigma_n/2$. In the Findley model, fatigue failure is deemed to occur when

$$\Delta\tau_{max}/2 + A\,\Delta\sigma_n/2 = B \dots\dots\dots\dots\dots\dots\dots\dots\dots\dots\dots\dots (2.2)$$

where A and B are material parameters determined experimentally, which are constants for a given fatigue life.

Later Brown and Miller [39] proposed a method of evaluating multiaxial fatigue life again using the critical plane approach, but it reportedly represented a more realistic crack growth ideology. The method is based on the physical quantities that control fatigue crack growth, namely, the maximum shear strain and the tensile strain normal to the plane of maximum shear, although it has more emphasis on LCF. Thus expressed by the equation

$$(\varepsilon_1 - \varepsilon_3)/2 = f[(\varepsilon_1 + \varepsilon_3)/2] \ldots\ldots\ldots\ldots\ldots\ldots\ldots (2.3)$$

Fatemi *et al* [40] suggested that shear based critical plane approaches are appropriate for situations where a Mode II (shear mode) failure mechanism is predominant, although there are exceptions where combinations of materials and loading conditions can result in different failure modes.

McDiarmid [45] recently proposed variations to his previous critical plane model, a model based on the Findley criterion, which now attempts to take account of different crack patterns. Crack patterns that were first proposed by Brown and Miller [39] and known as Case A and Case B cracks. This terminology characterised the different directions of crack growth, such that cracks growing along the surface are termed (Case A) and cracks growing in from the surface are termed (Case B). The differences allow these specific cases of crack growth to relate two distinct classes of multiaxial fatigue [39].

2.2.6 Multiaxial Fatigue Crack Paths

Multiaxial fatigue crack paths exhibit Stage I and Stage II propagation [29], but, crack patterns differ depending on the applied multiaxial state of stress. Fig. 2.3 [29] shows the planes of crack growth for different multiaxial strain states that relate to stress states commonly found in engineering practice. Although in HCF the local conditions at the tip of a Stage I microcrack are mixed mode regardless of the remote loading mode combination due to crystallographic growth, local anisotropy and constraint of neighbouring grains, analogous to bimaterial interface cracks [42]. Therefore, multiaxial behaviour can be regarded as an inseparable feature of the HCF small crack problem.
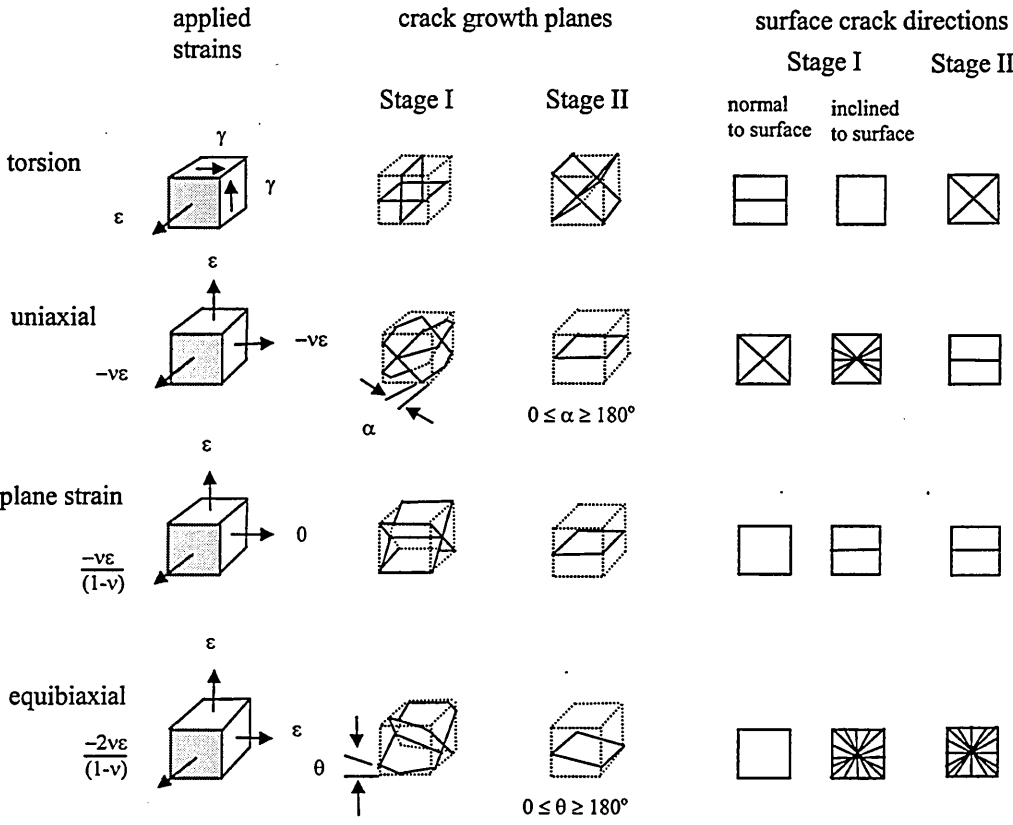
Fig.2.3 Typical crack planes for various states of strain [39]

To understand multiaxial fatigue crack growth mechanisms, some pertinent questions arise, such as, when and where will cracks initiate and in what direction and how fast will they grow. The intersection of the crack planes with the free surface plane is of particular importance, since the different attitudes of the planes of Stage I and Stage II cracks can dictate whether the fatigue life is lengthened or shortened. Similarly the orientation of a defect plane in a critical location of an engineering structure can affect fatigue life. Which indicates that crack shape and crack speed can change considerably depending on the directionality of the applied equivalent stress or strain state relative to the surface of the component or specimen

The physical behaviour of crack planes can be represented by the generalised 3-D fatigue theory proposed by Brown and Miller [39]. This particular theory considered the nucleation and growth of fatigue cracks and suggested two specific cases known as Case A and Case B for an isotropic material shown in Fig. 2.4.

The different cases are represented by showing how the free surface influences crack growth rate and shape, when considering loading of material subjected to fatigue and where the principal strains ($\varepsilon_1 \geq \varepsilon_2 \geq \varepsilon_3$). Case A is where the greatest range of principal strain amplitude ($\varepsilon_1 - \varepsilon_3$) both lie in the plane parallel to the free surface and the intermediate strain (ε_2) lies in the plane normal to the free surface. Whereas for Case B the minimum principal strain amplitude (ε_3) acts normal to the free surface. As for instance in biaxial tension (Case B) where the direction of the shear stress acts to promote the cracks to grow into the material. The Case B types of cracks are obviously considered to be more dangerous since they propagate away from the free surface into the material.
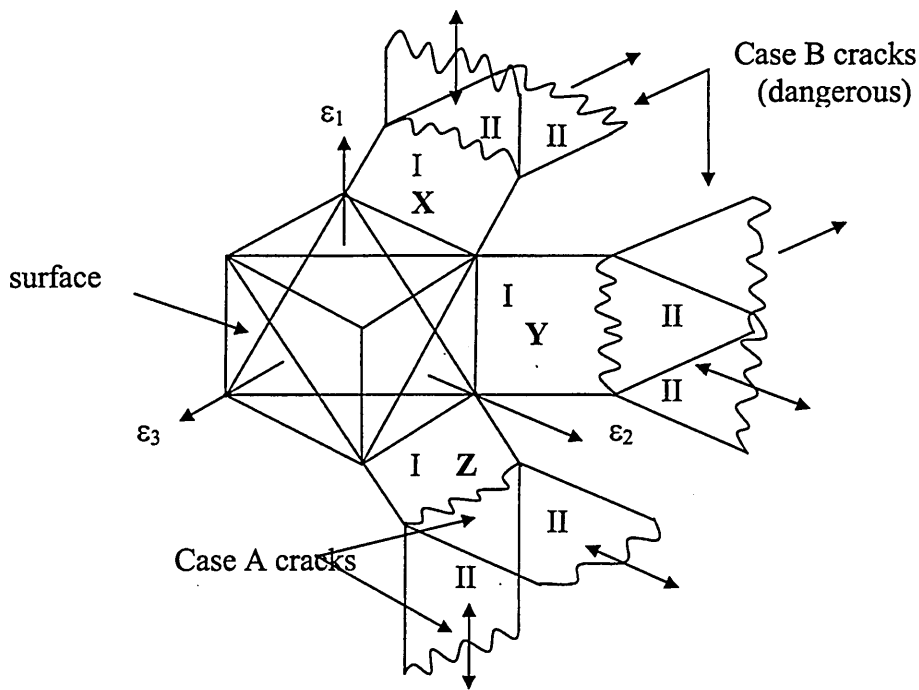
Fig. 2.4 A three-dimensional strained system Stage I
and Stage II - Case A and Case B cracks [39]

2.3 Non-Proportional Loading

Many engineering components and structures, such as, axles, crankshafts, ground vehicles, pressure vessels, aircraft parts and nuclear reactors generally experience non-proportional loading. Non-proportionality of loading can refer to combined out-of-phase loading or for sequential loading where the non-proportionality occurs in this case if the principal directions of the applied stress differ with respect to the crack plane, which is a loading system used in the current work.

Fig. 2.5 illustrates the strain-time histories and loading paths for (a) non-proportional combined loading, (b) non-proportional sequential loading, and (c) proportional loading for a cylindrical specimen subjected to torsion and axial fatigue loading.

Specimen subjected to torsion and axial fatigue loading

(a) strain-time history
    non-proportional
    combined loading

(b) strain-time history
    non-proportional
    sequential loading

(c) strain-time history
    proportional loading

90° out-of-phase combined non-proportional loading path

shear strain

general non-proportional loading path

normal strain

proportional loading path

non-proportional sequential loading path
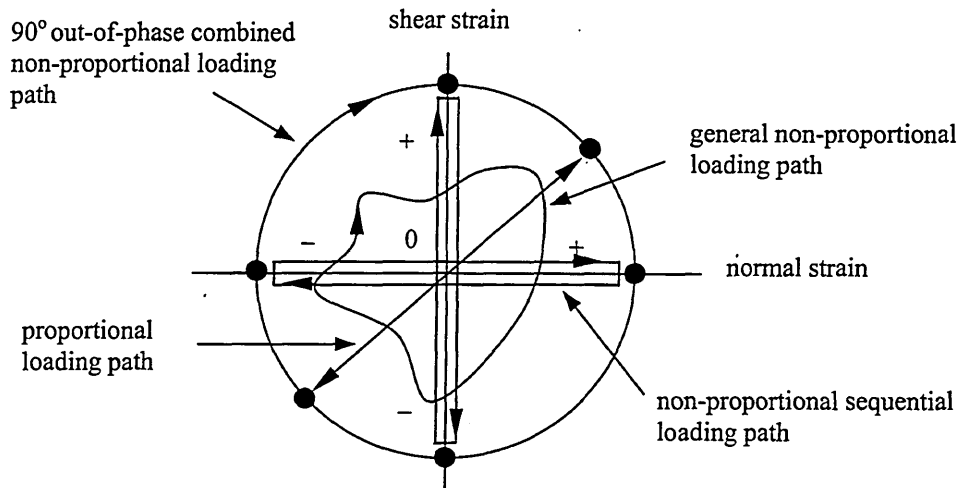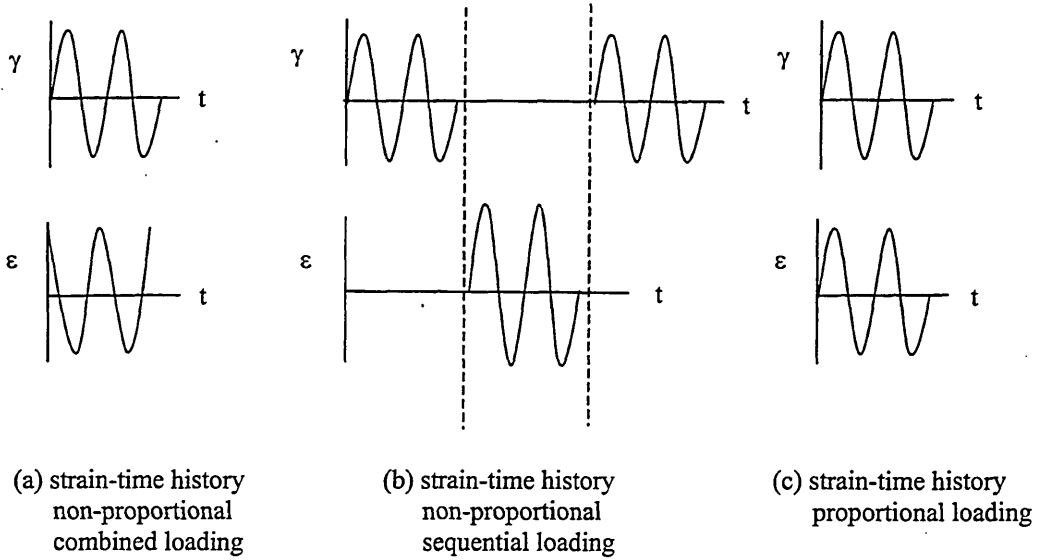
Fig. 2.5 Non-proportional and proportional loading paths

23

Non-proportional loading causes non-proportional straining in which the principal strain proportions and directions change during cycling. These are conditions that often cause additional cyclic hardening of the materials [46] and is considered to be the reason why low-cycle non-proportional loading is more damaging than low-cycle proportional loading [47]. The additional cyclic hardening during non-proportional loading can cause a dramatic decrease in fatigue life and Fatemi and Socie [40] proposed a modification to the original formulation of Brown and Miller's critical plane approach to account for this phenomenon. They considered that the strain parameters cannot account for cyclic hardening and thus proposed a change to the Brown and Miller's equation by incorporating a normal stress term instead of a normal strain term given by the equation,

$$\gamma_{max} \left(1 + n\, \sigma_{n\,max}/\sigma_y\right) = \text{Constant} \,\dots\dots\dots\dots\dots\dots\dots\dots (2.4)$$

where n is a constant found by fitting uniaxial data against the pure torsion data, σ_{nmax} is the maximum normal stress and σ_y is the yield strength of the material.

Unlike proportional loading where the principal stress/strain ratios and the principal planes remain unaltered during loading, the principal stress/strain ratio and principal planes change in relation to the crack plane in sequential non-proportional loading and therefore this could have a significant effect on crack growth behaviour.

Gao and Fernando [48] reported that for non-proportional sequential overloading, Stage I and Stage II crack advance is dependent on their respective favourable crack orientations in relation to their multiaxial stress state. For instance in the HCF

regime, particularly for in-plane shear non-proportional overloading, an increase in crack growth rate can occur and consequently cause a reduction in fatigue life. This was reportedly [48] attributed to the reduction in crack tip blunting and the crack tip becoming sharper. Although in this case it maybe better to relate this effect to lower compressive residual stresses normal to the crack plane, rather than imply a change in the crack tip profile which is obviously difficult to ascertain.

It is generally accepted that non-proportional loading is more damaging than proportional loading for a variety of loading, but is this so for a relatively marginal non-proportional load interruption in sequential loading. Especially where the interrupted loading may appear insignificant in terms of the number of fatigue cycles applied and furthermore maybe incorrectly dismissed in fatigue design analysis. The work presented here examines this particular case of how a non-proportional loading sequence affects Stage I crack growth and subsequent fatigue life of specimens for various stress states in the HCF regime.

2.4 Sequential Loading

It is known that sequential loading has an effect on fatigue life where load changes of the same stress state are significant. Such that the damage summation according to Miner's linear damage rule LDR for low-high or high-low loading sequences will be greater or less than unity respectively. However, where different stress states are involved i.e. push-pull and torsion, it has been reported that lifetimes can be changed significantly depending on which stress/strain state is applied first in the loading sequence [49] [50].

Brown *et al* [51] outlined the above effects for a particular stress-strain state which gave the same endurance in reversed torsion and push-pull loading with R = -1. The fatigue lifetime was reportedly [51] dramatically reduced when the original stress state was initially applied in torsion then in push-pull. Conversely an unusual increase in lifetime was observed if the stress states were reversed i.e. push-pull loading followed by torsion loading. Indicating that the reduction in lifetime was due to broad Stage I crack (see Fig. 2.3 torsion Stage I crack growth planes) naturally continuing propagating in Stage II (see Fig.2.3 uniaxial Stage II crack growth planes). Whilst the enhancement in lifetime was considered to be as a result of Stage I cracks generated in push-pull (see Fig 2.3 uniaxial Stage I crack growth planes) hindering the development and extension of shear cracks in torsion (see Fig. 2.3 torsion Stage I crack growth planes). This is because in this case the cracks form on different planes. Probably because of the incompatibility of existing slip plane configuration that does not reconcile with the maximum shear planes associated with different stress state, for such small cracks at these stress amplitudes.

Obviously, the fatigue life of engineering components can be affected quite dramatically for sequential loading, depending on the configuration of the applied stress states. The effect the different loading system has on crack advance is mainly dependent on the extent of the interactive nature of deformation and fracture process of each loading mode. Zhang [50] reportedly found that for medium carbon steel subjected initially to push-pull and then to torsion loading, that push-pull cracks which were less than a critical crack length (equivalent to the Stage I-Stage II crack transitional length), new cracks formed at the onset of torsion loading in preference to continued crack growth of existing cracks.

Stage II crack growth is the dominant period for fatigue lifetime at high strain amplitude whereas at low strains it is Stage I which occupies the majority of the lifetime. The physics of fatigue damage as a crack advances has culminated in considerable work to propose theories to describe the kinetics of crack growth [10]. Therefore, since the fatigue lifetime of smooth engineering components is usually cumulative of Stage II and Stage I crack growth, then the mechanics of crack growth associated with these stages are necessary to describe the complete fracture process. Fracture mechanics provides the basis for analytical concepts. However, the fracture mechanics terminology used for long and short cracks is different since the mechanisms associated with crack propagation for each type of crack are influence by totally different parameters.

2.5.1 Long Crack Growth

The Stage II crack growth region is generally associated with the term long cracks and linear elastic fracture mechanics (LEFM) or elastic-plastic fracture mechanism (EPFM) is usually invoked to quantify the propagation behaviour of these long fatigue cracks. The crack surface displacements in LEFM as shown in Fig. 2.6 [34], can be in three principal modes namely,

1. Mode I - The tensile opening mode

2. Mode II - The in-plane sliding mode

3. Mode III - The tearing or anti-plane shear mode

The application of LEFM in crack growth considers only the macroscopic aspects of crack growth and is based on the intensity of the stress field at the crack tip [20]. The characterisation of this elastic stress distribution near the crack tip is denoted by a single parameter the stress intensity factor (K) after Irwin [52].
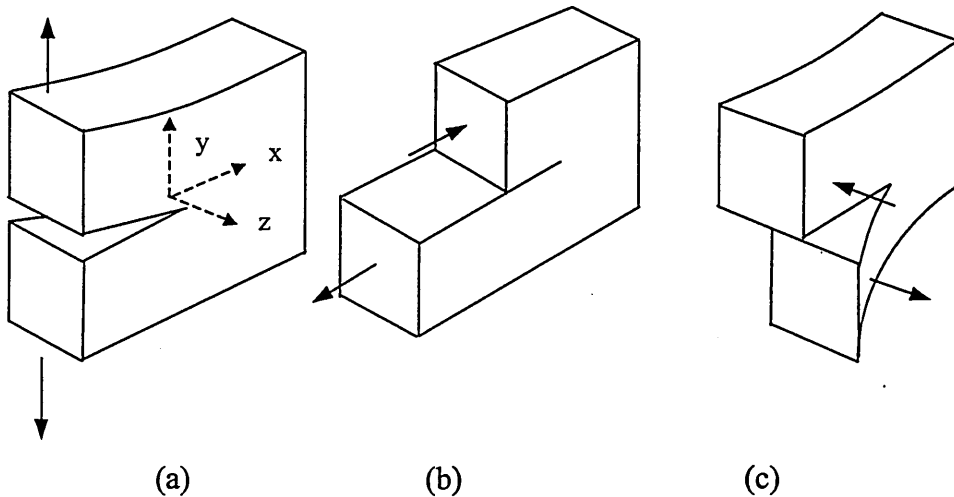
Fig. 2.6 The modes of fracture (a) Tensile opening (Mode I). (b) In-plane sliding (Mode II). (c) Anti-plane shear (Mode III). [34]

Depending on the deformation mode K is usually defined accordingly. For the case of a Stage II fatigue crack in push-pull loading which grows by a Mode I mechanism then K is given in the more general form as,

$$K_I = Y \sigma (\pi a)^{1/2} \quad\text{..} (2.5)$$

where Y is a geometry factor and is dependent on crack configurations, σ and *an* are stress perpendicular to the crack and crack length respectively. The solutions for values of Y are available for idealised geometry, crack tip displacement and mode of deformation [53].

In the analysis of fatigue crack growth LEFM assumes that the crack growth rate da/dN is a function of ΔK, given by the Paris and Erdogan [54] equation,

$$da/dN = C\ (\Delta K\ )^{m} \dotfill (2.6)$$

where da/dN is the rate of crack growth, a is the crack length and N is the number of fatigue cycles. The terms C and m are empirical constants which are functions of the material properties and microstructure, test frequency, mean stress or load ratio, environment, loading mode, stress state and test temperature [34], and where ΔK is defined as,

$$\Delta K = K_{max} - K_{min} \dotfill (2.7)$$

where K_{max} and K_{min} are the maximum and minimum stress intensity factors corresponding to the maximum nominal stress σ_{max} and minimum nominal stress σ_{min}. However, for cyclic loading the compressive load is assumed to be carried by the faces of the crack, thus avoiding the intensification of stress around the crack tip. It is therefore conventional to take K_{min} equal to zero, when the stress ratio (R < 0), where $R = \sigma_{min}/\sigma_{max}$, on the assumption that crack will close up at zero load [55].

Engineering structures that are subjected to low levels of stress and have inherent flaws of a size (0.5-1mm) are generally the parameters that allow designers to benefit from LEFM analysis [56]. Where the evaluation of crack growth up to a critical size using LEFM analysis could be in the order of several hundred millimetres. However, the majority of engineering components have no pre-crack present and therefore, ΔK is zero, but, fatigue cracks will initiate and grow if the applied stress is of significant magnitude as described earlier. The critical value of ΔK below which long cracks will be arrested is termed the stress intensity threshold (ΔK_{th}). The cracks that grow in the region below ΔK_{th} are the so-called short cracks i.e. cracks that do not behave in principle as long cracks, and where LEFM is not considered applicable [57]. McDowell [37] found that this was particularly so for lower stress amplitudes where the deceleration of crack growth was observed and which corresponded to a dip in the da/dN vs. ΔK behaviour. It is therefore very important to evaluate the growth of short cracks when considering the fatigue life of materials and components [33] [57].

2.5.2 Short Crack Growth

The term 'short cracks' is usually referred to cracks which are not considered long enough to be described by LEFM, since LEFM becomes inapplicable to characterise the growth of fatigue cracks which are of crack size less than 0.3mm [34]. This is because the relationship between the far-field loading conditions are quite different to the near-tip conditions when comparing the crack size of short and long cracks. For instance short cracks in the order of 5-10 times the microstructural scale in length [37] require a high stress to propagate them, whereas long cracks being on a

macroscopic scale greater than 1mm in length [33] usually require a low stress to propagate them.

The schematic diagram of idealisation of short and long crack growth is shown in Fig. 2.7
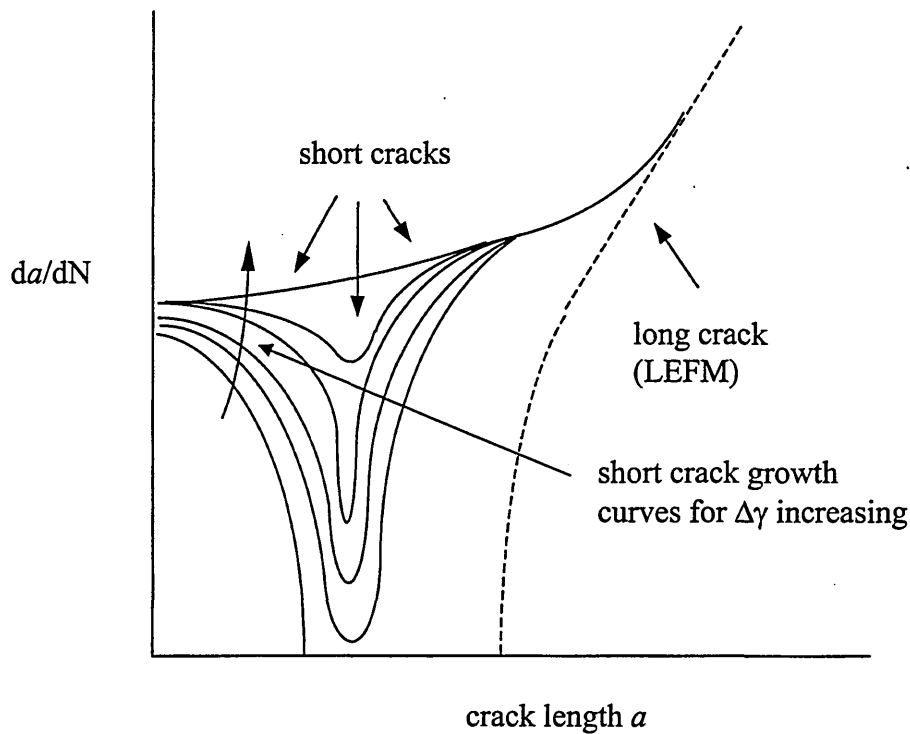
Fig.2.7 Schematic diagrams of idealisation of short and long cracks [95]

It is only the upper limit of a short crack length that will conform to LEFM analysis where ΔK_{th} approximates to a limiting value. Although Allen *et al* [58] suggested that LEFM may be able to predict the behaviour of short cracks as the crack length tends to zero by introducing some criteria to account for the changes in the stress field at the vicinity of the crack tip. McDowell [37] however, presented a view to the contrary, that whilst several quantitative attempts have been made to explain the

31

fatigue propagation of short cracks in terms of plasticity-induced closure, along with adoption of an additional component of the driving force e.g. crack tip opening displacement, to reflect the contribution of cyclic plastic strain, suggested that the models are complex and depend on idealised assumptions that neglect microstructure properties such as local anisotropy and heterogeneity. It would appear to date, that no apparent work has been done in this field in which models based on LEFM analysis is recognised to adequately reflect the behaviour of short crack growth regime.

The inability of established methods of fatigue analysis, such as fracture mechanics, to provide acceptable mathematical models, has therefore, created considerable interest in the behaviour of short fatigue cracks [58-62]. The interest in short fatigue cracks has been brought about by the realisation that even below the fatigue limit cracks can form. Thus offsetting the traditional belief that the fatigue limit and the region below it was coincident with no apparent crack initiation, rather than what is now recognised as the limit for non-propagating cracks to exist [63].

For the design analysis of defect tolerant structures the method of predicting fatigue lives is generally based around the base-line da/dN data which is obtained from laboratory generated results on test specimens containing relatively long cracks. However, engineering components are generally free from any defects on the scale that allows any immediate transition to long crack growth, and as a consequence a large proportion of the lifetime will be spent in the short crack domain. Keiro et al [96] who studied the behaviour of small fatigue cracks for a medium carbon steel found that the growth of small cracks shorter than approximately 1mm represented 80% of the fatigue life. It is therefore, very important to understand the role of short

cracks so that a more complete and realistic fatigue analysis is achieved. If fatigue lifetimes do not take into account the short crack regime then any fatigue lifetime prediction reliant on LEFM alone, would probably not only be inaccurate, but, could be non-conservative.

Several workers [64] [65] have noted the anomalous behaviour of short cracks that is uncharacteristic of long crack growth. Pearson [59] was first to report observations of accelerated growth of small cracks compared to long cracks. Who examined the effect of crack size on propagation rates that were subjected to the same nominal ΔK. Other workers [37] [67] have also found that short cracks consistently exhibit higher crack growth rates than those cracks associated with LEFM. However, Morris [66] and Lankford [67] found the opposite effect in that short crack growth was slower than for long crack growth. Nevertheless, irrespective of whether short cracks propagate faster or slower than LEFM predictions, the behaviour of short cracks cannot be considered to be consistent with that of long cracks. Consequently the short crack domain can represent a major part in the total fatigue lifetime of most engineering components and as such this domain is examined further.

2.5.3 Short Crack Domain

The short crack domain can be considered as the region of endurance that is dominated with the growth of these so-called short cracks. Whilst the propagation of short cracks can be a substantial feature of HCF there is no universal interpretation for short cracks or any definitive demarcation between long and short cracks,

33

although several possible definitions have been proposed. Suresh and Richie [68] suggested that short cracks might be defined as being short when,

(1) Fatigue cracks are of a size which is comparable to microstructural dimensions i.e. same order as the grain size (μm).

(2) Small fatigue cracks in smooth specimens for which the near-tip plasticity is comparable with the crack size.

(3) Fatigue cracks classed as being simply physically small when of a macro-length (<1.0 mm).

When considering the extent of the plastic zone the size and shape depends on the plastic flow properties of the material, but, its dimensions are proportional to $(K_I/\sigma_y)^2$ [69]. In fracture mechanics the yielding at the crack tip is approximated to a plane strain condition and the nominal plastic zone (r_p) is given by [69], as

$$r_p = 1/2\pi \ (K_I/(\sigma_y)^2 \ \dots\dots\dots\dots\dots\dots\dots\dots\dots\dots\dots\dots\dots \ (2.8)$$

However, for LEFM analysis the limitation of small scale yielding for the plastic zone size at the crack tip [53], is given by

$$r_p < a/50 \ \dots\dots\dots\dots\dots\dots\dots\dots\dots\dots\dots\dots\dots\dots\dots \ (2.9)$$

But, for short cracks the plastic zone size is generally taken to be of the same order as the crack length where the ratio ($a/r_p \approx 1$) [33]. This is obviously of such a scale that makes LEFM non-compliant in the short crack domain. Although, Tokaji [57] found that for a coarse grained low alloy steel, cracks behaved as long cracks even though the cracks were physically small.

The short crack domain implies a region where cracks are physically small and Miller [56] suggested that all cracks be considered short except for those propagating at low stress levels i.e. $\Delta\sigma < 2\sigma_{cy}/3$. Whereas McDowell [37] suggested that cracks are considered short when all pertinent dimensions are small compared to some characteristic length scale. However, Miller [33] outlined a more detailed and physical crack demarcation by grouping short cracks with respect to particular modes of crack growth and an associated dimensional constraint. For instance the so-called microstructural short cracks having a crack length of microstructural scale ($\approx 2\mu m$) and physically small cracks having a crack length in the order 1mm. The Kitagawa-Takahashi diagram [70], is modified to represent the distinct regimes of crack behaviour described after Miller [56] namely,

(1) Microstructural short cracks (MSC), where $a < d_3$

(2) Physically small cracks (PSC), where $d_3 < a > l$

(3) EPFM type cracks - highly stressed cracks where $a > l$ and $\Delta\sigma > 2\sigma_{cy}/3$

(4) LEFM type cracks - long cracks where $\Delta\sigma < 2\sigma_{cy}/3$
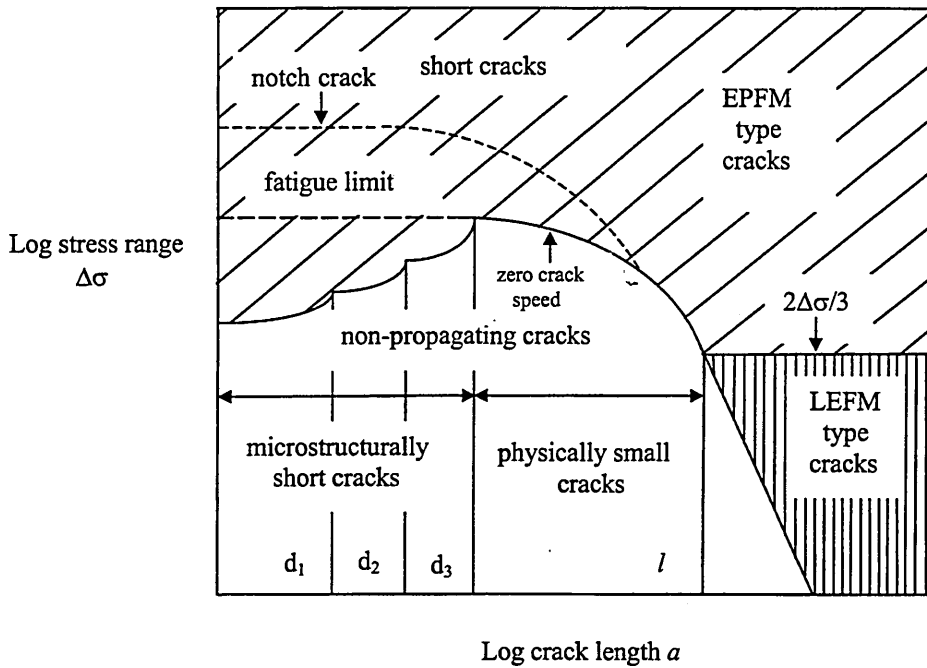
Fig. 2.8 The three regimes of short crack behaviour [56]

The lower limit for a short crack can be taken to be 2-3μm corresponding to the surface roughness of the best prepared engineering component [71] or assumed to be zero since the crack growth from 0-3μm makes only minimal difference to the lifetime [30]. The upper limit of a short crack is that length which can be calculated from LEFM analysis in which the stress intensity is equivalent to ΔK_{th}.

The current research work involves the fatigue lifetime of smooth specimens under high cycle multi-stage loading conditions. Under these particular loading conditions the influence of MSC and PSC growth are a dominant feature and the parameters that are influential to these cracks are examined in more detail below.

36

2.5.4 Microstructural Short Cracks (MSC)

The extent of the influence of microstructure on fatigue crack growth is an important factor when considering the behaviour of short crack growth of metals, because the microstructural properties of the material determines the extent of the MSC growth [56]. MSC growth is specifically associated with the microstructural-dependence of crack growth and as such these cracks are represented by the term - microstructural fracture mechanics (MFM) [33], shear dominant Stage I cracking regime or Mode II and Mode III mechanism.

The degree of influence of MSC growth centres around the composition of a polycrystalline metal and for the adequacy of this work, its composition is considered to be basically a crystalline structure made up of grains, where the grain boundaries are obstacles to slip [72]. Consequently these boundaries will not generally afford easy passage for crack growth, unless there is sufficient crack driving force. Miller [33] suggested that twin boundary; grain boundaries and pearlite stringers in medium carbon steel are barriers to MSC growth. In some instances MSC growth may be limited to one grain [73], but, it can however, extend to several grains in some metals [74][75][76].

In a ferritic-pearlitic banded structure a material similar to the one used in this work, the softer ferrite grains are generally the sites for crack initiation [50], and MSC growth may extend through several ferrite grains before arresting at a pearlite colony [56]. Although typically for a ferritic-pearlitic structure, several different microstructural barriers may exist to preclude crack growth [76]. As shown

37

schematically in Fig 2.9 the successive resistive barriers can only be overcome by increased stress levels
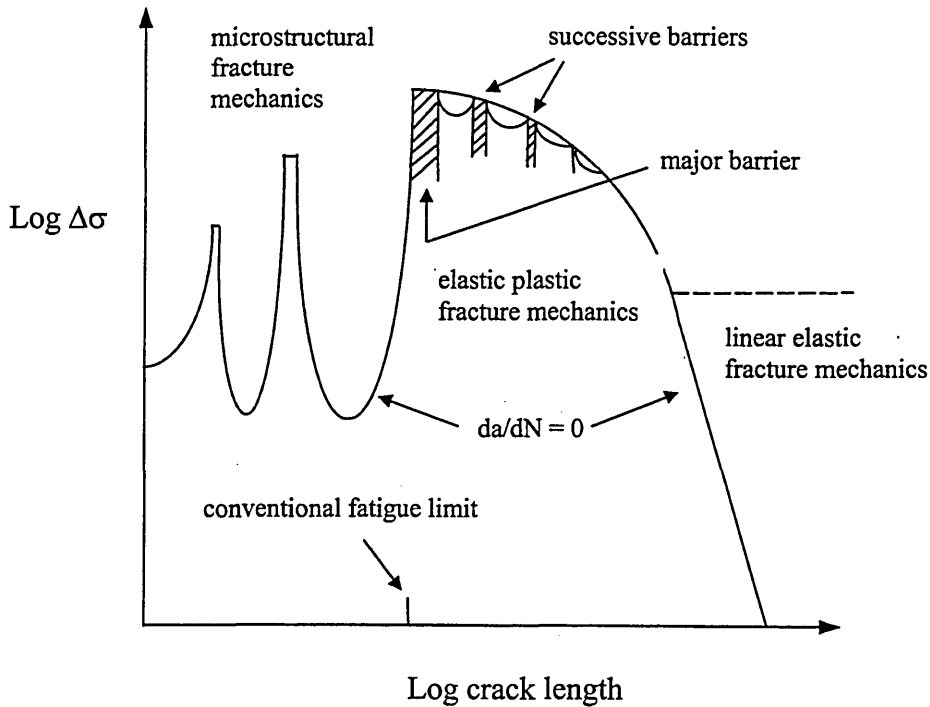
Fig. 2.9 Schematic representation of the effect of successive

microstructural barriers on fatigue crack growth [33]

The increase in stress level to overcome these barriers is necessary to induce the cross slip or the operation of secondary slip systems in the next grain [77]. The pearlite regions are the barriers of greatest strength and therefore, represent a much more formidable barrier to crack growth. These pearlite barriers have been observed to be particularly influential in arresting transverse cracks in torsion where the pearlite banding is normal to the crack direction [77].

38

If grain boundaries are the dominant barriers to crack growth then the reduction in grain size can improve the fatigue resistance of smooth specimens [78], although this is only beneficial for smooth engineering components where an increase in the fatigue limit is desired. Since the ΔK_{th} tends to reduce with the reduction in grain size, possibly because smaller grain sizes afford less sustainable deformation at the crack tip [62]. Kage *et al* [79] reported on the grain size effect being due to barriers to MSC growth for two different carbon steels (A) and (B) having grain sizes of 15μm and 50μm respectively. It was found that cracks stopped propagating in the smaller grain material after fewer cycles.

The MSC regime involves complexities in crack growth that arise from the individuality of microstructural properties of the material. The microstructural effect on a growing crack is generally not infinite, and the mechanisms of crack growth change at some point, which is a function of, crack length and the applied stress range. Therefore, the upper bound of MSC growth is the start of cracks that are considered to grow under markedly different criteria to MSC and are referred to as physically small cracks.

2.5.5 Physically Small Crack (PSC)

PSC growth is the behaviour of cracks that is bounded by the upper limit of MSC growth and the lower limit of long crack growth the LEFM threshold ΔK_{th}. The transition from a MSC to a PSC usually occurs when the crack has reached a length in the order of several grain diameters. McDowell [37] suggested that when the crack reached sufficient length a PSC begins to exert an influence on cyclic deformation

39

and damage process at the crack tip in accordance with elastic plastic fracture mechanics (EPFM) crack opening and singularity concepts. EPFM concepts become applicable when the scale of plastic deformation at the crack tip are small compared to crack length and span over sufficient number of microstructural barriers, but where microstructural influence is still evident [37]. This has been justified by the application of EPFM concepts to the PSC in the short crack growth regime [80] [81]. Some workers [82] [83] have suggested that crack density is a precursor for the transitional boundary between MSC and PSC growth. They observed that the crack density increased with fatigue cycling in the MSC stage and at the transition point into the PSC stage, it reached a saturation point, then decreased until failure. However, other workers [84] [85] have found the contrary, that crack density increased throughout the entire fatigue lifetime of the specimens.

Whereas MSC growth is the region governed mainly by the effects of microstructural barriers, PSC growth is the region where crack growth is more dependent on stress level [86]. The stress level must be above the fatigue limit stress if PSC are to propagate beyond MSC growth barrier. The PSC growth regime is therefore, considered to be an intermediate stage of crack growth between MFM and LEFM stages where a higher stress is required to overcome the more persistent microstructural features to crack growth. It appears to be appropriate to signify the growth of PSC in terms of some controlling cyclic stress parameters since the fatigue limit stress is the upper threshold for non-propagating MSC growth, and 0.3 x cyclic yield stress ($0.3\sigma_{cy}$) is the upper threshold where LEFM analysis prevails [62]. Although at and above the cyclic yield stress cracks may be considered long in LEFM terms but behave as short cracks [59] where the PSC growth regime is

dominant and therefore EPFM need to be invoked. In fact once the stress limit of 0.3 σ_{cy} is exceeded then EPFM analysis should strictly be used [67], and Skelton [87] proposed a variety of parameters to correlate fatigue crack growth under this behaviour. The types of equations that are given in literature to quantify the growth of cracks in the EPFM region [62] are of the form,

$$da/dN = A(\Delta\varepsilon_p)^n a \quad\text{..} \quad (2.9)$$

where $\Delta\varepsilon_p$ is the cyclic plastic strain range and A and n are material constants. Ibrahim and Miller [88] indicated that the index 'n' was approximately 2.0 for two plain carbon steels.

PSC growth is also synonymous with greater growth rates where the so-called 'anomalous behaviour' does not always conform to LEFM analysis [65] [66], especially just beyond MSC growth region where the microstructure is still influential in part. However, this microstructural influence has a diminishing affect as the crack length increases to the point of ΔK_{th} where the microstructural effects become insignificant.

2.6 Short Fatigue Crack Model

2.6.1 Introduction

Since short crack propagation generally comprises a significant part of the fatigue lifetime of smooth clean engineering components, its degree of influence must be

recognised and adequately accounted for. The behaviour of short cracks has been known of for some time [89] [65], and there has been considerable attempts to model them embracing several techniques e.g. dislocation-based models [90] [91], models based on LEFM and EPFM [65] [87], models based on statistical analysis [92]. However for the current work, crack growth models based on short crack growth of the form developed empirically by Hobson [93] are used. These crack growth models have been shown [93] to be capable of predicting MSC and PSC crack growth for a medium carbon steel, which reflect crack growth initially dependent on microstructural features and the subsequent crack growth beyond this dependency. The models however, have been used mainly for restricted loading paths i.e. uniaxial loading or torsion loading. Therefore the validity of these models are considered under multiaxial and multiphase loading by this current work. The schematic representation of short crack growth is shown in Fig. 2.10
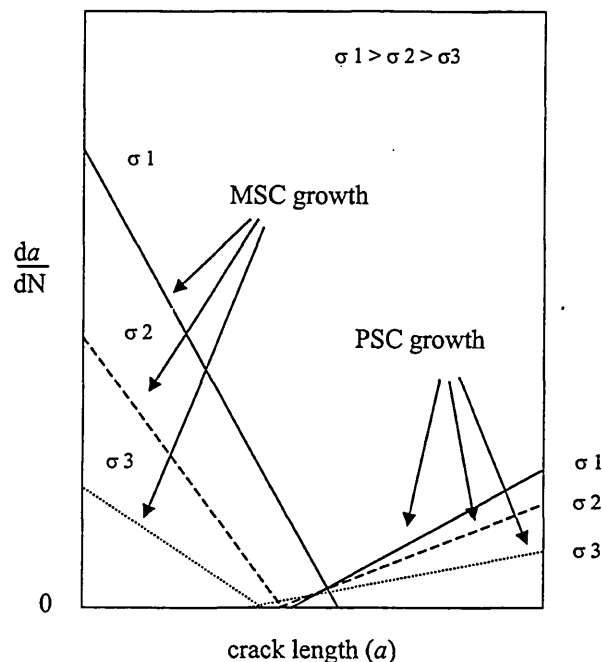

Fig. 2.10 Schematic representation of linear graphs for short crack growth

2.6.2 Theoretical Model - MSC Growth

To model the behaviour of MSC growth, the model must theoretically replicate the resistive nature of the material's microstructure if accurate representation of crack advance is to be realised as it negotiates the successive microstructural barriers. Therefore, it is essential for the model to account for these microstructural influences and Hobson [93] derived an expression for crack growth using the method of dimensional analysis. This expression detailed in ref. [93] considered parameters that might be expected to affect the propagation of a crack embedded within the grain containing a nucleation site, from which the solution is given below;

$$da/dN = C(d-a)^{1-\alpha} a^{\alpha} \dots\dots\dots\dots\dots\dots\dots\dots\dots\dots\dots (2.10)$$

where C is a stress or strain related parameter, d is the microstructural barrier length, α is a material constant and a is crack length.

The above crack growth equation has been used to describe the propagation of short cracks in aluminium [94] that analysed experimental data collated by Lankford [95]. Where Hobson [94] used a 'best fit ' analysis and reportedly found that for 7075-T6 Aluminium alloy $\alpha = 0.4$, and extended the analysis to a medium carbon steel subjected to push-pull loading found that $\alpha = 0$ [93]. Carbonell and Brown [96] and Miller *et al* [55] also used the same value for $\alpha = 0$, for a similar medium carbon steel, but, subjected to fully reversed torsion loading and reported to have obtained similar results. Also more recently Zhang [50] carried out push-pull and fully

reversed torsion loading tests on medium carbon steel again with $\alpha = 0$, and again reported good results.

A further interesting point in the crack growth model analysis used by Zhang [50], was the method for the determination of the microstructure parameters. Where d_1, was taken as the upper bound of the average ferrite grain and the subsequent grain sizes d_2, d_3, etc. taken to be equal to the mean ferrite grain size. It was reported [50] that there was good agreement between the experimental results and theoretical calculations, indicating that the method of determining d was acceptable for medium carbon steel. The work by Zhang [50] confirmed the proposal Hobson *et al* [97] had suggested earlier, that from experimental observations performed in fully reversed tension-compression loading on a medium carbon steel, the value of d could be reasonably equated to the ferrite plate length.

To equate the parameter d to a microstructural feature appears appropriate, since in practice the measurement of d for each crack is difficult to obtain [97], whereas, micrographic techniques enable easy determination of grain sizes and other surface microstructural features. Also the determination of d estimated in this way, although it may appear somewhat subjective, research work [67] has indicated that statistical analysis of the microstructure can adequately reflect the barriers to crack growth. Murtaza *et al* [98] using surface replica techniques found that crack growth retardation position of the average crack length coincided well with the prior average austenite grain size for a heat treated low-alloy steel. Although this is not the case for all materials, for instance, in some aluminium alloys the microstructural barriers are not so evident as to influence any appreciable retardation in crack growth [99].

However, there appears to be reasonable confidence in relating the parameter d to the mean ferrite grain for a medium carbon steel.

It would appear that equation (2.10) represents reasonable analysis of MSC growth for polycrystalline materials although its application has been somewhat limited for different materials. However, several workers [96][93][55][50] have shown that for medium carbon steel, MSC maybe characterised adequately by the crack growth law in the form given below,

$$da/dN = C \ (d\text{-}a) \ \dots\dots\dots\dots\dots\dots\dots\dots\dots\dots\dots\dots \ (2.11)$$

If a crack continues to propagate, then the transition to Stage II crack growth is influenced by different criteria as discussed previously and subsequently the model has to reflect the growth of PSC and the eventual establishment of a long crack.

2.6.3 Theoretical Model - Long Crack

Long crack growth is the region of accelerating crack growth beyond the MSC growth region extending to failure at a point beyond ΔK_{th}, which then conforms, to LEFM. The threshold effects on fatigue crack growth of long cracks as they approached ΔK_{th} are accounted for by modifying the equation (2.6) [54], which introduces a parameter to describe LEFM data down to the threshold [100], given by the equation of the form,

$$da/dN = C((\Delta K)^m - (\ \Delta K_{th})^m) \ \dots\dots\dots\dots\dots\dots\dots\dots \ (2.12)$$

where ΔK and ΔK_{th} are the stress intensity factor range and threshold respectively, and C and m are material constants.

Hobson [44] developed equation (2.12) to express the crack growth equation as function of a instead of ΔK in a dimensionally correct form (which implies m = 2), given by

$$da/dN = Ba - D \dots\dots\dots\dots\dots\dots\dots\dots\dots\dots\dots\dots (2.13)$$

where B is a stress or strain related parameter, D is a material constant and a is crack length.

2.7 Fatigue Life Assessment

2.7.1 Introduction

It is common for engineering components to be subjected to different states of cyclic stress with loading of various magnitudes. Therefore, it is necessary to have some form of accountability of the loading to give confidence in the working life of the engineering component. The question of quantifying fatigue damage sustained during each cycle and the necessary summation is still unanswered in certain complex fatigue patterns. Although obviously there is a requirement for accurate fatigue life prediction methodologies especially in an engineering dominated society we have of today. However, there appears to be no universally accepted definition of fatigue damage, although there have been many attempts to provide suitable

explanations. All attempting to apply different criteria and approaches to account for fatigue damage. This review will examine some of the theories relevant to this work, to see how they have developed over the years to account for complex loading patterns.

2.7.2 Linear Damage Rule

The early recorded fatigue damage models date back to the 1920s and 1930s [101][102][103], and it is over seventy-five years since Palmgren put forward the hypotheses of linear summation of fatigue damage, now accepted as the - linear damage rule (LDR). This concept later expressed mathematically by Miner [104] in 1945 in the form of,

$$D = \Sigma(n_i / N_{fi}) = 1 \quad\dots\dots\dots\dots\dots\dots\dots\dots\dots\dots\dots\dots\dots\dots\dots (2.14)$$

where D represents the damage, n_i the applied cycles at stress level σ_i and N_{fi} the total cycles to failure under constant amplitude loading.

The Palmgren-Miner rule is the most common empirical law used to predict fatigue life subjected to variable stress levels because of its simplicity. The fatigue damage (D) that occurs at the various stress levels is assumed to accumulate linearly and is considered to be independent of any microstructure, the possible effect of any micromechanism and sequential loading and/or type of loading. However, it is well known that if loading sequence is from low to high stress, then D>1; and conversely for high to low stress, D<1. Furthermore it as been shown previously [105] [106]

47

and again recently [50] that fatigue damage accumulation under sequential loading for different types of loading is non-linear. Fatemi and Yang [107] in their recent survey of cumulative fatigue damage and life prediction theories also concluded that due to the inherent deficiencies of the LDR these are generally unsatisfactory irrespective of any modified version [108] [109].

To overcome the anomalies of LDR many later studies [110-112] put forward predictions for fatigue damage accumulation on different themes without expressing any definition of the physical damage mechanism. However, Manson *et al* [113] proposed a double linear damage rule (DLDR) which considered the damage process to have two separate linear phases, but, not necessarily associated with crack initiation and propagation as shown in Fig. 2.11.

The approach by Manson was built on Grover's [114] qualitative hypothesis of separating crack initiation and crack propagation that considered cycle ratios for the two separate stages in the fatigue damage process. The co-ordinates of the 'transition knee-point' (knee) for the DLDR theory are approximated from the following empirical equations

$$[n_1/N_{f1}]_{knee} = 0.35 \, (N_{f1}/N_{f2})^{0.25} \dots\dots\dots\dots\dots\dots\dots\dots\dots\dots \, (2.15)$$

$$[n_2/N_{f2}]_{knee} = 0.65 \, (N_{f1}/N_{f2})^{0.25} \dots\dots\dots\dots\dots\dots\dots\dots\dots\dots \, (2.16)$$

where the subscripts 1 and 2 represent the initial and second stress level respectively.
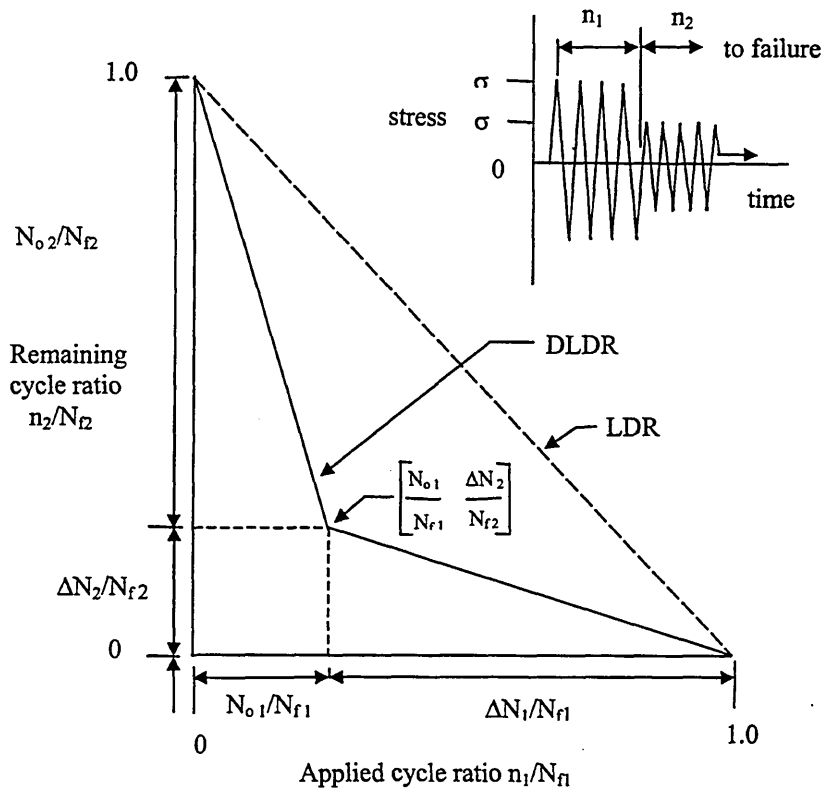
Fig. 2.11 Diagram showing DLDR for (H-L) two level load cycling [107]

In order to refine the DLDR, Manson and Halford [113] developed a damage curve approach (DCA) and a subsequent double damage curve approach (DDCA). The DCA was developed to refine the original DLDR in order to account for phenomenological factors associated with the complex processes of crack growth such as dislocation agglomeration, sub-cell formation, multiple micro-crack formation and the independent growth of these cracks to form a dominant crack [107]. The refined DLDR knee points in a damage verses cycle ratio (D-r) plot, divide the damage process into two phases given by,

$$D_{knee} = A \, (N_r/N)^{\alpha} + r_{knee} = 1 - (1 - A)(N_r/n)^{\alpha} \dots\dots\dots\dots (2.17)$$

49

where A and α are material constants. The DDCA refines further the DCA by the addition of a linear term and with some mathematical manipulation and may be represented [107] of the form,

$$D = [(pr)^k + (1 - p^k) \, r^{kq}]^{1/k} \quad \text{..} \quad (2.18)$$

where k is a mathematical exponent, q is a load level parameter and p is given as,

$$p = D_{knee}/r_{knee} = [A \, (N_r/N)^\alpha] / (1 - (1 - A)(N_r/N)^\alpha) \quad \text{.......} \quad (2.19)$$

The comparisons of the DDCA to the DLR and DCA for high to low (H-L) interactive test for a 316 stainless steel are shown in Fig. 2.12 [113].
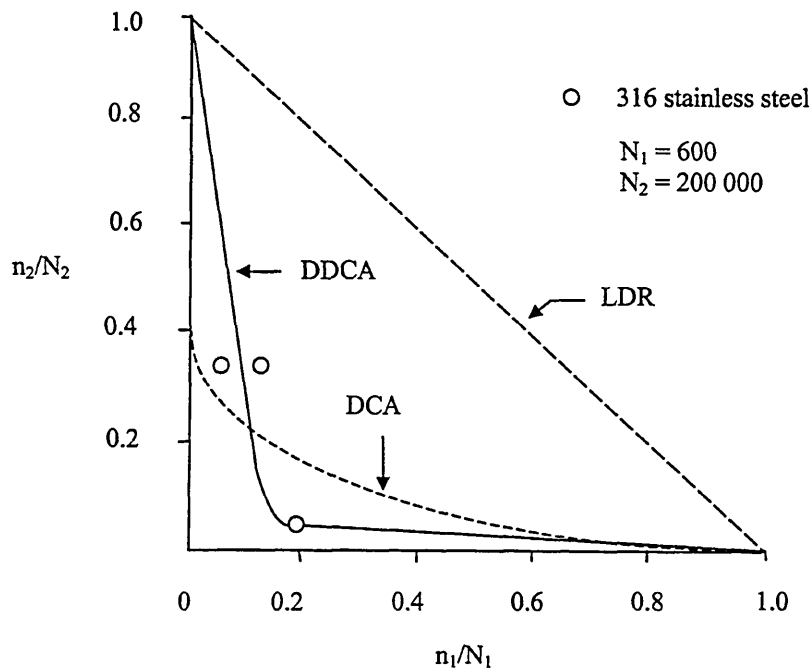

Fig. 2.12 Comparison of DDCA to LDR and DCA for a H-L interaction test [33]

50

Cumulative fatigue damage and fatigue life theories from the 1970s to date have seen the continual development of crack growth concepts, because cracks are directly related to fatigue damage and are widely accepted.

The earlier crack growth concepts centred around LEFM which resulted in the development of macro crack growth models to account for load interaction effects in the propagation phase (Stage II). The macro-crack growth retardation model or yield zone model proposed by Wheeler [115], modified the Paris constant amplitude growth rate equation $da/dN = A(\Delta K)^m$ by employing an empirical retardation factor C_i such that,

$$da/dN = C_i [A(\Delta K)^m] \text{...} (2.20)$$

where $C_i = (r_{pi}/r_{max})^p$, and where r_{pi} is the plastic area associated with the loading cycle, r_{max} is the distance from the current crack tip to the largest prior elastic-plastic area created by the overload, and the exponent p is dependent on the material and load spectrum.

The model proposed by Wheeler [115] assumes that crack growth rate is related to the interaction of crack tip plasticity affected by residual compressive stresses created by overloads. Another similar model [116] based on crack tip plasticity introduced variations in the crack tip stress intensity, ΔK_i, to reduce this factor to an

51

effective stress intensity range (ΔK_{eff}). This was to account for the increased residual compressive stress created by the overload.

In many instances the current design methodology based on LEFM provides an accurate estimate of fatigue life when the initial size of the fatigue flaw is larger than 0.3mm [40]. There are however, a number of fatigue critical components such as turbine discs and blades, whose design considerations fall outside the boundary of LEFM. Hudak et al [117] indicated that life predictions based on LEFM may be non-conservative for a nickel-base superalloy - Astroloy (a disc material for aircraft gas turbine engine). An area of concern that was emphasised by a review made by Cowles [118] in 1996, who reported that approximately 24% of fatigue failures in military gas turbine jet engines were as a result of HCF. Indicating that LEFM cannot readily account for damage in the short crack regime a region that is dominant in HCF, which is a view that is increasingly acknowledged today.

There is wide acceptance that components subjected to HCF require a greater understanding of the influence fatigue cracks having significantly smaller dimensions i.e. short cracks, have on fatigue lifetime. This is especially so for the extremely long-lifetime regime ($10^7 < Nf < 10^{12}$ cycles to failure) where MFM and EPFM play a primary role in the overall fatigue life [32]. Therefore, other approaches for fatigue damage accumulation [105][106] are necessary to take into account the effects of short fatigue cracks.

To account for damage accumulation for crack initiation and Stage I growth Miller and Zachariah [119] introduced an exponential relationship between crack length

and the life for each phase, an approach which is termed - double exponent law. Later Miller and Ibrahim [120] modified the model such that damage accumulation in the short crack propagation phase is related to EPFM crack growth of the form,

$$da/dN = \phi \ (\Delta\gamma_p)^\alpha \ a \ \text{...} (2.21)$$

where ϕ and α are material constants, and γ_p is the plastic shear range.

More recently Miller *et al* [121] examined the effects of increasing stress amplitude for a 0.4% carbon steel and used a two-stage crack growth method to predict cumulative fatigue damage. Miller [121] used crack growth models proposed by Hobson [93] by applying derivations based on the short and long crack growth rate expressions of the form,

for short cracks

$$da/dN = A \ (\Delta\gamma_p)^n \ (d - a); \text{...} (2.22)$$

and for long cracks

$$da/dN = B \ (\Delta\gamma_p)^m \ a - C \ \text{...} (2.23)$$

where A, B, C, m and n are material constants, $\Delta\gamma_p$ is the plastic shear range, d represents the distance to the major microstructural boundary and a is crack length.

Comparisons made of the above crack growth models, with the Corten-Dolan-Marsh method and Palmgren-Miner method for fatigue life predictions, indicated the latter two methods to be somewhat non-conservative as shown in Fig 2.13.
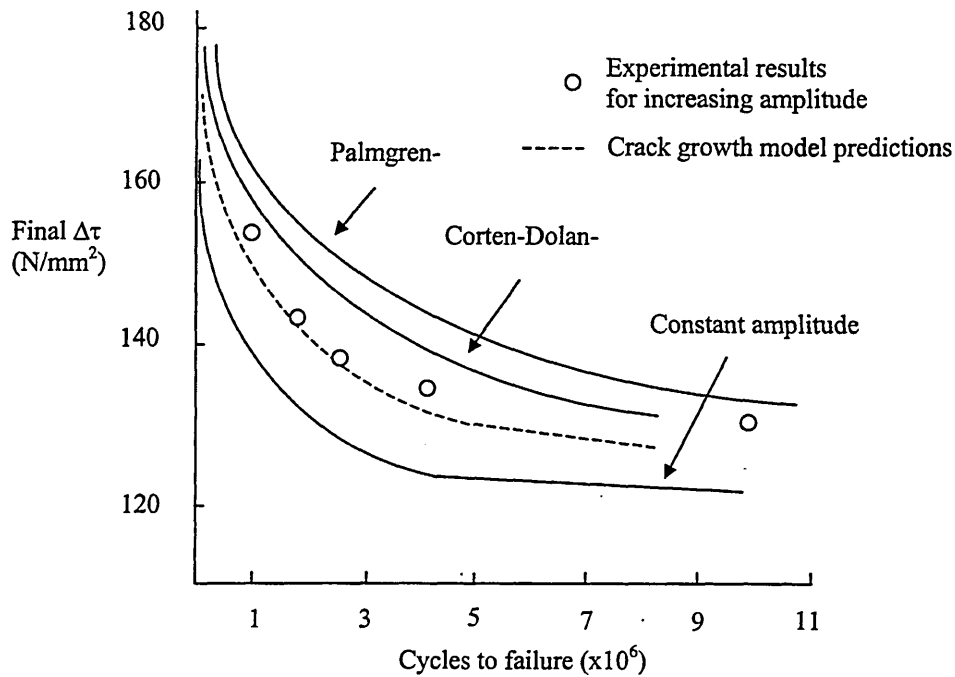

Fig. 2.13 Lifetime predictions of the three models: (i) Palmgren-Miner,
(ii) Corten-Dolan-Marsh (iii) short and long crack growth equation [42]

It is acknowledged that for sequential loading of the same stress state that non-conformity to LDR can be conservative or non-conservative, for cases where the load changes from L-H or H-L in the loading sequence. However, non-conformity to the LDR has been reported for stress-strain states that give the same endurance (4 x 10^5 cycles) in reversed torsion and push-pull loading in sequential loading [51]. In this instance the fatigue lifetimes can be changed dramatically depending on which loading mode is applied first. The effects of push-pull - torsion sequential loading and vice versa are shown in Fig. 2.14, and where reportedly [51] the Palmgren-

Miner hypothesis is approximately applicable if a single cracking system is dominant throughout lifetime.
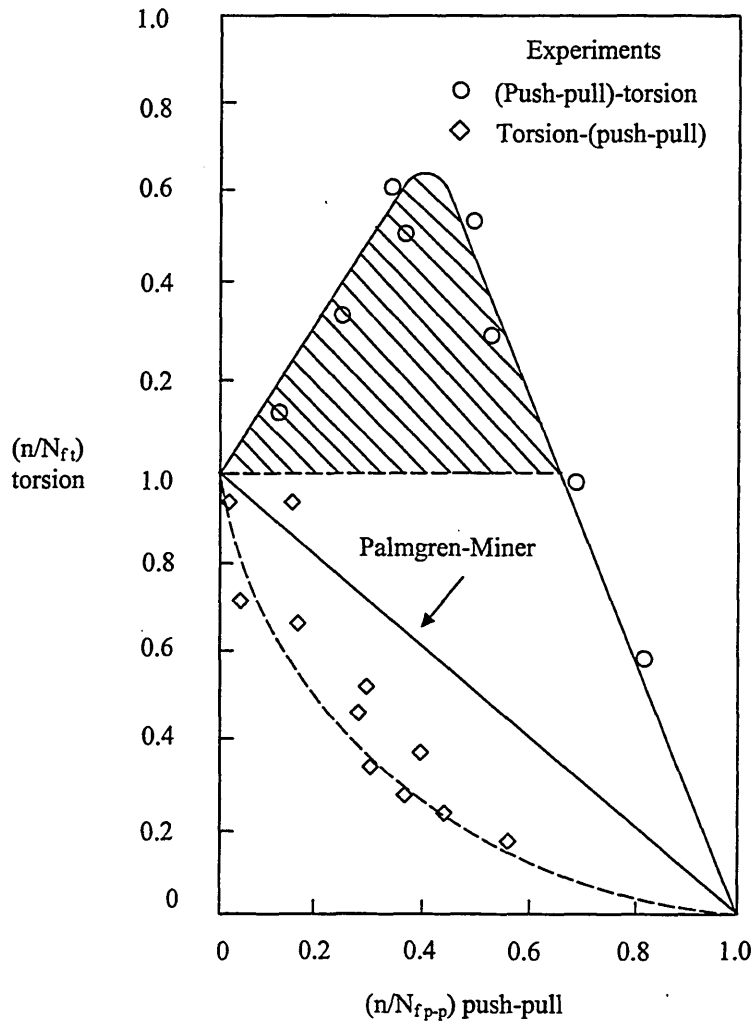
Fig. 2.14 The effects of push-pull - torsion sequential loading and vice versa [51]

($\Delta\sigma$ = 598 MPa, $N_{f p-p}$ = 4 x 10^5 cycles and $\Delta\tau$ = 413 MPa, $N_{f t}$ = 4 x 10^5 cycles)

Fig 2.14 also shows that for increasing fatigue life, the departure from Miner's rule can be quite severe for such sequences and can be considerably non-conservative as a consequence of the variability of loading mode.

2.8 Summary

After decades of fatigue research the understanding of complex cyclic loading is still incomplete and as such the answers to all fatigue related problems is still not definitive. Some advances have been made in particular areas of fatigue life assessment with the development of predictive fatigue life models, but none has universal acceptance. The complexity of the problem generally allows the models to account for only one or more factors [107] i.e. load dependence, multiple damage stages, non-linear damage evolution, load sequence and interaction effects, overload effects, small amplitude cycles below fatigue limit and mean stress. The effect these phenomenological factors have on fatigue lifetime, present problems in establishing simple predictive models that can account for cumulative fatigue damage.

The consequences of inadequate fatigue knowledge is often reflected in design analysis, which can be subject to compromise to allow for the unknown and consequently result in over-engineering and expensive monitoring of the engineering components in service. Therefore waste is inevitable in this context where fatigue behaviour is difficult to ascertain, the results of which can affect 'sustainability' which is a key-point made in Chapter 1.

Thus from this literature review it demonstrates objectively the necessity for the greater understanding of fatigue behaviour and the need to examine the effects on fatigue damage surrounding particular fatigue conditions that have no established fatigue criteria. Several workers [48][49][50][96][98] have examined the effects of fatigue damage accumulation under torsion and push-pull loading for different

loading regimes. But, the crack growth data obtained from these loading systems and others cannot necessarily be extended to other similar loading systems to establish reliable predictive fatigue criteria. This is because the unknowns surrounding crack-load interactions can differ considerably for different loading conditions and as yet the understanding is not complete and further research is necessary.

The current work therefore, focuses on a torsion loading case of how torsion Stage I crack growth and the subsequent torsion fatigue lifetimes of 0.42% carbon steel specimens are affected by the introduction of a non-proportional interrupted push-pull loading. Whereby for all the tests the fully reversed torsion loading remains constant for a stress range of $\Delta\tau = 410MPa$ that corresponds to a torsion fatigue lifetime of 1.8×10^6 cycles. The push-pull load interruption is applied after various prior torsion cycle ratios of 0.22, 0.26, 0.33, 0.53 and 0.73 n_1/N_{f1}. The prior torsion cycle ratios are selected so that no torsion Stage II crack growth prevails under the initial torsion loading. The influence on torsion fatigue life is examined under different push-pull load stress ranges of 600, 640, 760 and 820 MPa. The push-pull load interruption represents limited damage of only 4% according to LDR, chosen to examine the effects of minimal multiaxiality of loading on the specimens.

Furthermore as outlined in the literature review the LDR is still widely used today despite of its major shortcomings, which makes it extremely important that any deficiencies of the LDR are highlighted, especially where multiaxial loading is concerned. Since as shown by this case of multiaxial sequential loading, although the fatigue cycles of an interrupted load may seem innocuous, the effect can be more damaging compared to the LDR.

Chapter 3

Experimental Work

3.1 Introduction

To facilitate this research testing programme one of the main criteria was the design of a new specimen-loading set-up for the biaxial test machine. This was necessary because the biaxial test machine used for the experimental programme had originally been designed and used only for fretting experimental work. Therefore a new facility to apply the required multiaxial torsion and push-pull loading required for this work, was designed, fitted and commissioned prior to the experimental test programme.

The specimen material used for the test programme was conventional industrial medium carbon steel.

The experimental programme involved various combinations of non-proportional sequential loading. The loading sequence involved initially torsion, followed by push-pull and then torsion to failure.

The following sections and sub-sections of this chapter outline, the material used for the experimental work, the specimen - profile, preparation, surface profile measurements, section measurements, microstructure, grain size counts, the multiaxial test machine and the associated new design for torsion and push-pull

cyclic loading, the torque measurement system, the experimental procedures, test programme and the definition of failure for the specimen.

3.2 Material

The material used in this research work was a medium carbon steel which had the following specification - BS 970 080A42 cold finished bright bar manufactured to BS EN ISO 9002:1994. The material had the following nominal chemical composition (weight %), as shown in Table 3.1.

Table 3.1 Nominal chemical composition of the medium carbon steel

C	Si	Mn	P	S
0.421	0.219	0.78	0.011	0.008

The mechanical properties of the specimen material were obtained by carrying out tensile tests on a 20kN capacity test machine manufactured by J. J. Lloyd. Fig. 3.1 shows the engineering stress-strain curve for the material and the specimen geometry used for the tensile test.

The test pieces for the tensile tests were manufactured from off-cuts of the specimen bar material and machined to the profile as shown in Fig. 3.1. The mean results of the three tensile tests were,

Ultimate strength .... 730 MPa

Yield strength .... 499 MPa

RA 34%

Elongation 14%
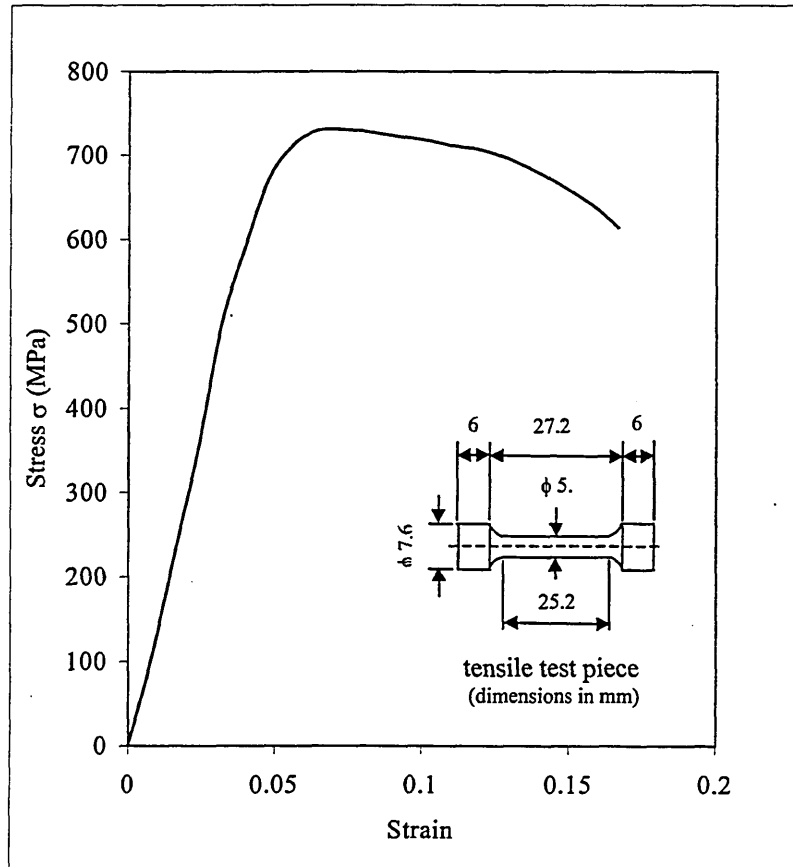

Fig. 3.1 Monotonic tension stress-strain curve

The hardness of the material was measured using a Vickers diamond indenter machine. Seven specimens were tested and these were indented on the largest diameter (25mm section - the section that was not subjected to any fatigue loading) using a 20kg indentation mass and the mean Vickers hardness number calculated from the results was 217.

3.3 Specimen

The specimens used for the test programme were solid, having a machined hourglass

profile as shown in Fig. 3.2.
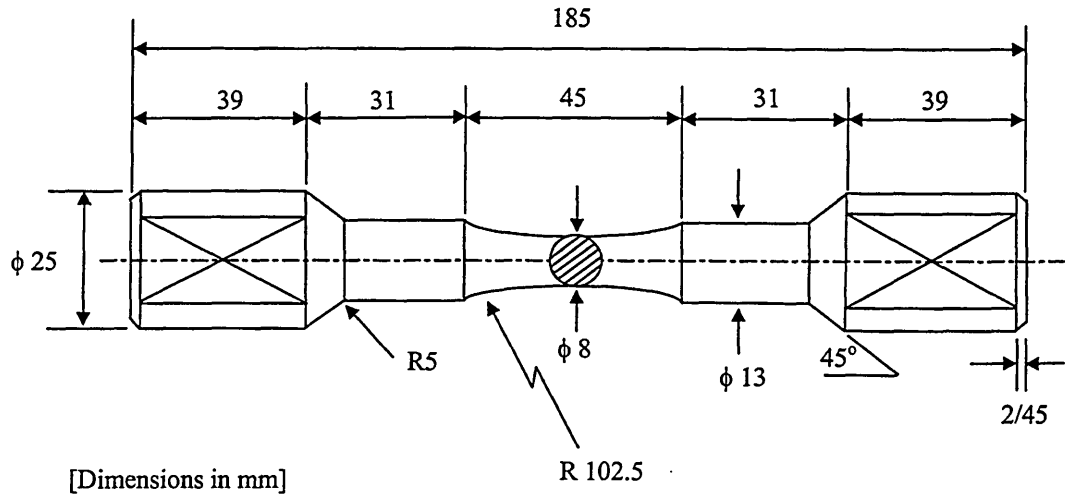
Fig.3.2 Test specimen geometry

The specimens were manufactured from 25mm diameter cold finished bright bar

material purchased locally from a steel stockist and machined to the required profile

using a CNC machine in the University's workshop. The specimens were not

subjected to any specific material refining or heat treatment process, because the

experimental tests were to study the fatigue characteristic of a material in the

annealed and normalised ferrite and pearlite condition.

3.3.1 Specimen Preparation

The specimens were numbered prior to the preparation of the surface with a prefix

letter 'T' for the constant amplitude tests and 'S' for the sequential loading tests. The

hour glass section of the specimens was polished, first, with silicon carbide paper by the application of successive finer grades of 320, 400, 600, 800 and 1200, and then with diamond pastes of 6μm and 1μm respectively. The polishing was carried out in the longitudinal direction on the hour glass section in accordance with BS 3518 : Part 3 : 1963 Section 6 - Preparation of test piece - Surface finishing paragraph (6e). The polished test specimens had an appropriate mirror like finish free of any machining marks or scratches as illustrated by the sample test specimen in Fig. 3.3.
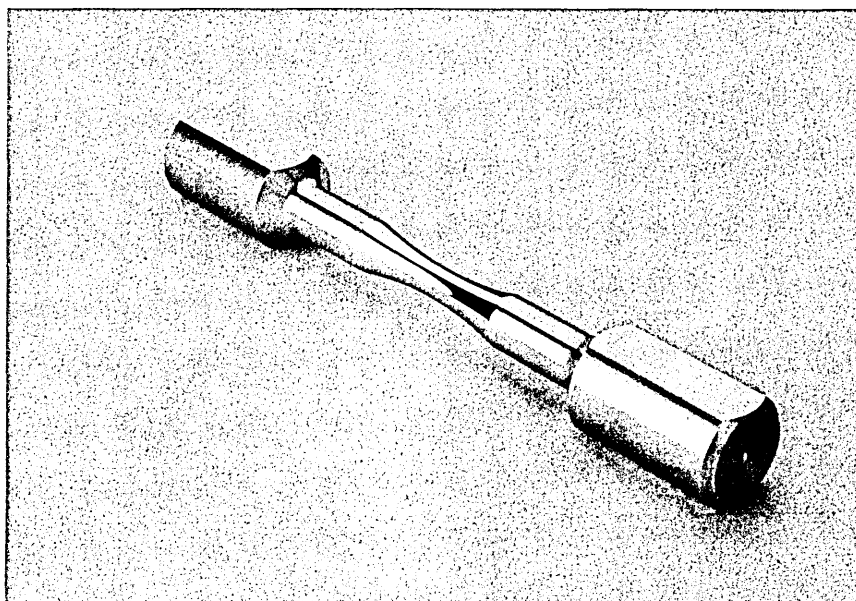

Fig. 3.3 Test specimen

3.3.2 Specimen Surface Profile Measurement

To ensure that the polished surface of specimens had some consistency of finish and an acceptable level of surface roughness, three specimens were examined using a Taylor-Hobson surface-measuring machine in the University's Metrology laboratory.

The principle operation of the machine is that a diamond stylus having a radius profile (2μm radius) is traversed across the hour glass section of the surface of the specimen in a longitudinal direction. The vertical movements of the stylus are measured coincidentally by the machine with the aid of laser beam displacement technology and converted into electrical signals by the so-called gauge. Different types of gauges are used for varying applications of surface roughness measurement and the type used in this machine was a laser interferometric gauge with digital transducers. It is a gauge that is very responsive to stylus movement and has a gauge resolution in the order of 10nm. A close-up illustration of a test specimen with the stylus in contact with the surface of the specimen is shown in Fig. 3.4.
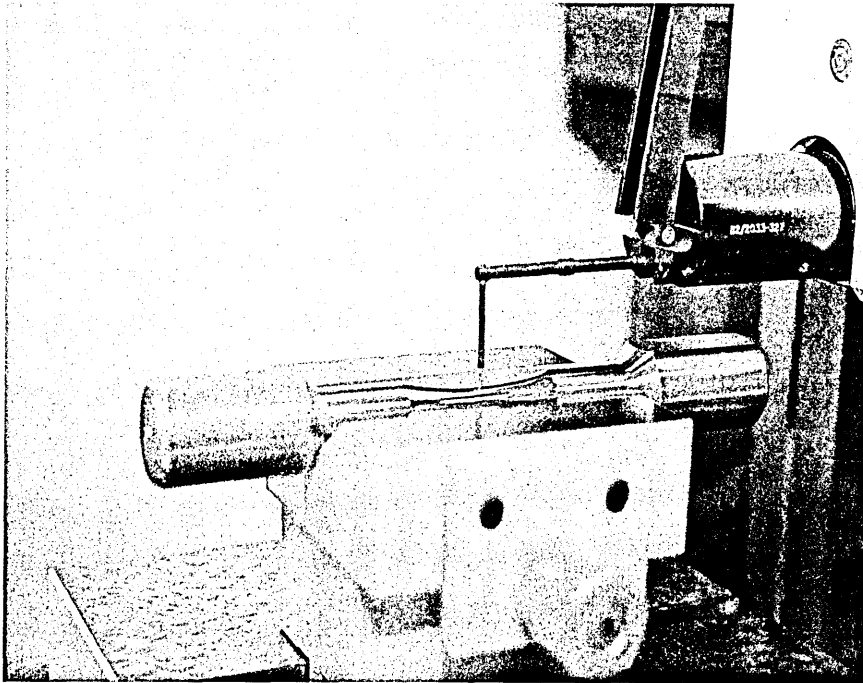

Fig. 3.4 Illustration of a test specimen and stylus set-up of the measuring machine

An illustration of the complete Taylor-Hobson surface measuring machine is shown in Appendix 1.

The vertical movements of the stylus are converted by the transducers to digital outputs, analysed, and recorded by the computer interface to give the surface roughness measurements and graphic display. The recorded maximum values for the surface valley measurement (R_v) and the surface roughness (R_a) were 1.04μm and 0.031μm respectively. For this work it is considered pertinent to use the R_v value for fatigue evaluation, since microscopic valleys are probably the likeliest sites for accelerated crack initiation. Although in this case not necessarily where R_v is a maximum on the specimen. The surface profile measurement trace recorded by the surface measuring machine is shown in Fig. 3.5.
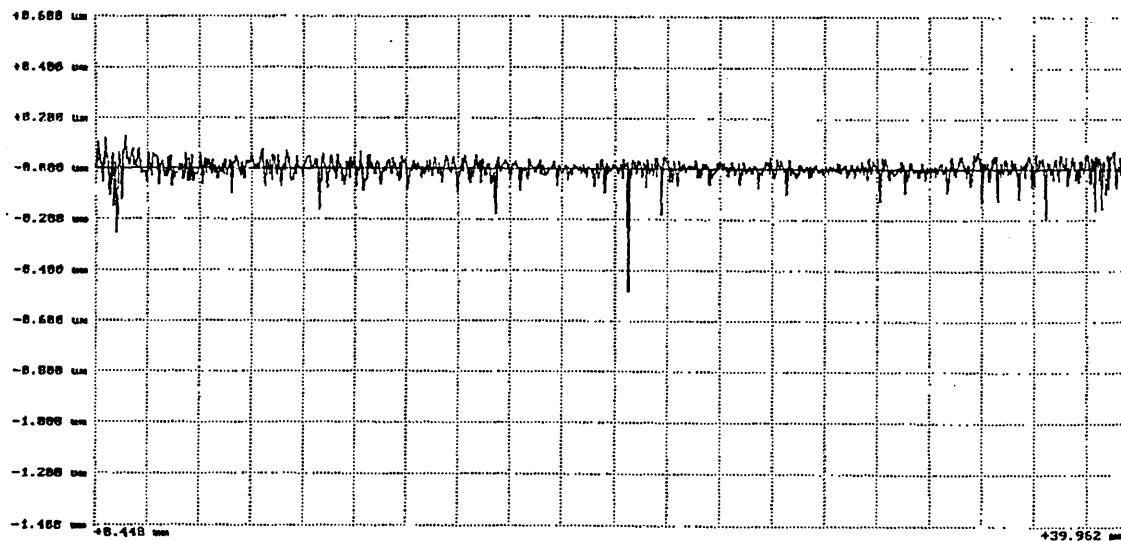

Fig. 3.5 Surface measurements of a test specimen profile

The recorded values of R_v and R_a are considered well within the acceptable levels for fatigue analysis since it has been suggested that crack growth from 0 to 3μm makes minimal difference to fatigue lifetime [30]. Therefore, the measured surface

roughness results indicate that the method used is appropriate for the surface preparation of the test specimens.

3.3.3 Measurement of Specimen Section

The minimum diameter (d_{min}) of the hour glass section of the specimen was obtained using the Societe Genovoise MU-214B universal measuring machine as shown by the illustration in Appendix 2. The specimen was mounted in V-supports blocks secured to the machine table which facilitated accurate alignment for measuring and enabled easy rotational movement to change measuring position. Two sets of measurements were taken in positions ~ 90° apart and the mean of the two results were taken to represent d_{min}. The precise measurements for d_{min} is achieved by the aid of the two reading microscopes which are integral with the machine and record displacement of the microscope attachment in the 'x', 'y', and 'z' planes. A spherical-ended 6mm-diameter microscope attachment was used for this work and the principle of the measuring technique is shown schematically illustrated in Fig.3.6.

The measurement of d_{min} by this method although it is more time consuming than the more conventional method of a point micrometer, accuracy is more precise and consistent since there is no dependency on experience and feel which is necessary with a micrometer. This method also has the additional benefit that its use prevents any undesirable surface indentations and scratches on the surface of the specimen that can result from the use of a point micrometer. A factor that is especially important for this work involving HCF testing since such surface markings could be sites that lead to premature crack initiation.
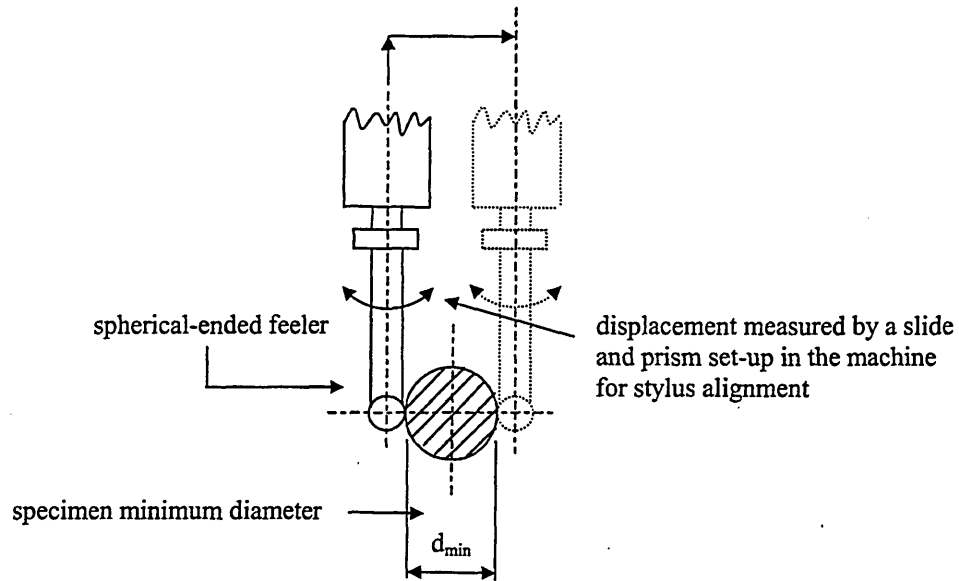
Fig. 3.6 Schematic of the feeler measuring system

3.3.4 Specimen Microstructure

The microstructure of the specimen consists of ferrite and pearlite grains, which is typical of a medium carbon steel grain structure as shown in Figs. 3.7 (a-d). The illustrations shown are viewed with decreasing magnification to demonstrate the characteristics of the ferritic and pearlitic regions of this particular medium carbon steel. The micrographs show the considerable differences in grain size and shape that are randomly distributed throughout the material. The complexity of the grain structure clearly illustrates the obstacles to MSC growth i.e. grain boundaries and the stronger pearlite regions, and why grain size in particular is important in short crack growth as discussed earlier in Chapter 2.

(a)

(b)

67
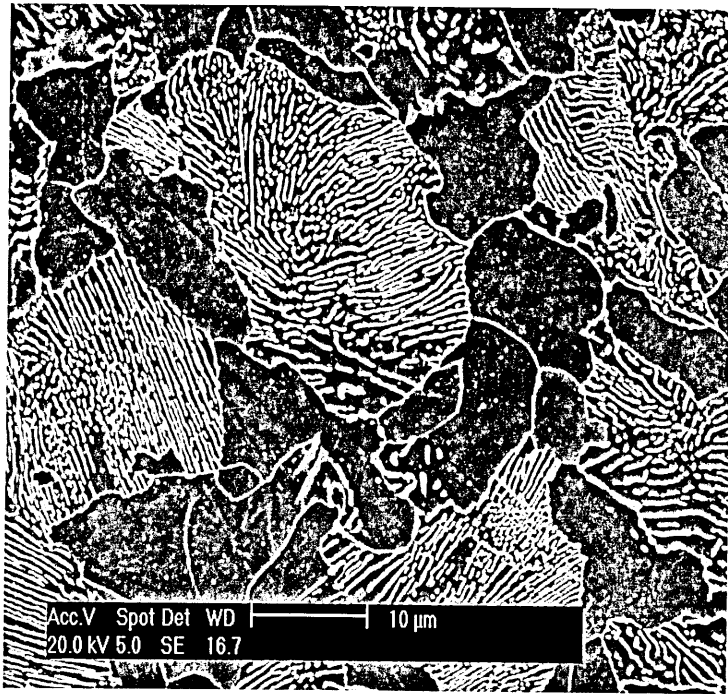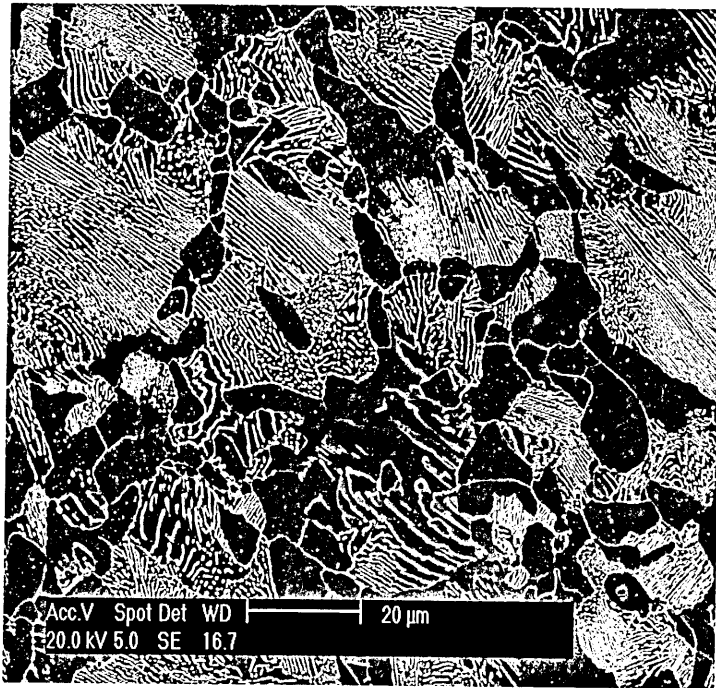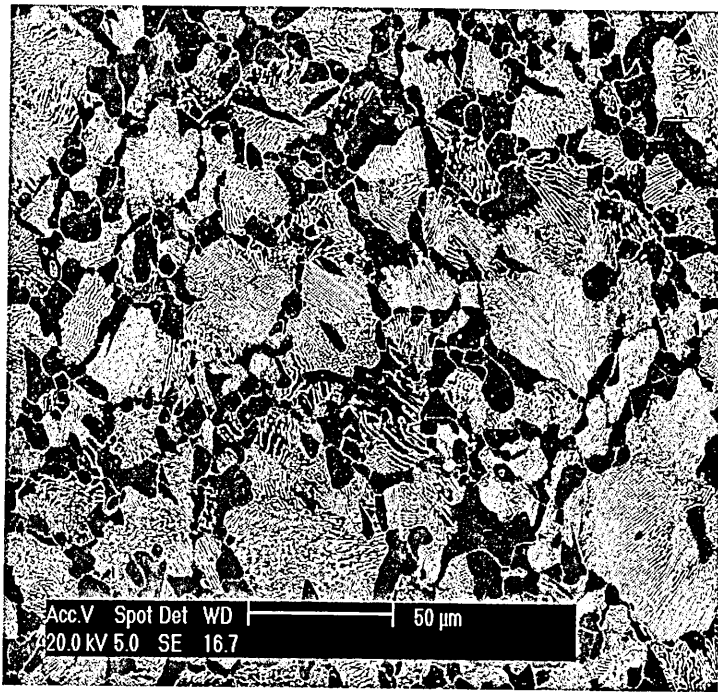
(c)
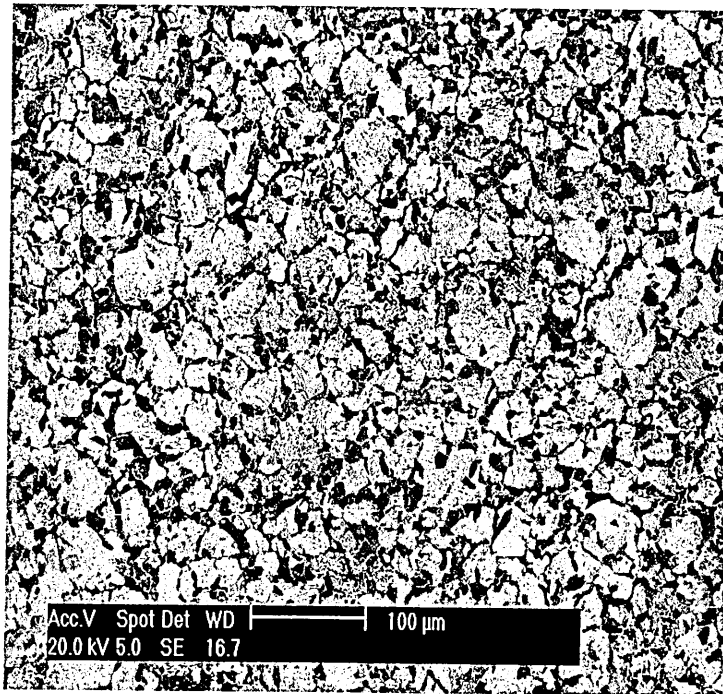
(d)

Figs. 3.7 (a-d) Specimen grain structure (medium carbon steel)

3.3.5 Analysis of Ferrite Grain Sizes

As discussed in Chapter 2 the modelling of short crack growth was to be based on the MSC growth equation (2.11). The parameter d used in the equation is approximated to ferrite grain sizes of the material, as illustrated in Fig 2.8. The ferrite grain size is used because they are the weaker grains (pearlite stronger) and cracks generally initiate in the larger grains as discussed in Chapter 2. Therefore the parameter (d_1) in the model is taken as the upper limit of grain size and the parameters $(d_2, d_3, d_4, \ldots)$ taken as the mean ferrite grain size. Therefore the upper and mean ferrite grain sizes were determined from the material's microstructure by preparing a sample from an unused specimen. The specimen was sectioned so that the surface area used for grain size analysis was taken normal to the specimen surface to account for any grain size directionality from previous manufacturing processes i.e. cold rolling operations.

The ferrite grain sizes were measured using an Image analyser in the University's - Materials Research Institute laboratory. The machine analyses the grain structures of materials and computes the grain counts using the recognised BS 4490 : 1989 - Micrographic determination of the grain size of steel; or the ASTM designation: E 112-95 - Standard test methods for the determination of grain size.

The field areas for each of the ferrite grain counts was approximately $1.8 \times 10^4 \ \mu m^2$ and ferrite grains counted for the field areas that were between 32 to 89. However, to get a good representative sample for the ferrite grain sizes, 20 field areas were taken and these were chosen randomly on the prepared surface. This obviously resulted in

varying ferrite grain sizes for each count taken, but, these differences are not unexpected when considering the irregularity of the grain structure of the material.

The irregularity in grain structure was also an important factor in which method was used for the determination of the ferrite grain sizes analytically, since grain shape can effect the results considerably as was found by using the interpolated grain area method. The best method that was considered to give the most accurate computed results, was the mean linear intercept method as detailed in the ASTM E 112-95. When the results from this method of the ferrite grain sizes for this material were compared against sample hand counts they were found to be in good agreement. The ferrite grain size results obtained by the mean linear intercept method were subsequently used for the crack growth model predictions.

Figs. 3.8 (a) and (b) are two of the micrographs that were used for the ferrite grain analysis. Correspondingly a sample field summary result sheet is shown in Fig. 3.9 that outlines the computed data obtained from one of the micrographs that was used for the grain size determination, in particular the maximum and mean grain sizes. For information the maximum and mean grain size results used, are denoted by the max and mean terms respectively that are given in the field summary column in Fig. 3.9.

Fig.3.8 (a) Micrograph of field area (1) used for grain size analysis

Fig 3.8 (b) Micrograph of field area (5) used for grain size analysis
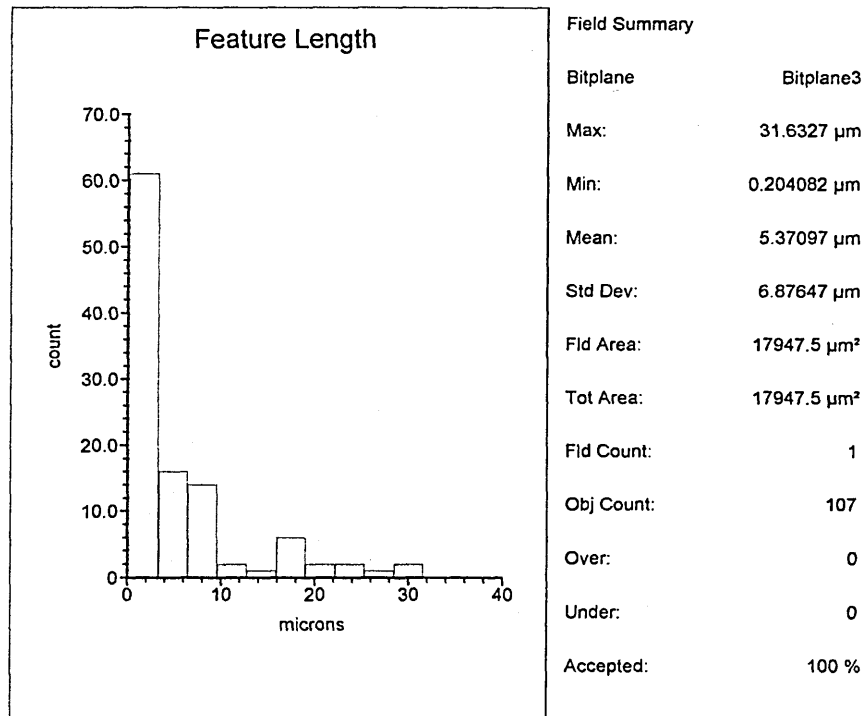
Fig.3.9 A sample field summary result sheet for ferrite grain count

3.4 Multiaxial Test Machine

Multiaxial test machines vary in configuration to enable different experimental fatigue tests to be performed and there are a number of different types described in past literature [20][29][122]. The machine used for the current test programme is a closed-loop servo hydraulic test machine that comprises of four actuators, two positioned in the vertical axis and two in the horizontal axis. The movement of all the actuators are purely axial centred on the x and y planes contained within the predetermined structural envelope of the machine as illustrated in Fig. 3.10.

Fig 3.10 Multiaxial testing machine set-up for torsion and push-pull cyclic loading

The control parameters for the actuators can be for either axial load (with a range of ± 0-250kN), or stroke (with a range of ± 0-25mm). The electronic control unit has an in-built variable-phase signal generator having two oscillators of the switched integrator type, generating a sinusoidal waveform. There are two other auxiliary outputs; square and triangular wave, however, for the current works only the sinusoidal wave was used. One of the oscillators is variable phase, switched to be either leading or lagging from the other reference phase. The frequency range of the signal generator is from 0.01Hz to 1kHz, although the maximum frequency achievable for torsion loading was of the order of 10Hz with the present hydraulic servo set-up.

Fig 3.10 Multiaxial testing machine set-up for torsion and push-pull cyclic loading

The control parameters for the actuators can be for either axial load (with a range of ± 0-250kN), or stroke (with a range of ± 0-25mm). The electronic control unit has an in-built variable-phase signal generator having two oscillators of the switched integrator type, generating a sinusoidal waveform. There are two other auxiliary outputs; square and triangular wave, however, for the current works only the sinusoidal wave was used. One of the oscillators is variable phase, switched to be either leading or lagging from the other reference phase. The frequency range of the signal generator is from 0.01Hz to 1kHz, although the maximum frequency achievable for torsion loading was of the order of 10Hz with the present hydraulic servo set-up.

3.4.1 New Design for Torsion and Push-Pull Cyclic Loading

The biaxial machine used for the current test programme had no facilities to apply push-pull and torsion loading, so a new design arrangement had to be thought through, designed and manufactured. The detailed design drawings for the push-pull and torsion loading are outlined in Appendix 3.

The objective of the new design features was to incorporate engineering simplicity whilst maintaining practical functionality for the testing application. Especially for the application of the torsion loading which was the main consideration of the new design arrangement. This was because load transfer from the reciprocating actuators to develop the necessary shear strain on the specimen is the more complex to realise effectively. Also any design arrangement had to be accommodated within the constraints of the machine's structural envelope that encompasses the location and operational space of the biaxial actuators. This meant that any proposed design arrangement had component size limitations whilst considerations had to be given to the maximum design loading capabilities of the machine. Although it was possible to limit the load control settings to be within the constraints of the proposed design arrangement. To the effect that the settings were selected in the range of $\pm$ 0-50 kN for the axial load range and $\pm$ 0-5 mm for the stroke range to accommodate safely the push-pull loading and torsion cyclic straining respectively. The appropriate control trip settings also gave over-riding protection in the event of accidental overloading, but, it is important to note that the trips are only effective if the correct load and stroke ranges are selected.

The new design arrangement centred on the principle to apply the torsion loading, since obviously load transfer for torsion loading by actuators involves a more complex design arrangement to that for push-pull loading. The design principle that met the above requirements for applying the torsion and push-pull loading is shown schematically in Fig. 3.11.
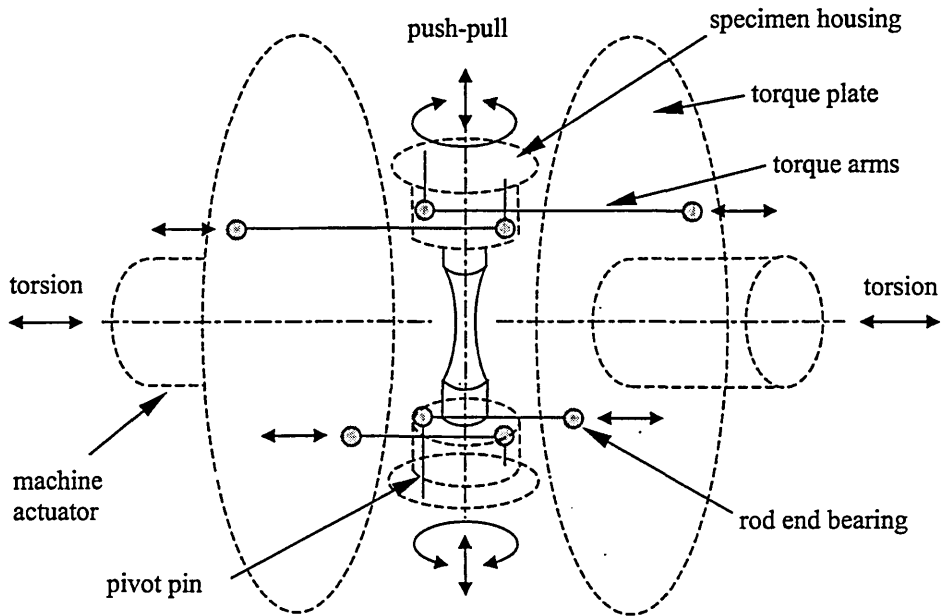
Fig. 3.11 Schematic of the principle of the loading arrangement

To eliminate any unwanted bending stress on the specimen, the torsion mechanisms were designed such that there was no net lateral load on the specimen due to torsion. The basic design arrangement for the torsion loading was achieved by bolting circular torque plates (see Fig. 3.11) on to the horizontal actuator load cells. To ensure accurate dimensional tolerance for the fit of the torque plates and specimen housings to the load cells. Consequently the load cell spigot bore dimensions (see Fig

75

3.12) were checked in the Metrology laboratory using Societe Genovoise MU-214B universal measuring machine. The recorded load cell spigot dimensions are shown in Table 3.1 and for supplementary information a diagram of the load cell is shown in Fig. 3.12.

Table 3.1 Spigot dimensions of the load cells

diametrical position	spigot axial position	Load cell No 1535A	Load cell No 1535B	Load cell No 1535C	Load cell No 1535D
0°	top (mm)	136.152	136.04	136.222	136.046
	middle (mm)	136.101	136.028	136.211	136.031
	bottom (mm)	136.068	136.009	136.182	136.022
90°	top (mm)	136.112	136.057	136.168	136.045
	middle (mm)	136.078	136.047	136.146	136.027
	bottom (mm)	136.073	136.013	136.108	136.018
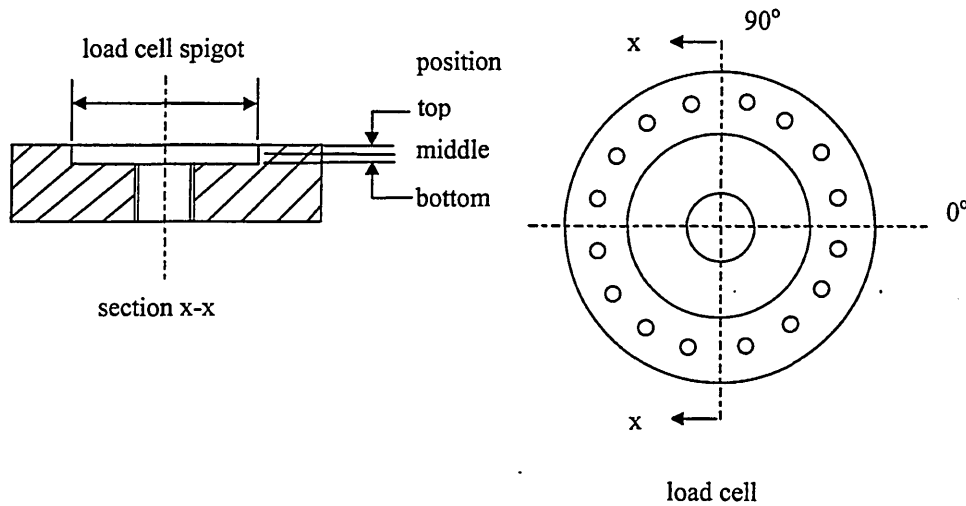
Fig. 3.12 Diagram of load cell

It is worth noting that although simpler diagonal fixings could have been designed for the torsion-loading requirement. The torque plates were purposely designed circular for positive and correct location to the existing load cell circular recessed

spigot, ease of ensuring correct alignment for the torque arm axes (could be indexed drilled for accuracy) and flexibility of use for further applications.

In order to provide the necessary turning moment for the torsion loading the torque plate was linked to the specimen housing by torque arms as illustrated in Fig. 3.13.
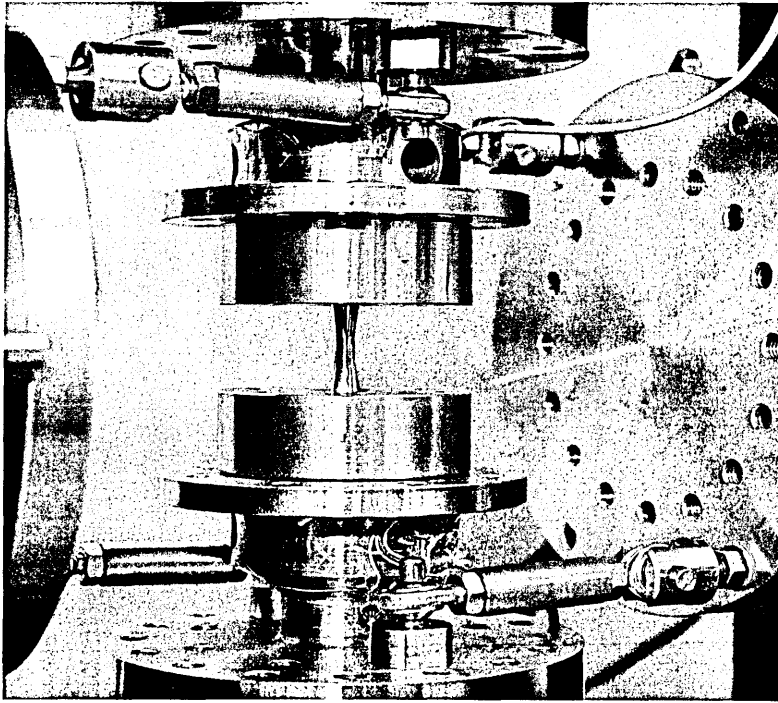
Fig. 3.13 Illustration of torsion mechanisms

The torque arms were positioned diagonally on the torque plate to give the necessary horizontal offset from the actuator axis to facilitate rotational movement of the specimen housing. Which in turn applied the controlled shear strain to the specimen. The torque arm end fixings had a screw fastening to the torque plate and a bearing connection at the pivot pin on the specimen housing. The reason for incorporating

end pivot bearing mechanisms was to ensure minimal backlash and thereby maintain a smooth load waveform with minimal peak transient effect.

The bearing mechanisms were precision rod end bearings, supplied by IKO Nippon Thompson having a dynamic load capacity of 2 kN, which gave a component factor of safety of 12:1. The rod end bearing was chosen also to afford a good fit to limit the tolerance in the pivot mechanism. The mechanisms were greased on assembly to reduce the effects of fretting, especially on the contact areas of the pivot pins, although any appreciable wear effects could be easily monitored by inspection after each test. The torque arm mechanism gave adequate control for the reciprocating motion whilst allowing for the relatively slight rotational movement during cycling. The torque arm connection to the torque plate was designed to give fine longitudinal adjustment to facilitate accurate set-up. This allowed precise positional control so that zero loading on all torque arms was achieved prior to the strain application. The zero load values were accurately sensed by the load cells and displayed on the control panel of the machine.

To prevent any rotational movement during cycling, the actuators that applied the torsion loading were fitted with side stabilising rod assemblies, two for each actuator. These were mounted on to the supporting structure of the machine as shown in Fig. 3.14. The stabilising rods were aligned horizontally by the aid of a dial gauge, to give the necessary relative positional accuracy to the torque plate load cell-interconnecting fixture. The stabilising fixture (see Fig. 3.14) that was bolted to the load cell, had adjustable screws (see Fig. 3.14) that were positioned diametrically opposite in the hole of the fixture that the stabilising rod passed through. The screw

design ensured that there was adequate contact pressure to give the appropriate degree of stabilisation, whilst affording compensation for any wear taking place as a result of successive testing. Even so the stabilising rod and screw faces were adequately lubricated by grease, prior to each test to limit wear. Although it was considered that any marginal amounts of wear would have an insignificant affect on the attitude of loading during testing.
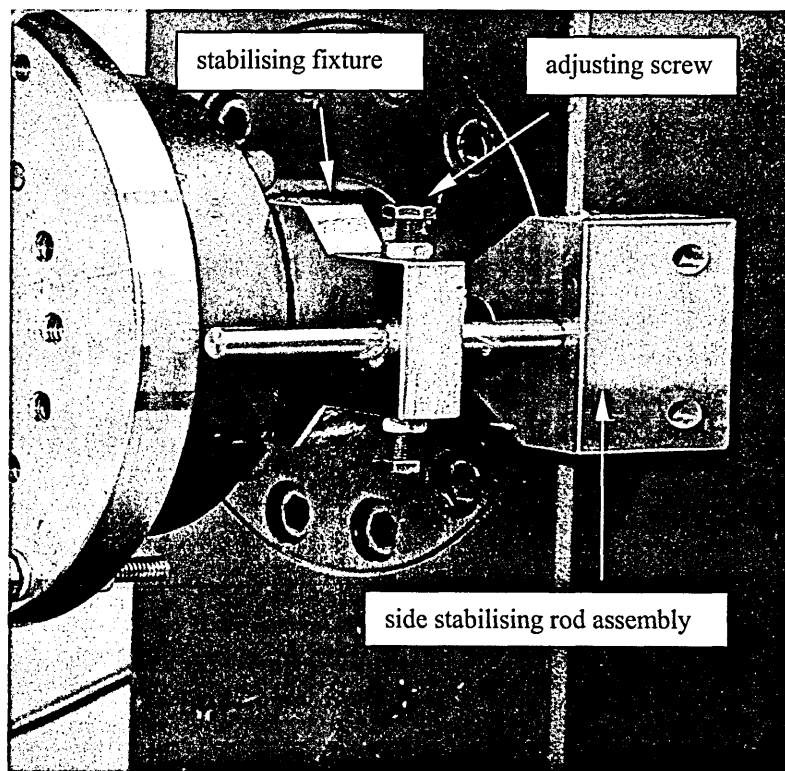
Fig. 3.14 Illustration of the side stabiliser rod assembly

The application of the torsion loading from the specimen housing to the specimen was achieved by large grub screws located diagonally opposite in the specimen housing, which on tightening secured the specimen in a positive drive position. The contact face area of the grub screw was designed to maximise the resistive moment,

such that the diameter of the screw approximated with the face width of the specimen flat. The grub screws had a machined flat face that was ground finished and set-up to be perpendicular with the screw axis. This ensured a good contact area between the flat faces of the screw and the specimen on tightening. The design of the specimen housing also accommodated the provision to mount strain gauges that were necessary for the torque measurements associated with torsion loading.

For push-pull loading the specimen housings were bolted to the load cell faces of the two vertical actuators, again with a spigot connection for centralisation. The application of the load to the specimen incorporated the more conventional design method of split retention collets, secured in the specimen housing by a bolted spigot mounted collet retaining ring as shown by the design drawings in Appendix 3. The collet retaining ring assembly provided accurate alignment of the specimen to prevent any unwanted bending loads and thereby allowed the precise axial push-pull cyclic load application.

The new design arrangement is considered to be somewhat unique for HCF torsion testing, in so much that the design affords simplicity and practicability, yet it is an inexpensive retro-fit assembly that can be accommodated to most biaxial testing machines of similar construction. In this case it has extended the capabilities of the existing machine to perform additional experimental procedures. Especially for experimental work involving variability in multiaxial loading patterns for push-pull and torsion loading, either cyclic or monotonic and for combined or sequentially loaded cases.

3.4.2 Torque Measurement System

Since the horizontal actuators in stroke control carried out the application for the torsion loading, it was necessary initially to calibrate the machine under this condition. The calibration of the horizontal actuators of the machine was carried out by recording displacement against an applied voltage. To achieve maximum sensitivity of control set-up of the machine, the minimum stroke range of ± 0-2.5mm was selected for the torque calibration. The accurate displacement of the actuators was recorded using dial gauge. The voltage was successively increased from 0 volts in increments of 200 mV and the displacement (mm) of the actuator recorded. The results are shown by the graph of displacement verses applied voltage in Fig.3.15.
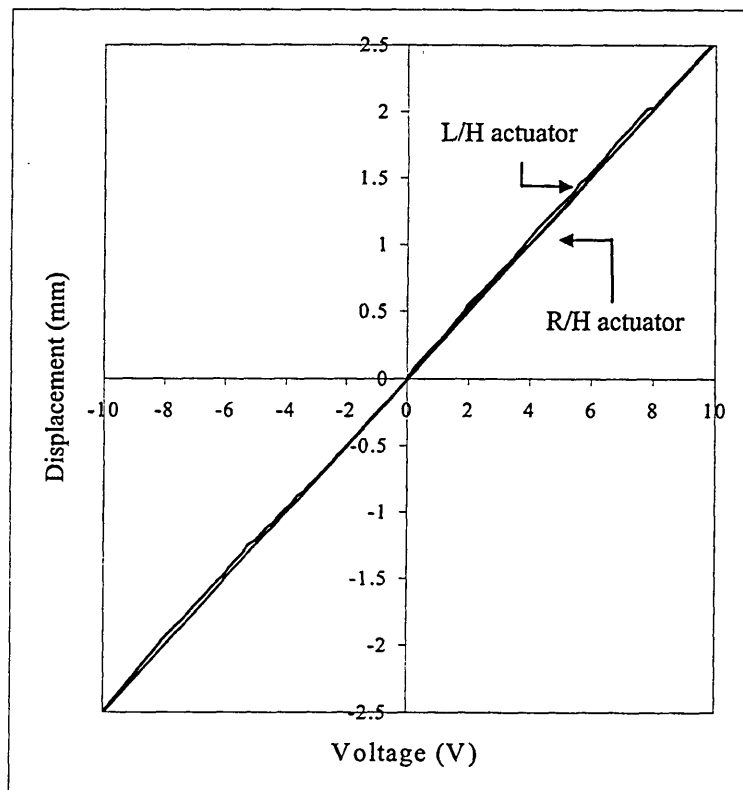
Fig. 3.15 Graph of displacement verses voltage

81

The linearity of the graph shows that the displacement of both the R/H and L/H actuators are proportion to the applied voltage and therefore demonstrated the acceptability of the machine's torsion load control system.

It is worth noting that the calibration for the push-pull loading that involved load control for the vertical actuators was not necessary because the manufacturer had previously calibrated the individual load cells.

The torque was measured using a full Wheatstone bridge composition, made up of high sensitive 350 Ω gauges suitable for 12V DC input. Rosette gauges where used for ease of installation and the gauges were cemented on to the outer centre section of the specimen housing in a four active gauge configuration. To maximise strain sensitivity whilst affording adequate strength the specimen housing had a purposely designed hollow cross section. Although to assist in overcoming the geometry constraints of the specimen housing, the gauges used were specifically selected to give high strain sensitivity. This also enabled less amplification of the output voltage from the strain gauges and in effect ensured greater accuracy of the measured torque imparted to the specimen. The gauges were also temperature compensated and so positioned on the specimen housing as to eliminate bending strain.

The DC output signal from the bridge was amplified by a FYLD (FE-379-TA) transducer amplifier which was part of a multi-channel modular instrumentation unit. The gain setting was set to within limit detection to provide the necessary stable signal appropriate for the required predetermined torque values and the strain gauge sensitivity as outlined above. A supplementary peak hold instrument FYLD (277 PH)

processed the amplified signal to determine dynamic peak ± signal values. Peak values that were also continuously recorded on a chart recorder and the recorded results showed clearly the reduction in dynamic peak voltage (drop-off in load) with time as the failure criteria is reached. Fig 3.16 shows a sample recorder sheet (part) which outlines the drop-off in dynamic peak voltage i.e. torsion load peak values.
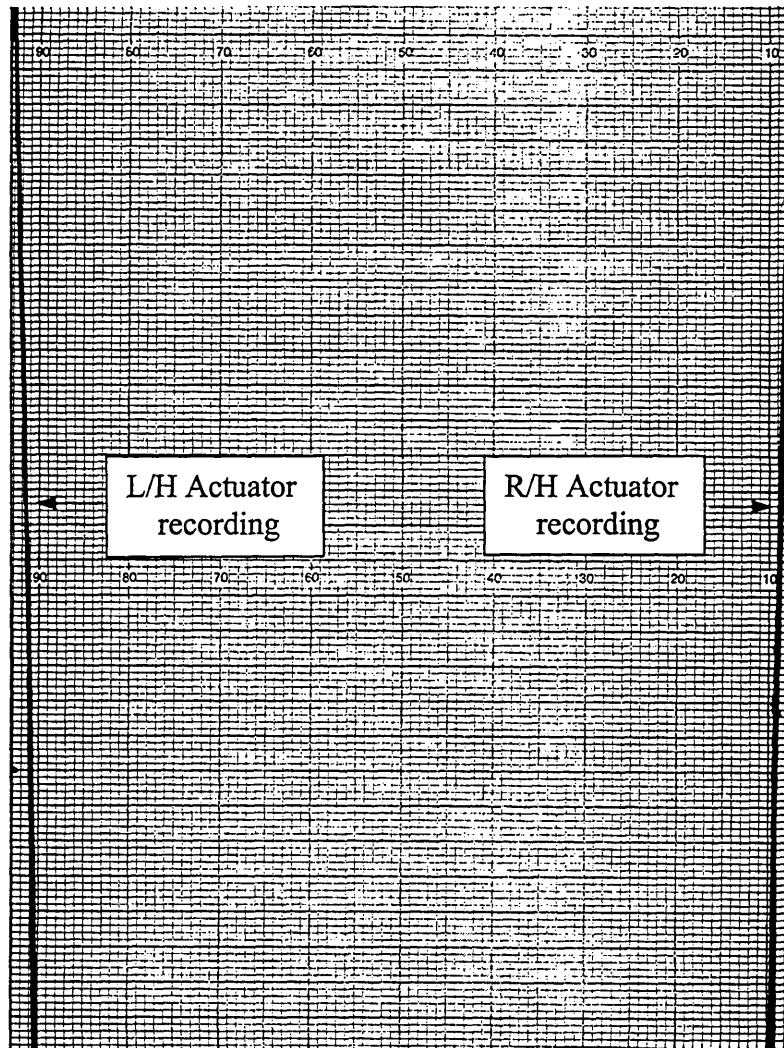
Fig. 3.16 A section of a chart recorder sheet showing the drop-off in peak value

A multi-channel Gould (DSO) 1604 oscilloscope monitored the signals for the above circuits and others from the machine control panel. The fatigue cycle count was

recorded by an integral counting unit located on the control panel that was linked internally to load sensors for predetermined trip conditions.

To calibrate the bridge circuit on the specimen housing, a known calibrated special test specimen was used. The special test specimen having been calibrated previously using a certified in-house torsion machine manufactured by Avery - Birmingham. The torque measuring system adopted is needed to eliminate any changes in extraneous load effects of seal friction from the actuator cylinders, effects that can arise from changes in oil temperature and axial load characteristics. Although the latter effect is not appropriate to this test programme since the axial loading was sequential and not combined. The full control and monitoring arrangements used during the testing programme are illustrated in Fig. 3.17
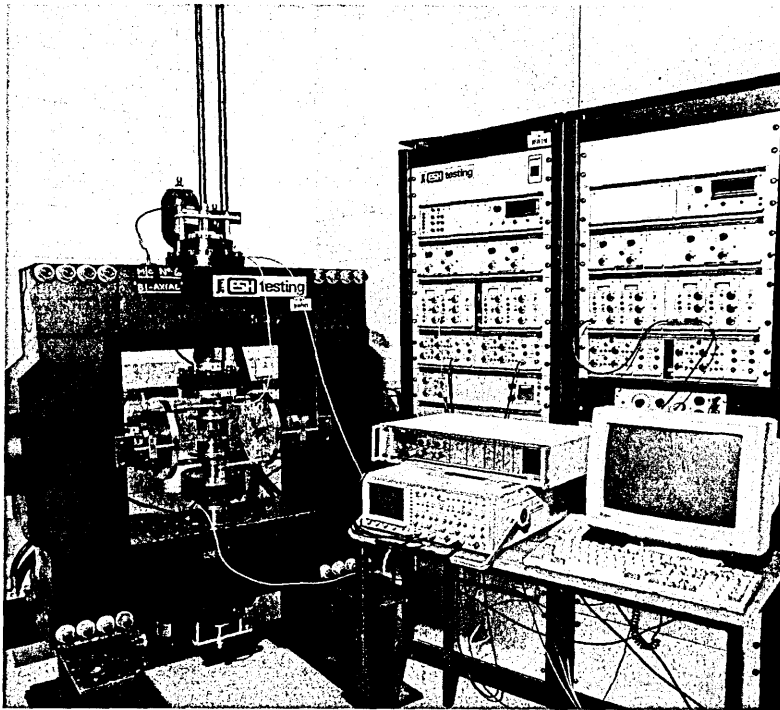
Fig. 3.17 Instrumentation for the test machine

3.5 Experimental Procedure

All the fatigue tests for the complete test programme that involved fully reversed torsion loading and fully reversed tension-compression loading were conducted at room temperature and in laboratory air. The test machine control parameters were load control (upper actuator while stroke control for the lower actuator) for push-pull loading and stroke control for the torsion loading.

(Note - The control arrangement for push-pull loading having positional control set by the lower actuator allowed for the easy set-up for the assembly of the specimens to the specimen housings and also enabled the precise positioning of the torque arms axes).

The push-pull and torsion loading fatigue tests were carried out with R = -1. The torsion shear stress was calculated using the elastic analysis and no account was made for the hour glass shape of the specimen, since comparative evaluations to other similar experimental work for pure torsion was not to be undertaken. For the multi-phase tests the torsion stress amplitude used is close to the fatigue limit and therefore no elastic- plastic analysis was necessary. For the push-pull load the tensile stress was calculated using the applied load and the minimum cross sectional area.

The analysis of fatigue crack development and fracture of the specimens subjected to multi-phase loading were studied using a SEM.

3.5.1 Test programme

The test programme set out to initially determine the fatigue characteristics of the material for pure torsion loading and pure push-pull loading, where 8 specimens were tested in each mode to obtain the respective S -N curves for the material. The S-N curves for both stress states were required for the determination of the material constants used in short crack growth models.

For the main experimental test programme 17 specimens were tested which involved multi-phase tests of non-proportional loading sequences. Tests which comprised of fully reversed torsion loading followed by a push-pull load interruption and then a continuation of the initial fully reversed torsion loading to failure as shown in Fig 3.18.
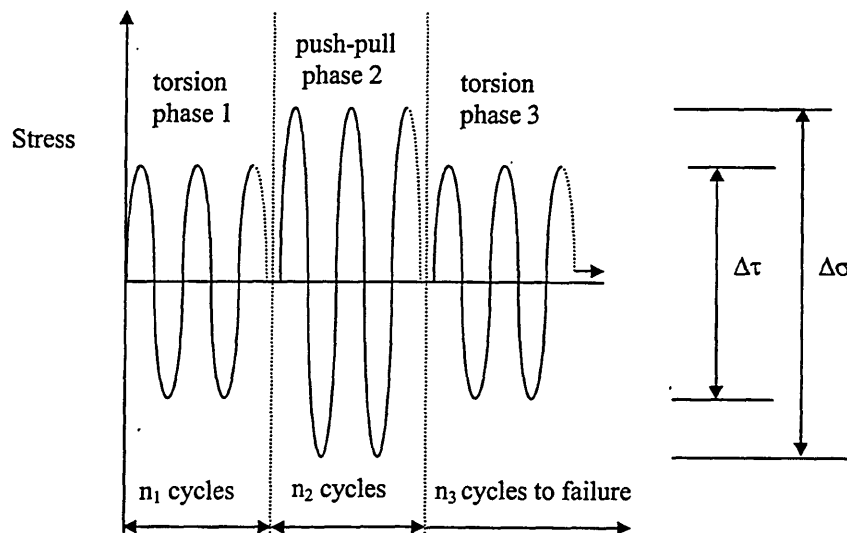
Fig. 3.18 Non-proportional loading sequence

The multi-phase test programme was undertaken to establish the effect the push-pull load interruption had on the fatigue crack growth and how this subsequently affected the torsion fatigue life. The interruption is considered to influence the propagation of the Stage I and or Stage II cracks developed under the initial and final torsion loading. The degree of influence being dependent mainly on the amplitude of the push-pull loading and the prior torsion fatigue cycle ratio since the cyclic torsion loading remains constant. The selected push-pull load ranges were all above the material's fatigue limit.

All the specimens for the fully reversed torsion loading were subjected to the same stress amplitude of $\Delta\tau = 410\text{MPa}$ corresponding to 1.8×10^6 cycles to failure. For the initial torsion loading (Phase 1) the fatigue cyclic ratio n_1/N_{f1} was varied (0.22-0.73N_{f1}), followed by the push-pull load interruption (Phase 2). The push-pull fatigue cycle ratio was chosen to represent a very low damage interruption ($n_2 = 0.04N_{f2}$) with stress ranges of 600, 640, 760 and 820 MPa. The final torsion loading (Phase 3) continued with the same loading as Phase 1 until failure.

3.5.2 Definition of Failure

The definition of failure varies with the perceptions of different investigators for their particular work undertaken as outlined in supporting literature. For instance in strain controlled torsion tests, where there is a stress gradient, failure may be defined at the point in time when the specimen cannot sustain a significant load [123] i.e. load instability due to rapid development of cracking. Other investigators have used failure criterion such as crack length [124] [125], the percentage drop off in torque

amplitude [126] or the torsion load carrying capacity radically changed [127], and the complete fracture as for push-pull loading [49], which is probably the simplest of all the failure definitions.

Although the different failure criterion used cannot be considered definitive for any particular test, this may offer parameters that can be used for future comparative tests by other workers. However, the definition of failure is associated with the inability to sustain the applied load for a given condition and can obviously be interpreted in many different ways. For this work programme failure is defined below;

For push-pull and torsion constant amplitude tests the fatigue lifetime was taken at the instant of complete rupture of the specimen. This criterion was chosen since the comparative evaluation of crack growth to failure is more precise (necessary for crack growth modelling). It was also easier practically to determine failure this way from the control aspects of the machine because the test machine had no under-load control facilities.

For the multiphase tests failure was determined by a 10% reduction in the steady state torsion loading which reflected the development of a Stage II crack system. Whereas non-failure was taken to be an endurance limit equivalent to a number of fatigue cycles of $\Sigma n/N_f \geq 2.45$.

Chapter 4

Test Results

4.1 Fatigue Results

4.1.1 Push-Pull Cycling

To obtain the fatigue endurance curve for push-pull cycling 8 specimens were tested and the experimental results are presented in Table 4.1.

Table 4.1 Push-pull fatigue lifetime results

Specimen No	Specimen Diam. (d_{min})	± P kN	$\Delta\sigma$ MPa	$N_{f\,(p\text{-}p)}$ Cycles
T1	7.971	20.5	820	1.846×10^4
T2	7.956	18.9	760	3.877×10^4
T3	7.984	17.5	700	6.603×10^4
T4	7.973	17.0	680	1.462×10^5
T5	7.980	16.3	640	2.378×10^5
T6	7.974	15.5	620	5.197×10^5
T7	7.979	15.0	600	4.418×10^6
T8	7.982	14.5	580	$> 10^7$

As discussed in Chapter 3 the push-pull fatigue lifetime ($N_{f(p-p)}$) was taken at the instant of complete rupture of the specimen. The graph of the push-pull fatigue endurance data and the representative fatigue curve are shown in Fig. 4.1. The best-fit push-pull fatigue endurance curve determined by regression analysis could be described as follows,

$$\Delta\sigma \, (N_f)^{0.05} = 1256.4 \ \dots\dots\dots\dots\dots\dots\dots\dots\dots\dots\dots\dots\dots\dots\dots \ (4.1)$$
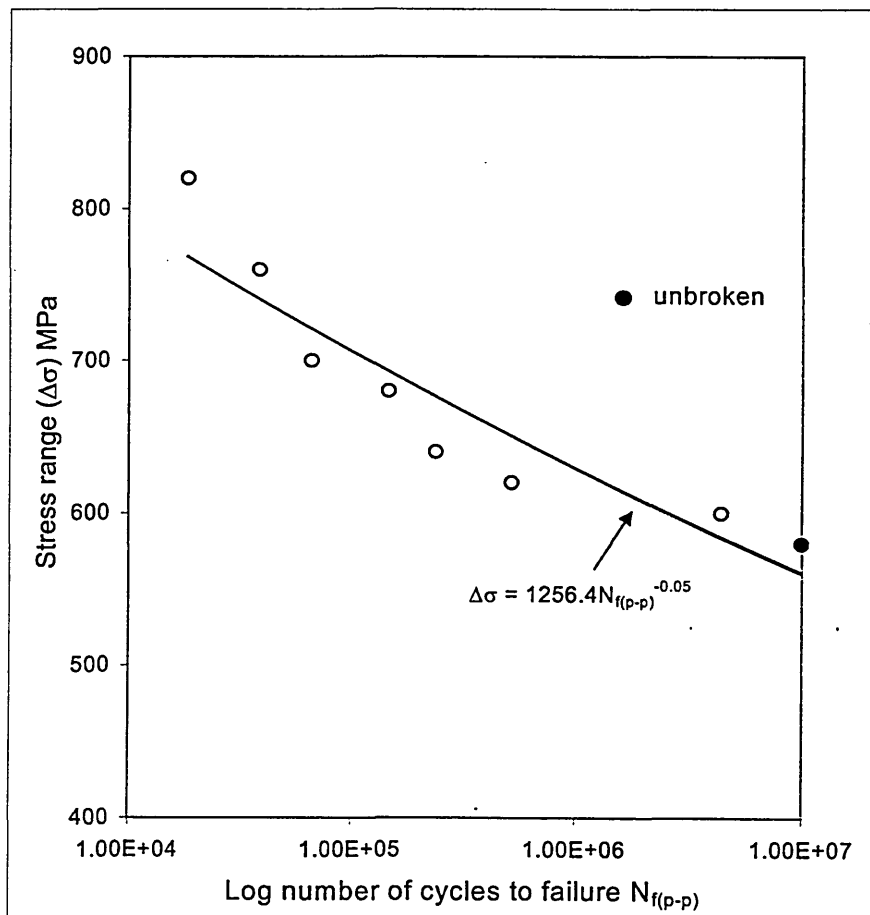
Fig. 4.1 Fatigue endurance curve for push-pull

To obtain the endurance curve for the fully reversed torsion loading, 8 specimens were tested and the experimental results are presented in Table 4.2.

Table 4.2 Torsion fatigue lifetime results

Specimen No	Specimen Diam. (d_{min})	ΔTorque Nm	$\Delta\tau$ MPa	$N_{f(t)}$ Cycles
T9	7.948	55.2	530	6.090×10^4
T10	7.914	51.6	495	1.583×10^4
T11	7.968	48.7	460	2.852×10^5
T12	7.970	45.7	435	5.231×10^5
T13	7.972	43.8	425	8.512×10^5
T14	7.951	41.5	415	1.297×10^6
T15	7.960	40.7	410	1.784×10^6
T16	7.975	37.8	385	$> 10^7$

As discussed in chapter 3 the torsion fatigue lifetime was taken at complete failure of the specimen. The graph of the torsion fatigue endurance data and the representative fatigue curve are shown in Fig. 4.2. The best-fit torsion fatigue curve determined by regression analysis could be described as follows,

$$\Delta\tau \, (N_f)^{0.0649} = 1052.7 \quad \dots\dots\dots\dots\dots\dots\dots\dots\dots\dots\dots\dots\dots \text{(4.2)}$$
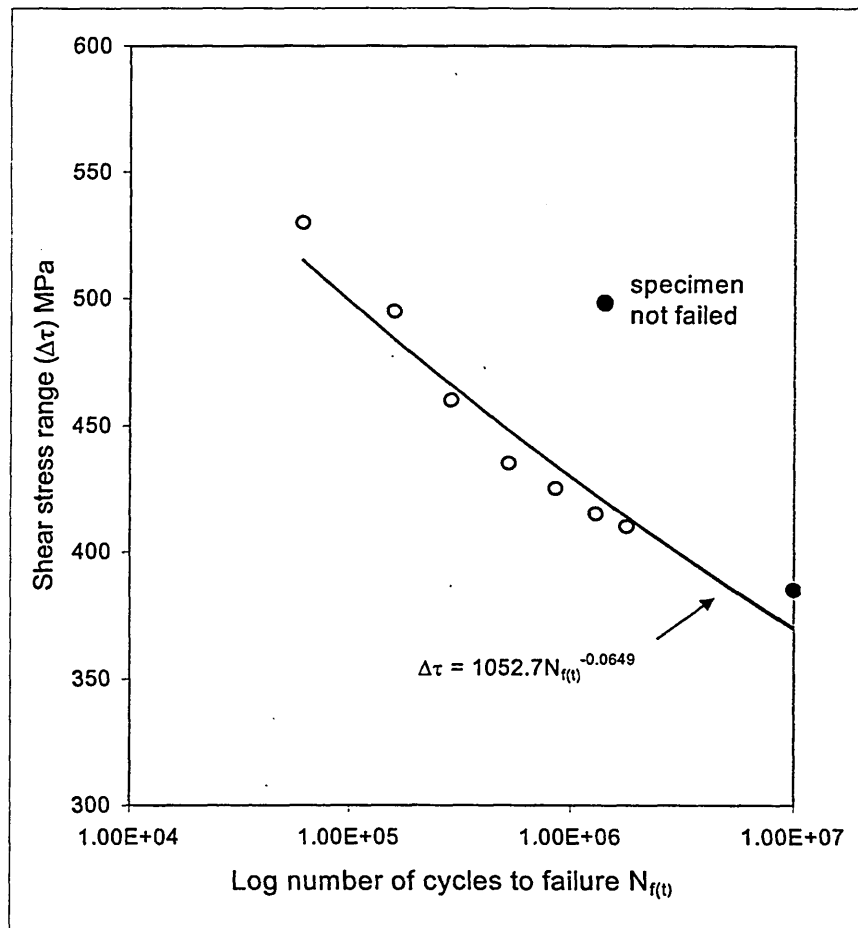
Fig. 4.2 Fatigue endurance curve for torsion

4.1.3 Multi-Phase Loading

Fatigue tests under multi-phase loading were conducted such that three loading phases were carried out sequentially i.e. Phase 1 - fully reversed torsion loading, followed by Phase 2 - push-pull cycling and finally Phase 3 - fully reversed torsion loading to failure. In all 17 multi-phase tests were conducted and the results are shown in Table 4.3.

Table 4.3 Multi-phase loading fatigue lifetime results

Specimen No	Torsion n_1 / N_{f1} (Phase 1)	Push-Pull $\Delta\sigma$ (MPa) (Phase 2)	Torsion n_3 / N_{f3} (Phase 3)	$\Sigma n/N_f$ Exp.
S1	0.22	600	1.35	1.61
S2	0.33	600	2.25	> 2.62
S3	0.53	600	2.13	> 2.70
S4	0.73	600	2.02	> 2.79
S5	0.22	640	2.24	> 2.50
S6	0.33	640	2.25	> 2.62
S7	0.53	640	2.01	> 2.69
S8	0.73	640	2.00	> 2.77
S9	0.22	760	0.43	0.69
S10	0.26	760	0.49	0.75
S11	0.33	760	0.50	0.88
S12	0.53	760	0.87	1.44
S13	0.73	760	0.96	1.73
S14	0.22	820	0.45	0.71
S15	0.33	820	0.36	0.67
S16	0.53	820	0.21	0.78
S17	0.73	820	0.55	1.32

Where in Table 4.3 the torsion stress range $\Delta\tau = 410$MPa, and for the Phase 2 push-pull loading the number of cycles are $\Delta\sigma$ 600MPa = 1.8×10^5 cycles, $\Delta\sigma$ 640MPa = 1.5×10^4 cycles, $\Delta\sigma$ 760MPa = 2.5×10^3 cycles and $\Delta\sigma$ 820MPa = 8.6×10^2 cycles.

4.2 Grain Size Measurements

The results of the grain size analysis are presented in Table 4.4.

Table 4.4 Results of ferrite grain size analysis

Field Count No	Mean Grain Size (μm)	Upper Grain Size (μm)
1	4.669	20.137
2	7.181	34.520
3	6.876	40.011
4	4.884	21.986
5	5.014	28.151
6	5.357	31.633
7	5.460	30.816
8	6.751	36.161
9	4.891	18.775
10	6.058	27.593
11	7.316	25.890
12	5.271	38.612
13	6.492	23.781
14	5.874	29.593
15	6.981	32.701
16	6.432	27.771
17	4.965	23.897
18	7.053	39.105
19	6.084	27.953
20	6.310	24.679

The ferrite grain size measurements used for the model parameter d were calculated for the material from the micrographs field areas as outlined in Chapter 3, to give a representative values for the upper and mean grain sizes. Both the upper and mean grain sizes were taken as the mean value of Σ(20 field counts) respectively. The upper and mean ferrite grains sizes calculated from the results of the grain size analysis presented in Table 4.4 and are given below,

$$d_{upper} = 583.777 \,/\, 20 = 29.1 \mu m \quad \text{................................} \quad (4.3)$$

$$d_{mean} = 119.936 \,/\, 20 = 5.996 \ \mu m \quad \text{................................} \quad (4.4)$$

and therefore the MSC growth model values approximated to the above such that,

$$d_1 \ \text{is taken as - } 29 \mu m \quad \text{................................} \quad (4.5)$$

$$d_2, d_3, \text{etc. are taken as - } 6 \mu m \quad \text{................................} \quad (4.6)$$

Chapter 5

Fatigue Crack Growth Modelling

5.1 Introduction

It is well established that the fatigue behaviour of metals can be described by three distinct regimes each having a different analytical approach to characterise crack propagation behaviour [128] i.e. MSC - MFM, PSC - EPFM and long cracks - LEFM as described in Chapter 2. Fatigue crack growth models developed to reflect these various stages of crack growth can prove difficult to realise for some cases where complex loading conditions are involved. This is particularly so for cases where short crack growth is the dominant fatigue process of the total fatigue lifetime. Especially where distinct phenomenon such as the deceleration and acceleration patterns of crack growth play significant roles, the effects of which have been attributed to the interaction of crack-tip plastic zone with microstructural barriers to plastic flow. Although Hong *et al* [78] suggested that the fatigue damage process involving short cracks in metallic materials might present collective evolution characteristics in that fatigue damage may result from a large number of dispersed short cracks, combined with grain size and the grain-boundary obstacle effects. Crack growth models have to take account of these effects if they are to be representative of the actual crack growth behaviour associated with a particular complex loading system. This is particularly so in HCF since short crack growth represents a significant proportion of the fatigue lifetime and any effective changes in stress-strain state can readily influence micro-crack growth mechanisms. Ibrahim [49] and Zhang [50] have shown

separately this to be the case for two-stage loading conditions where fatigue crack growth can be affected considerably depending on which stress-strain state is applied initially. Indicating that different loading conditions present formidable problems in modelling crack growth behaviour.

The experimental work carried out in this research programme featured multi-stage loading patterns that similarly influenced the underlying crack growth mechanisms, which had a pronounced effect on crack growth. Crack growth mechanism that produced distinct crack growth patterns, the consequence of which affected the fatigue lifetimes of the specimens considerably.

Crack growth models were developed to predict the fatigue behaviour of the medium carbon steel used in this research programme, for the push-pull and torsion constant amplitude tests, and the crack growth behaviour and fatigue lifetimes for the multi-phase loading

5.2 Crack Growth Models

The crack growth models developed for this work are based on short and long crack growth models proposed by Brown-Hobson [97]. The models describe both the Stage I shear crack development or short fatigue crack growth regime which is suggested to reflect MFM after Miller [33], and the Stage II tensile crack propagation or PSC and long crack growth regime corresponding to EPFM and LEFM analysis respectively.

The short fatigue crack equation may be expressed in the form,

$$\mathrm{d}a_s/\mathrm{dN} = A(\Delta\sigma)^m (d - a_s) \quad\text{...} (5.1)$$

where A and m are material constants, $\Delta\sigma$ represents the applied stress range, d refers to the distance to successive microstructural barriers and a_s is crack length for a short crack.

Thus equation (5.1) represents the crack growth process which experiences retardation and acceleration in crack growth, that is governed by the balance of local driving and the resistive forces associated with periodic microstructural barriers [37]. The fatigue crack will continue to grow if the applied stress level is sufficient to overcome the dominant microstructural barrier and so develop into a PSC as the start of the long crack regime. At this transitional point in crack growth the role of the microstructure diminishes. The PSC equation may be expressed in the form,

$$\mathrm{d}a_l/\mathrm{dN} = B(\Delta\sigma)^n a_p - D \quad\text{...} (5.2)$$

where B, D and n are material constants and a_p is the length of a PSC.

The parameter D in the original Brown-Hobson model, is determined by invoking a threshold condition i.e. $\mathrm{d}a_p/\mathrm{dN} = 0$ in equation (5.2) such that;

$$D = B(\Delta\sigma)^n a_{th} \quad\text{...} (5.3)$$

and

$$a_{th} = 2(\Delta K_{th})^2 / [\pi(\Delta\varepsilon)^2 Y^2 E^2] \quad\text{.................................} (5.4)$$

where ΔK_{th} is the threshold stress intensity factor range, E is Young's modulus and Y = $2/\pi$.

5.3 Fatigue Lifetime Models

For the purpose of this work computer programs were developed for torsion using torsion S-N fatigue data to predict push-pull fatigue data, based on the short and long crack equations (5.1) and (5.2). The crack growth models are purely stress state dependent for a given material and no account of load interaction on crack growth is considered whereby interrupted crack growth could occur. The models assume only uninterrupted crack growth for the loading cases. The predicted fatigue damage was derived by the summation of the MSC and PSC phases by integrating equations (5.1) and (5.2) of the form,

for MSC growth

$$\mathrm{d}a/\mathrm{d}N = C_m (d_i - a) \quad \text{.. (5.5)}$$

where C_m is stress state dependent rate such that;

for torsion

$$C_{m\,(t)} = A(\Delta\tau)^m \quad \text{.. (5.6)}$$

and for push-pull

$$C_{m\,(p\text{-}p)} = A(\Delta\sigma)^m \quad \text{... (5.7)}$$

99

$$N_{fs} = (1/ C_m) \ln [(d - a_o)/(d - a_t)] \quad\text{.................................} (5.8)$$

where A and m are material constants, d is the distance to microstructural barrier (μm), a_o is the surface finish (μm) and a_t represents the transition point to physically small crack (μm), determined from equations (5.7) and (5.10) at the threshold condition i.e. $da/dN = 0$.

For PSC growth :-

$$da/dN = C_p a - D \quad\text{...}(5.9)$$

where C_p is again stress state dependent such that;

for torsion

$$C_{p(t)} = B(\Delta\tau)^n \quad\text{...}(5.10)$$

and for push pull

$$C_{p(p-p)} = B(\Delta\sigma)^n \quad\text{...}(5.11)$$

$$N_{fp} = (1/C_p) \ln [(a_t - D/B(\Delta\sigma)^n) /(a_f - D/B(\Delta\sigma)^n)] \quad\text{..........}(5.12)$$

where B, D and n are material constants and a_f corresponds to failure crack length (μm).

The value for a_o here was taken to be (2 μm), the rounded-up equivalent of R_v which was determined from the measurements of the surface finish of polished untested specimens as outlined Chapter 3. For a_f this was taken to be half the minimum diameter of the specimen i.e. $d_{min}/2 = 4000$ μm. The total lifetime is the summation of the short and long crack fatigue lifetimes,

$$N_f = N_{fs} + N_{fp} \dots\dots\dots\dots\dots\dots\dots\dots\dots\dots\dots\dots\dots (5.13)$$

5.3.1 Determination of the Parameter d for the Model

In the short crack growth equation (5.1) the parameter d represents a crack length when the crack growth rate decreases to a minimum, corresponding to a position where the crack front meets a main microstructural barrier i.e. grain or phase boundary. Several workers have employed different methods to establish this parameter and Hobson [93] obtained d by applying a least-square fit to data points for crack growth rate (da/dN) versus the average crack lengths, approximated to where a marked retardation in crack growth was observed. The value of d was taken from the extrapolated least-square regression line at the point of intersection with the abscissa. Murtaza and Akid [98] using the same method reported some variations for d from the experimental analysis and suggested this was associated with the physical nature of the material, reflecting variations in grain size. Carbonell and Brown [96] used a different method to obtain d from empirical data by a best-fit third order polynomial passing through the origin. The point of inflexion of the polynomial was taken as the value of d that corresponded to minimum crack growth rate. Mohamed [129] used a more direct method and measured the value of d physically from plastic

101

replicas and applied this value individually to each crack. Although, for this method the precise measurement of d could prove difficult to establish if cracks continue to propagate into the next grain. As discussed in Chapter 2 Zhang [50] however, used a method, which avoided numerical calculation, or plastic replica observations by equating d from the statistical evaluation of measured grain sizes.

For the current work the value of d was equated to the ferrite grain size of the material, since the weaker ferrite grains are generally the sites for microcrack initiation and Stage I crack growth. The method used here is considered appropriate since short crack growth is strongly dependent on microstructure, particularly for lower stress levels. The quantitative analysis of the microstructure of untested material was carried out using a Buelher Omnimet Imaging analyser and was based on the mean linear intercept method to analyse the ferrite grain sizes. The analysis was performed on ferrite grains from a surface area of the specimen, which was carefully sectioned with the grain structure coincidental with the longitudinal axis of the specimen. Some grains however, proved difficult for the system to distinguish, even though the final polish using 'Silico-Colloidal' before etching achieved a highly polished surface finish. This was mainly where a few small ferrite grains had some minor dispersions of cementite, but, not characteristic of a pearlite region. Consequently some grains were ignored in the count by size limitation, but, the number was not considered to be significant in the statistical analysis of the field counts taken. The upper and mean grain sizes were calculated from the 20 field counts as outlined in Chapter 4. The grain sizes were based on ~ 657 grain measurements such that the upper grain size was calculated to be 29.1μm and the mean grain size calculated to be 5.996μm.

Therefore, d_I for the model is taken to be approximated to the mean of the upper bound grain sizes -such that $d_I = 29$ μm, which is considered to be representative of the crack initiation site, since it is has been observed that cracks generally initiate in 'large' ferrite grains [50]. The subsequent barrier lengths $d_1, d_2, etc.$ are taken as d_I plus the mean of the mean grain sizes which was calculated to be $= 6$μm. Therefore the parameters $d_I = 29$μm, $d_2 = 35$μm, $d_3 = 41$μm...etc.

5.3.2 Definition of Plastic Zone at Grain Boundaries

The model assumes a crack retardation threshold condition where (da/dN → 0) for crack advance in the first and subsequent grains to represent the characteristic of crack development as it approaches a grain boundary such that;

$$a_s = (d_i - r_{p(s)}) \quad\text{..} (5.14)$$

where $r_{p(s)}$ is taken to represent the extent of plastic slip zone ahead of the crack tip for MSC growth, that theoretically corresponds to a critical point where $r_{p(s)}$ is restricted by the microstructural boundary at the instant crack propagation continues into the next grain as shown in Fig. 5.1.

The above threshold position represented by equation (5.14) is similar in principle to the approach of Zhang [50] who proposed that;

$$a_s = (\alpha d_i) \quad\text{..} (5.15)$$

where α is dependent on the microstructure of the material and who used an arbitrary value for $\alpha = 0.95$. Therefore, α can be related to plastic deformation ahead of the crack tip as suggested in equation (5.14) such that;

$$\alpha = [1- (r_{p(s)}/d_i)] \quad \text{.. (5.16)}$$

The threshold condition for the crack to advance to the next grain is consistent with the theory of continuously distributed dislocations to represent the activated slip region ahead of the crack tip which has been postulated by several authors [131][91][132].
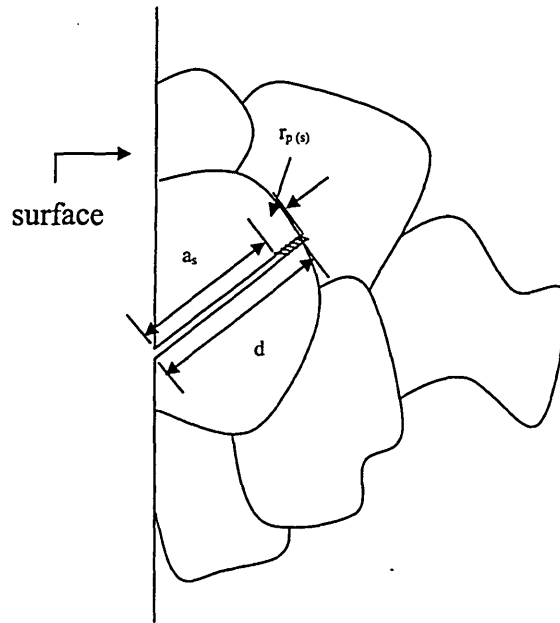

Fig. 5.1 Schematic showing plastic slip zone $r_{p(s)}$ for MSC

The model in effect corresponds to the onset of the fatigue process where the plastic slip deformation is caused by the movement of edge dislocations with Burger's vector along the x direction [38] i.e. parallel to the plane of the crack. Conditions that are synonymous with MSC growth where dislocation movement is blocked to an extent as the crack approaches a grain boundary. The growth rate at this point falls in response to the diminishing plasticity [50], or probably more accurately described as a result of the reduction in slip band formation since MSC growth is of the order of microstructural features [132]. However, if the crack is to proceed into the next grain and to overcome the blocking response of the microstructural barriers, Navarro and Rios [133] suggested that the shear stress (τ) ahead of the crack tip must be greater than the back stress (σ_b), where σ_b equates to the resistance to motion of dislocations by the ensuing barrier.

The crack retardation threshold can be expressed in terms of crack and crack-tip plastic zone relationship by the Bilby, Cottrell and Swinden model [90], for a freely slipping crack of the form;

$$a_s/d_i = \cos(\pi\tau / 2\sigma_b) \dots\dots\dots (5.17)$$

or,

$$a_s = [\cos(\pi\tau / 2\sigma_b)].\, d_i \dots\dots\dots (5.18)$$

or,

$$a_s = (\alpha d_i) \dots\dots\dots (5.19)$$

where $\alpha = [\cos(\pi\tau / 2\sigma_b)]$

and

$$r_{p(s)} = d_i \, [1\text{-cos} \, (\pi\tau \, / \, 2\sigma_b)] \; \dotfill \; (5.20)$$

Whilst recognising that crack advance is generally associated with some order of plastic deformation, $r_{p(s)}$ being on a microscopic scale is physically somewhat indeterminate. However, Navaro and Rios [133] suggested that crack growth will progress beyond a barrier when the stress concentration ahead of the plastic zone reaches a critical value related to the initiation of slip in the next grain. In this context αd_i could be approximated to the point for crack growth into the next grain and the value α in equation (5.25) which is obviously < 1 is therefore taken to be 0.95, same as that used in other similar work [50]. Therefore this representation of a critical crack length corresponding to a point within the grain that allows passage beyond the grain boundary can be considered consistent with the slip hypothesis put forward in the Navaro and Rios model.

5.4 Computer Modelling for Predicted Fatigue Lifetimes

5.4.1 Torsion and Push-Pull Loading

Computer model programs were developed to determine the predicted fatigue lifetimes for fully reversed torsion and push-pull cycling fatigue-loading conditions by utilising the Excel computer software package. These constant amplitude predictions were the first step for the later development of a computer program for multi-stage loading. The short and long crack growth equations (5.5) and (5.9) were

used to generate the S-N curves for torsion and push-pull to correlate calculated fatigue data to experimental S-N data by graphic interpolation.

The material constants A, B, D, m and n in the short and long crack growth equations (5.6) and (5.10) are dependent on the material's individualistic microstructural characteristics and are normally determined empirically. This is because even for similar materials the determination of the material constants in this way generally results in some variations, since they are derived from crack growth data. However, for this research work the material constants were determined from the experimental S-N fatigue data for the material. This method was considered to be of significance since S-N data is generally widely available for different materials. Yet, beyond its minimalist use for the representation of a materials fatigue endurance characteristics and comparative evaluation against other materials, the data becomes limited for further work. This approach however, presented some problems initially, because, since fatigue data represents both the MSC and PSC growth phases, the material constants are difficult to resolve mathematically. Therefore, another approach was developed to determine the material constants by utilising computer technology

Modern computer-based techniques such as mathematical modelling and finite element analysis (FEA), are increasingly used in engineering research activities to enable designs to be synthesised and analysed so that aspects of performance can be measured. Therefore, since material constants for short and long crack growth equations are difficult to determine from S-N data by other methodologies, it is considered appropriate in this case where extensive iteration procedures are necessary to use computer technology.

The computer programs for torsion and push-pull loading were developed initially to examine the validity of the short and long crack growth equations against the experimental results obtained. The fatigue limit in the computer model is equated to the experimental data for both stress states by invoking a fatigue threshold condition whereby the long crack fatigue lifetime equals zero;

$$N_{fp \; (\text{fatigue limit})} = 0 \quad .... \quad (5.21)$$

The predicted fatigue lifetime calculated by the model assumed an idealised crack growth pattern whereby at the start of fatigue cycling a crack propagates from a defect size on the surface of the specimen and continues to grow until a failure criterion is reached. This short crack growth behaviour is determined by the collective MSC and PSC growth phases and the degree of influence each has, is dependent on the stress amplitude, loading mode and the material parameters specific to that material. As discussed in detail in Chapter 2, MSC growth is known to be particularly affected by the material's microstructure and the effect is more significant at lower stress amplitudes.

Fig.5.2 shows diagrammatically the representation of short crack growth outlining the MSC and PSC growth phases, the surface crack length a, the transitional crack length (a_t), the surface finish a_o, the material parameter D and microstructural barrier lengths d_1, d_2, d_3 ....etc. The parameter D in the model is represented by the slope of da/dN versus the surface crack length a where the theoretical projected linear extension for PSC growth intercepts the da/dN axis (see Fig 5.2). Zhang [50] assumed the value at the point of intersection to be the 'short crack growth threshold'

since $da_{th}/dN = 0$. Therefore, the parameter D represents physically the Stage II crack growth rate threshold where a_{th} is dependent on the applied stress range.
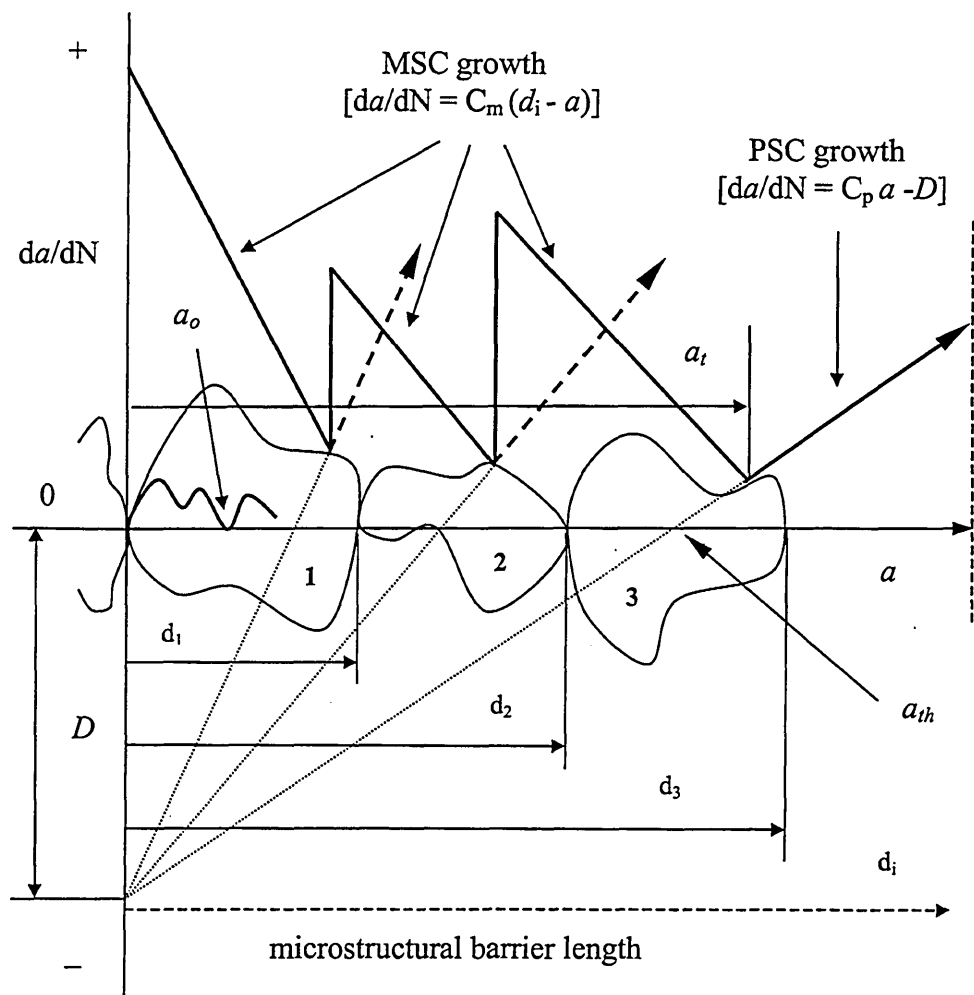

Fig 5.2 Diagram showing representation of short crack growth

It can be seen in Fig.5.2 that the Stage I to Stage II crack growth transition point is at grain 3. This is an arbitrary position taken to show the representation of crack growth through subsequent grains that can occur if the stress amplitude is high enough. If however, the stress amplitude is of a higher magnitude then the transition to Stage II crack growth can occur at a lesser grain number as shown by the dotted arrows in

Fig.5.2. Therefore for a given material and loading mode the transition point for Stage I to Stage II crack growth in the model is governed by the stress amplitude.

Computer programs were developed to correlate the experimental S-N data recorded for push-pull and torsion loading as the starting point for the later development of a computer program for multi-phase loading. The material constants were determined by theoretical analysis using the computer programs and applying iteration techniques, to the base values of known material constants obtained experimentally for a medium carbon steel [50]. This enables a best-fit analysis to be achieved for the material constants for the short and long crack growth equations. This is considered an acceptable method by the analysis of S-N data, since short and long crack growth equations are the collective representation of fatigue lifetime above the fatigue limit. The material constants obtained using the crack growth model equations (5.5) and (5.9) that gave good approximation to the torsion and push-pull S-N fatigue data are outlined below;

$$A = 1.800 \times 10^{-39}$$

$$B = 6.523 \times 10^{-27}$$

$$D = 3.74 \times 10^{-3}$$

$$m = 13.400$$

$$n = 8.129$$

The MSC and PSC growth equations were derived accordingly and are given as,

for MSC growth

$$da/dN = 1.800 \times 10^{-39} (\Delta\tau_{eq})^{13.400} (d\text{-}a) \dots\dots\dots\dots (5.22)$$

where $\Delta\tau_{eq} = \beta \, \Delta\tau_{max}$

and $\beta = 1.0$ .... for torsion

$\beta = 0.59$ .... for push-pull

and for PSC growth

$$da/dN = 6.523 \times 10^{-27} (\Delta\sigma_{eq})^{8.129} a - 3.74 \times 10^{-3} \dots\dots (5.23)$$

where $\Delta\sigma_{eq} = \phi \, \Delta\sigma_{max}$

and $\phi = 1.0$ .... for torsion

$\phi = 0.79$......... for push-pull

Note: plots using the above models are compared to the S-N results for torsion and push-pull and are shown subsequently in Figs 5.4 and 5.5 respectively.

5.4.2 Multi-Phase Loading

The crack growth model for multi-phase loading was developed by utilising the models developed for the torsion loading and push-pull to characterise the fatigue crack growth for any particular loading condition. The model accounted for crack

growth and the cumulative damage sustained during the three cyclic loading phases i.e. torsion (Phase 1), push-pull (Phase 2) and torsion (Phase 3) to failure. Such that crack growth for the torsion and push-pull load interruption could be predicted for the cycle ratios respectively and the subsequent predicted torsion fatigue lifetime evaluated.

The multi-phase crack growth model reflects the crack growth from the onset of fatigue cycling with no account for crack nucleation. Each of the loading phases thereby accounts for the damage sustained by a pseudo dominant crack that continues to propagate during each phase unless the predetermined failure crack length is attained. The model can derive the crack length under Phase 1 for any conditions i.e. stress amplitude and number of cycles applied. Whereon the crack growth sustained in Phase 1 determines the initial crack size for Phase 2 and whether Stage I or Stage II which is dependent on applied stress amplitude of Phase 2. The model predicts the final crack position of Phase 2 again depending on the stress amplitude and the number of cycles applied during this phase. The crack growth starting point for the final Phase 3 from phase 2 and the number of cycles to failure is then computed for Phase 3 for any given stress amplitude . The model determines the transitional stage from Stage I to Stage II crack growth during any of the phases and establishes the number of cycles in Phase 3 corresponding to the predetermined failure crack length i.e. fatigue failure.

The procedural steps adopted for the multi-phase loading are shown in the flow chart in Fig. 5.3 and the computer program (part) for multi-phase loading (torsion - push-pull - torsion → failure) is listed in Appendix 4.
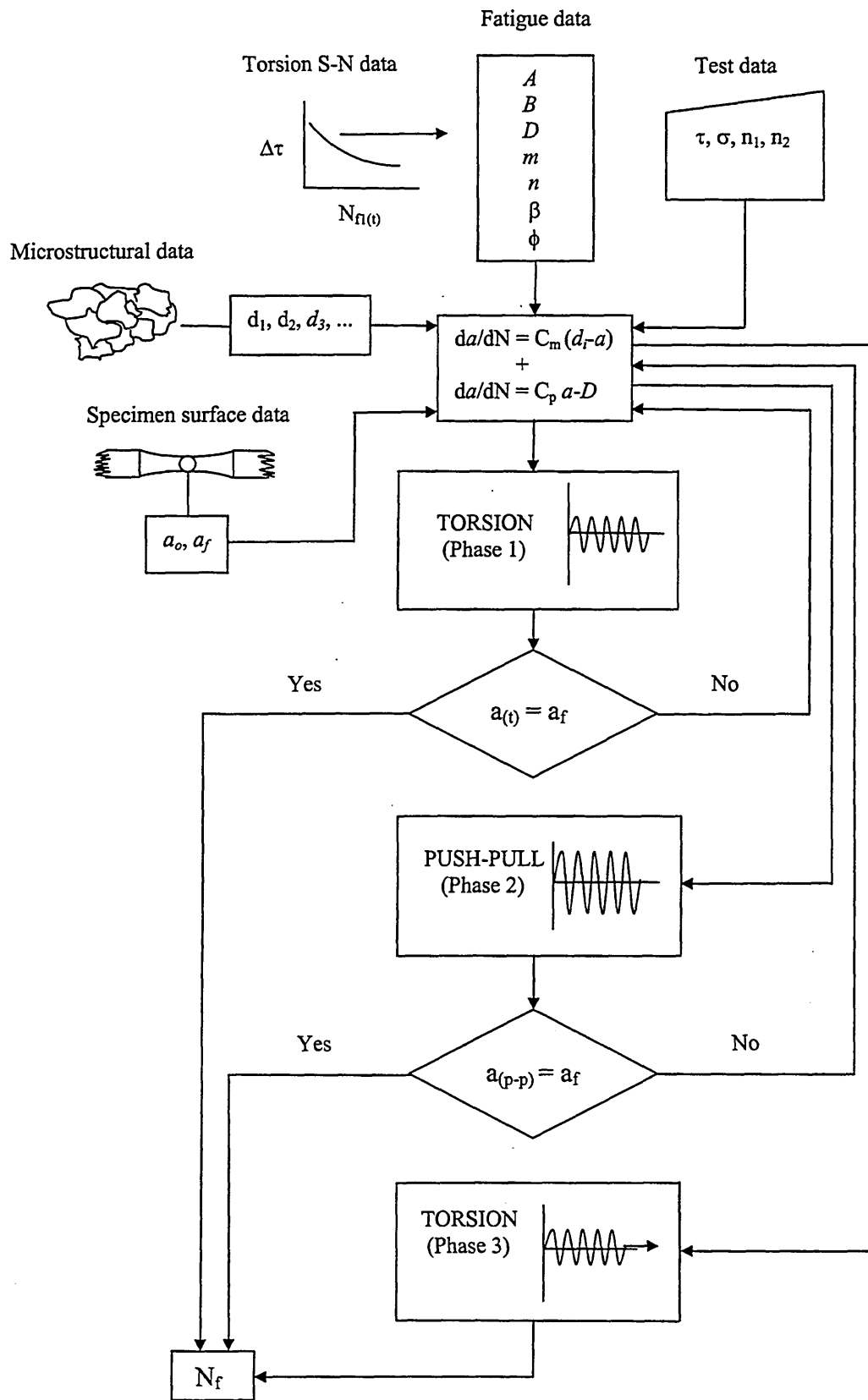
Fig. 5.3 Computer program flow chart for multi-phase loading

113

5.5 Predicted Fatigue Lifetimes

5.5.1 Fully Reversed Torsion Loading

The experimental results obtained for the cyclic torsion loading are compared with the model predicted lifetimes results and are presented in Table 5.1.

Table 5.1 Comparisons of experimental and predicted lifetimes for torsion loading

$\Delta\tau$ MPa	Model Lifetime ($N_{fs(t)}$)	Model Lifetime ($N_{fp(t)}$)	Total $N_{f(t)}$ $N_{fs(t)} + N_{fp(t)}$	Experimental Results
530	2.324×10^3	7.134×10^4	7.367×10^4	6.090×10^4
495	1.289×10^4	1.258×10^5	1.381×10^5	1.583×10^5
460	6.578×10^4	2.779×10^5	3.437×10^5	2.852×10^5
435	2.322×10^5	3.673×10^5	5.995×10^5	5.231×10^5
425	3.884×10^5	4.057×10^5	8.391×10^5	8.512×10^5
415	6.586×10^5	5.250×10^5	1.184×10^6	1.297×10^6
410	8.579×10^5	5.966×10^5	1.454×10^6	1.784×10^6
385	3.403×10^6	9.503×10^5	4.353×10^6	$> 10^7$

The torsion constant amplitude loading model predicted lifetime results are in good agreement with the experimental results as can be seen in Table 5.1. It further shows that the crack growth behaviour for this particular medium carbon steel subjected to torsion constant amplitude loading can be represented by the crack growth rate equation (5.5) for the MSC growth phase and (5.9) for the PSC growth phase.

The torsion experimental fatigue data and the model fatigue curve are shown in Fig. 5.4. The Excel spread sheets outlining the computed results for the model torsion loading tests are shown in Appendix 5.1
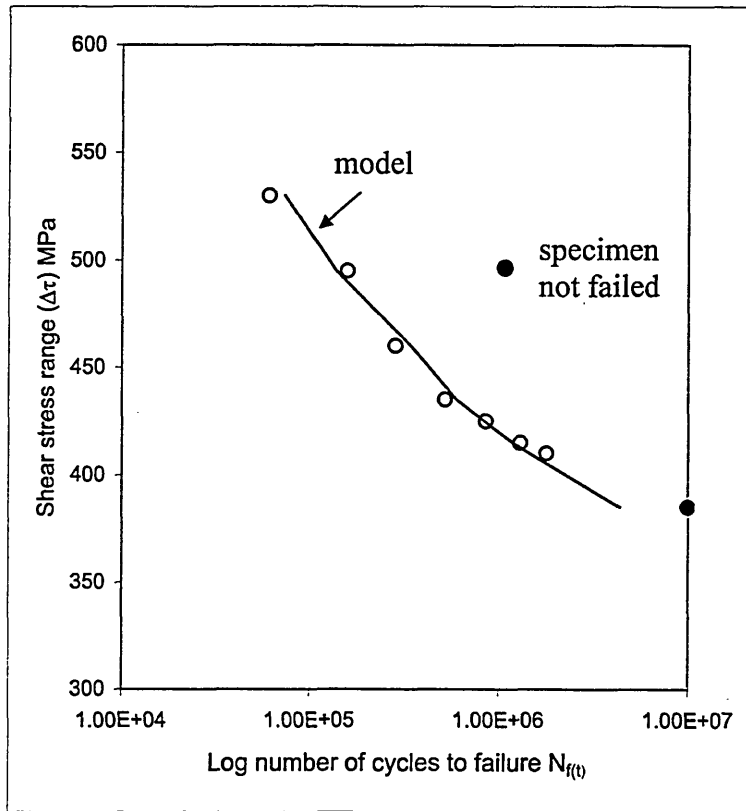

Fig. 5.4 Model fatigue curve (torsion)

5.5.2 Push-Pull Loading

The experimental results obtained for the cyclic push-pull loading are compared with the model predicted lifetimes results and are presented in Table 5.1.

It can be seen in Table 5.2 that the model predicted lifetime results are in good agreement with the experimental results. It further shows again as for the torsion case

that the crack growth behaviour for this particular medium carbon steel subjected to push-pull constant amplitude loading, can be represented by the crack growth rate equation (5.5) for the MSC growth phase and (5.9) for the PSC growth phase.

Table 5.2 Comparisons of experimental and predicted lifetimes for push-pull loading

$\Delta\sigma$ MPa	Model Lifetime ($N_{fs(p-p)}$)	Model Lifetime ($N_{fp(p-p)}$)	Total $N_{f(p-p)}$ $N_{fs(p-p)} + N_{fp(p-p)}$	Experimental Results
820	2.290×10^2	1.659×10^4	1.682×10^4	1.846×10^4
760	1.308×10^3	3.317×10^4	3.448×10^4	3.877×10^4
700	3.723×10^4	5.701×10^4	9.425×10^4	6.603×10^4
680	5.784×10^4	7.761×10^4	1.354×10^5	1.462×10^5
640	3.347×10^5	1.299×10^5	4.647×10^5	2.378×10^5
620	7.496×10^6	1.717×10^5	9.213×10^5	5.197×10^5
600	1.659×10^6	2.321×10^5	1.891×10^6	4.418×10^6
580	3.718×10^6	2.815×10^5	3.999×10^6	$> 10^7$

The pull-push experimental fatigue data and the model fatigue curve are shown in Fig. 5.5. The computed predictions for push-pull and torsion constant amplitude loading are outlined on the spreadsheet in Appendix 5.
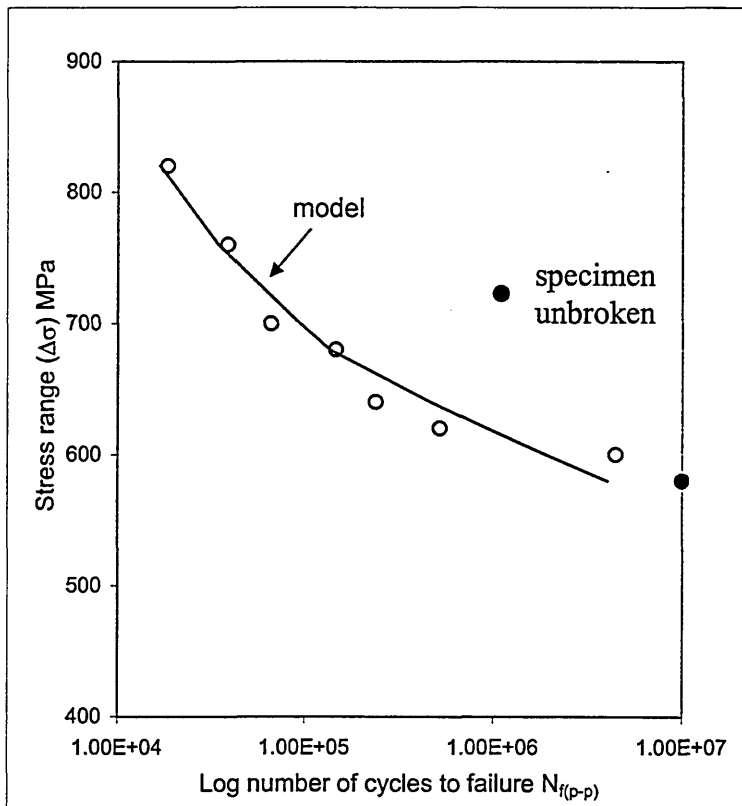
Fig. 5.5 Model fatigue curve (push-pull)

5.5.3 Multi-Phase Loading

The model fatigue lifetime predictions are compared with experimental results obtained for multi-phase loading as presented in Table 5.3. It can be seen clearly in Table 5.3 that the model predictions are not in agreement with the experimental fatigue lifetime results, where interrupted crack growth has occurred and the torsion fatigue lifetime has been enhanced considerably under the lower interrupted loads. The model however, does give conservative predictions for all cases, which is significant since fracture can be dangerous and is generally the foremost requirement in most practical cases. The computed predictions for multi-phase loading are outlined on the spreadsheets in Appendix 6 and 7.

Table 5.3 Predicted and experimental lifetimes for multi-phase loading

Test No	Torsion n_1 / N_{f1} (Phase 1)	Push-Pull $\Delta\sigma$ (MPa) (Phase 2)	Torsion n_3 / N_{f3} (Phase 3)	$\Sigma\, n/N_f$ Exp.	$\Sigma\, n/N_f$ Model
S1	0.22	600	1.35	1.61	0.386
S2	0.33	600	2.25	> 2.62	0.429
S3	0.53	. 600	2.13	> 2.70	0.581
S4	0.73	600	2.02	> 2.79	0.770
S5	0.22	640	2.24	> 2.50	0.469
S6	0.33	640	2.25	> 2.62	0.512
S7	0.53	640	2.01	> 2.69	0.664
S8	0.73	640	2.00	> 2.77	0.845
S9	0.22	760	0.43	0.69	0.678
S10	0.26	760	0.49	0.75	0.571
S11	0.33	760	0.50	0.88	0.568
S12	0.53	760	0.87	1.44	0.706
S13	0.73	760	0.96	1.73	0.884
S14	0.22	820	0.45	0.71	0.681
S15	0.33	820	0.36	0.67	0.570
S16	0.53	820	0.21	0.78	0.707
S17	0.73	820	. 0.55	1.32	0.886

Where in Table 5.3 the torsion stress range $\Delta\tau = 410$MPa, and for the Phase 2 push-pull loading the number of cycles are $\Delta\sigma$ 600MPa $= 1.8 \times 10^5$ cycles, $\Delta\sigma$ 640MPa $= 1.5 \times 10^4$ cycles, $\Delta\sigma$ 760MPa $= 2.5 \times 10^3$ cycles and $\Delta\sigma$ 820MPa $= 8.6 \times 10^2$ cycles.

Chapter 6

Discussion

6.1 Fatigue Damage Accumulation

6.1.1 Introduction

The accumulation of fatigue damage generally results in fatigue failure irrespective of whether the load cycles are uniform or of irregular manner. Although loading cycles of more irregular manner can result in a more complex accountability of fatigue damage. Therefore, for cases involving the lifetime predictions of complicated cyclic loading programs this has been referred to as the cumulative damage problem [134]. Notably since the Palmgren damage accumulation concept and the Miner linear damage rule (LDR) were introduced, more than fifty damage models have been proposed since the 1970s to the early 1990s [107]. However, none of these models are widely used, because their applications can become very complicated. In the attempt to evaluate the mechanisms and kinetics of crack initiation and propagation in variable loading cases even one as simple as that of a two-step test can be difficult and tedious to reconcile [134]. Whilst the endeavour is to seek more simplistic methodologies, these maybe difficult to realise and consequently the Palmgren-Miner LDR is still dominantly used despite its major shortcomings.

There are many factors affecting fatigue damage accumulation, such as loading sequence, residual stress, cyclic softening or hardening, fatigue life dispersivity and loading that is less than the fatigue limit [135]. The degree of influence these and other factors have on fatigue damage accumulation is sometimes difficult to predict, since the failure mechanisms involved can be very complex to evaluate. Realistically there are probably no simple resolvable solutions to the complexities surrounding the many fatigue processes, even though considerable real life working components are confronted with them.

Experimental analysis though can serve as an aid to seek improvement in the understanding of how these factors effect fatigue damage accumulation. Especially engineering components subjected to different loading modes and where the variability in the stress state is known to have a significantly affect on fatigue behaviour.

In cases where variable amplitude loading is involved it is customary to use LDR to quantify fatigue damage accumulation because of its simplicity. But, although the LDR is widely used in engineering design applications the damage calculated by this method does not actually reflect the actual fatigue damage which is mainly attributed to the formation and growth of fatigue cracks. Furthermore the LDR has been proposed predominantly for single mode loading situations such as uniaxial or torsion, and will not work satisfactorily for situations where the loading mode is changed periodically or in cases that involve sequential loading [49,50].

The main questions that arose from this work and discussed in detail in this chapter are,

- Could the LDR quantify fatigue damage accumulation if a push-pull load interruption that represented only 4% damage according to the LDR was introduced at different stages in the torsion fatigue lifetime of a specimen?

- What are the effects of the interaction of short fatigue cracks on multi-phase loading?

- How do changes in values of the parameters in the short and long crack growth equations affect fatigue lifetime predictions?

- Could the short and long crack growth models used for this work satisfactorily predict the crack growth behaviour under constant amplitude and non-proportional loading?

- What were the effects on crack growth behaviour as a result of the multi-phase loading?

- Are there any distinguishable features of crack growth behaviour from the micrograph observations of surface cracking systems and fractography analysis?

6.1.2 Multi-Phase Loading Fatigue Analysis

For recollection purposes the experimental procedure outlined in Chapter 3 is summarised as follows. The multi-phase loading tests were carried out to examine the effects that a non-proportional push-pull load interruption had on the torsion fatigue lifetimes of solid hourglass specimens manufactured from 0.42% carbon steel. The torsion stress range of $\Delta\tau$ = 410MPa remained constant for all the tests, whereas different interrupted push-pull stress ranges of 600, 640, 760 and 820 MPa were used. The push-pull cycles of $0.04n/N_{fp-p}$ were applied after prior torsion cycle ratios of 0.22, 0.26, 0.33, 0.53 and $0.73n/N_{ft}$.

The work programme demonstrated how the torsion fatigue life could be changed significantly for different torsion cycle ratios together with the introduction of the push-pull load interruption. This outlined how a the push-pull load interruption which represented only 4% damage according to the LDR significantly affected the crack growth behaviour and the torsion fatigue life of the specimen. In the case where the push-pull load interruption amplitude was less than ≈ 1.3 σ_{cy} (cyclic yield stress) then the experimental tests indicated that the torsion fatigue life could be expected to increase. However, if the push-pull load interruption amplitude was greater than ≈ 1.5 σ_{cy} then the torsion fatigue life could be dramatically reduced. Indicating that the degree of microscopic deformation at or near the crack tip as a consequence of push-pull load can play a significant role in affecting existing crack growth. In so much that at the higher stresses Stage I cracks start to develop, but at the lower stresses slip band formation is limited such that growth dependency is

considered to be a function not only of the magnitude of push-pull stress amplitude, but also its cycle ratio (n/N_{fp-p}).

It can be seen clearly from the Fig. 6.1, that Miner's linear damage rule cannot account for the cumulative fatigue damage ($\Sigma n/N_f$) for the push-pull interrupted torsion fatigue loading sequences used in the current test programme. The marginal push-pull load interruption of 4% should have been accounted for by the LDR, if the LDR is correct. However, the linear damage summation only came close to unity (≈ 0.88 in test S11) with the remaining number of tests either significantly above or below unity as shown by the test results in Table 4.3.
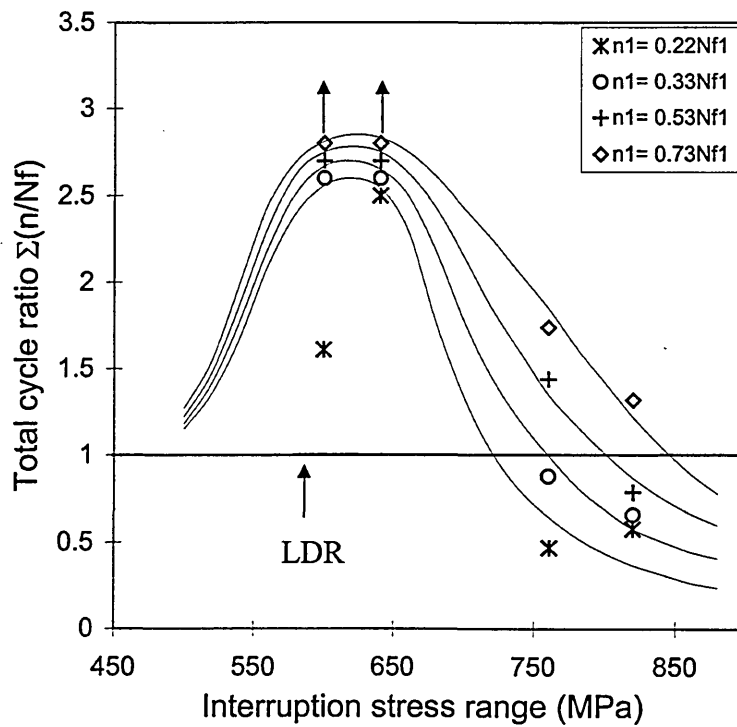

Fig.6.1 The total cycle ratio versus interrupted stress amplitude

The trend lines (solid lines) in Fig. 6.1 are included to indicate the predicted total cycle ratio → to unity as the push-pull load interruption amplitude falls below σ_{cy} ($\Delta\sigma$ = 580 MPa), since below this threshold it's effect on the torsion fatigue lifetime is considered to → 0.

As shown by the test results, the torsion fatigue life was found to change significantly due to the application of push-pull load interruption, which was considered to cause only a minor damage with respect to the LDR. The torsion fatigue life was enhanced considerably when the push-pull interruption was applied at a later stage of the torsion loading whilst the effect was less prominent when the interruption was applied at an early stage of torsion loading. At higher interruption stress amplitudes the torsion fatigue lifetime was reduced considerably and the damage summation was well below unity predicted by the LDR. The inability to predict damage accumulation by the LDR can be attributed to the complexity in the crack growth associated with the application of push-pull interruption. A similar behaviour has reportedly [48] been observed in non-proportional low cycle fatigue tests.

The introduction of the push-pull load interruption although minor in relative terms with respect to the number of applied fatigue cycles, demonstrated that it could have a marked effect on the torsion fatigue life of a component. Such that the application of a number of fatigue cycles of the different stress state need not be that significant to bring about a conservative or non-conservative effect on the torsion fatigue life with respect to the LDR.

6.2 Fatigue Lifetimes using Crack Growth Model

6.2.1 Fatigue Lifetime - Constant Amplitude Loading

The crack growth model was developed using torsion constant amplitude loading S-N fatigue data. The crack growth model was then used to predict the push-pull fatigue lifetimes for constant amplitude loading using an equivalent stress criterion i.e. $\Delta\tau_{eq} = \beta \Delta\sigma_{max}$ for MSC growth and $\Delta\sigma_{eq} = \phi \Delta\sigma_{max}$ for PSC growth as discussed in Chapter 5 (see pages 110 and 111). The crack growth model was found to be capable of predicting the fatigue lifetime for both stress states as shown by the results in Table 5.1 and 5.2 and Figs. 5.4 and 5.5 for each loading mode respectively.

Since the equivalent stress criterion used for the model predictions were derived by correlation to the material's S-N fatigue data, the push-pull experimental results are compared to the push-pull predicted fatigue lifetimes using the equivalent maximum shear stress theory of Tresca and the maximum shear strain energy theory of Von-Mises.

Therefore since the Tresca criterion based on the maximum shear stress gives,

$$\Delta\tau = 0.5 \Delta\sigma_{eq} \quad\text{...} (6.1)$$

and for the Von-Mises criterion based on the maximum shear strain energy gives,

$$\Delta\tau = 0.5 \Delta\sigma_{eq} \quad\text{...} (6.2)$$

where the equivalent stress range ($\Delta\sigma_{eq}$) is equal to $\Delta\sigma_{max}$ in push-pull loading.

Hence the cumulative fatigue lifetime calculated for Tresca for MSC and PSC growth is (MSC_{Tresca} + PSC_{Tresca}), and for Von-Mises ($\text{MSC}_{Von-Mises}$ + $\text{PSC}_{Von-Mises}$), therefore the Tresca and Von-Mises criterion stress coefficients β and ϕ used in equations (5.22) and (5.23) are taken as;

for MSC growth

$$\beta_{Tresca} = 0.50 \dots\dots\dots\dots\dots\dots\dots\dots\dots\dots\dots\dots \text{(6.3)}$$

$$\beta_{Von-Mises} = 0.58 \dots\dots\dots\dots\dots\dots\dots\dots\dots\dots\dots \text{(6.4)}$$

and PSC growth

$$\phi_{Tresca} = 0.50 \dots\dots\dots\dots\dots\dots\dots\dots\dots\dots\dots\dots \text{(6.5)}$$

$$\phi_{Von-Mises} = 0.58 \dots\dots\dots\dots\dots\dots\dots\dots\dots\dots\dots \text{(6.6)}$$

The push-pull experimental results and predicted fatigue lifetimes for the (MSC_{Tresca} + PSC_{Tresca}) and ($\text{MSC}_{Von-Mises}$ + $\text{PSC}_{Von-Mises}$) criteria are given in Table 6.1.

It can be seen from the fatigue lifetime values listed in Table 6.1 that the $\text{MSC}_{Von-Mises}$ + $\text{PSC}_{Von-Mises}$ and MSC_{Tresca} + PSC_{Tresca} predictions are considerably longer than the experimental results, with the MSC_{Tresca} + PSC_{Tresca} predictions being the more conservative.

Table 6.1 Push-Pull experimental results and predicted fatigue lifetimes for the

$MSC_{Von-Mises} + PSC_{Von-Mises}$ and $MSC_{Tresca} + PSC_{Tresca}$ criteria

Stress Amp. $\Delta\sigma$ (MPa)	Experimental $N_{f(p-p)}$	$MSC_{Von-Mises} + PSC_{Von-Mises}$ $N_{f(p-p)\,Von-Mises}$	$MSC_{Tresca} + PSC_{Tresca}$ $N_{f(p-p)\,Tresca}$
820	1.846×10^4	2.224×10^3	1.454×10^6
760	3.877×10^4	4.337×10^5	5.628×10^6
700	6.603×10^4	1.367×10^6	2.912×10^7
680	1.462×10^5	2.241×10^6	5.134×10^7
640	2.378×10^5	6.743×10^6	1.908×10^8
620	5.197×10^5	1.285×10^7	3.762×10^8
600	4.418×10^6	2.447×10^7	7.525×10^8
580	$> 10^7$	4.947×10^7	1.563×10^9

The predictions of the current work are similar to the findings reported by Zhang [50], who for a 0.45% carbon steel also found that neither the Tresca nor the Von-Mises criterion could give good push-pull fatigue lifetime predictions for a change in stresss state. This suggest that the short crack growth models used in this form are not capable of predicting the fatigue behaviour of a medium carbon steel for push-pull loading

The above predictions based on the Tresca and Von-Mises criteria for both MSC and PSC growth are clearly unrepresentative of the cumulative Stage I and Stage II crack

growth for the 0.42% carbon steel. However, since Stage II crack growth is largely dependent on the maximum principal stress normal to the crack direction, fatigue lifetime predictions based on the principal stress for PSC growth are considered. Such that Tresca and Von-Mises criteria are used for MSC growth and the Maximum Principal Stress (σ_1) for PSC growth i.e. ($MSC_{Tresca} + PSC_{\sigma1}$), and ($MSC_{Von-Mises} + PSC_{\sigma1}$).

Therefore since

$$\sigma_1 = \sigma_{max} \dotfill (6.7)$$

hence the coefficient and ϕ used in the PSC growth equations (5.23) is taken as,

$$\phi_{Max.\ Prin.\ Stress} = 1.00 \dotfill (6.8)$$

Therefore the push-pull experimental results and the predicted fatigue lifetimes for the $MSC_{Von-Mises} + PSC_{\sigma1}$ and $MSC_{Tresca} + PSC_{\sigma1}$ criteria are given in Table 6.2.

It can be seen from the values in Table 6.2 that the predicted lifetimes for the $MSC_{Von-Mises} + PSC_{\sigma1}$ and $MSC_{Tresca} + PSC_{\sigma1}$ criteria are much less than the experimental results, the $MSC_{Von-Mises} + PSC_{\sigma1}$ predictions are the more non-conservative.

Table 6.2 Push-Pull experimental results and predicted fatigue lifetimes for the

$MSC_{Von\text{-}Mises} + PSC_{\sigma 1}$ and $MSC_{Tresca} + PSC_{\sigma 1}$ criteria

Stress Amp. $\Delta\sigma$ (MPa)	Experimental $N_{f(p\text{-}p)}$	$MSC_{Von\text{-}Mises} + PSC_{\sigma 1}$ $N_{f(p\text{-}p)\,Von\text{-}Mises\,-\,\sigma 1}$	$MSC_{Tresca} + PSC_{\sigma 1}$ $N_{f(p\text{-}p)Tresca\,-\,\sigma 1}$
820	1.846×10^4	2.680×10^3	2.680×10^3
760	3.877×10^4	5.193×10^3	6.335×10^3
700	6.603×10^4	1.253×10^4	1.806×10^4
680	1.462×10^5	1.390×10^4	2.437×10^4
640	2.378×10^5	2.940×10^4	7.178×10^4
620	5.197×10^5	4.198×10^4	1.333×10^5
600	4.418×10^6	7.295×10^4	2.815×10^5
580	$> 10^7$	1.353×10^5	6.614×10^5

It can therefore be concluded that neither the $MSC_{Von\text{-}Mises} + PSC_{Von\text{-}Mises}$ and $MSC_{Tresca} + PSC_{Tresca}$ nor the $MSC_{Von\text{-}Mises} + PSC_{\sigma 1}$ and $MSC_{Tresca} + PSC_{\sigma 1}$ criteria can adequately predict the fatigue lifetime for the change in stress state.

Fig. 6.2 shows more clearly the relationship of the $MSC_{Tresca} + PSC_{\sigma 1}$ criteria and the $MSC_{Tresca} + PSC_{Tresca}$ criteria to the experimental data, where the former criteria underestimates and latter over-estimates the experimental push-pull fatigue data.
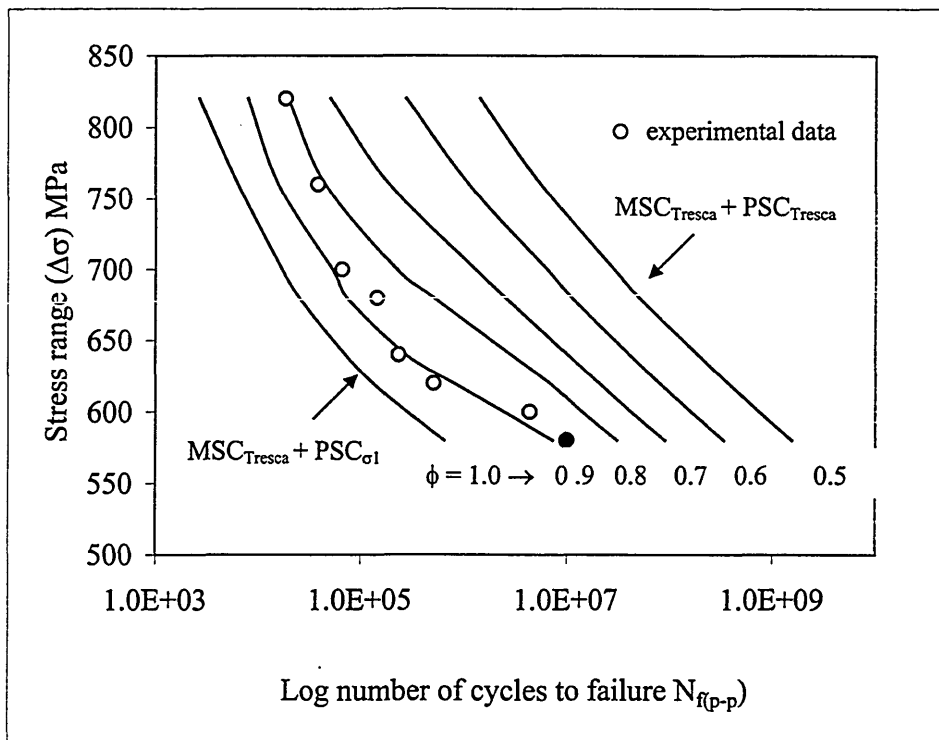
Fig. 6.2 Predicted fatigue endurance curves for MSC_{Tresca} and

PSC for different values of ϕ

Fig. 6.2 also shows the effect of decreasing stress coefficients of $\phi = 1.0,\ 0.9,\ 0.8,$

0.7, 0.6 and 0.5 as illustrated by the series of curves and indicates that the principal

stress is the more realistic criterion for the model PSC growth. This is probably not

unexpected since PSC growth (Stage II crack growth) is dependent largely on the

maximum principal stress operating in the specimen or in the region of the crack tip.

The relationship for $MSC_{Von\text{-}Mises}$ and PSC for different values of ϕ to the

experimental data is also clearly demonstrated by the curves for decreasing values of

ϕ ($\phi = 1.0,\ 0.9,\ 0.8,\ 0.7$ and 0.58) are shown in Fig. 6.3. Where in Fig 6.3 the

predicted fatigue endurance curve for $MSC_{Von\text{-}Mises}$ and for PSC where $\phi = 0.80$

approximates well to the experimental data. The criteria that approximates well to the

push-pull fatigue data in Fig. 6.3, is very close to the best-fit values of the Model,

since $\beta_{model} = 0.59$ and $\phi_{model} = 0.79$.
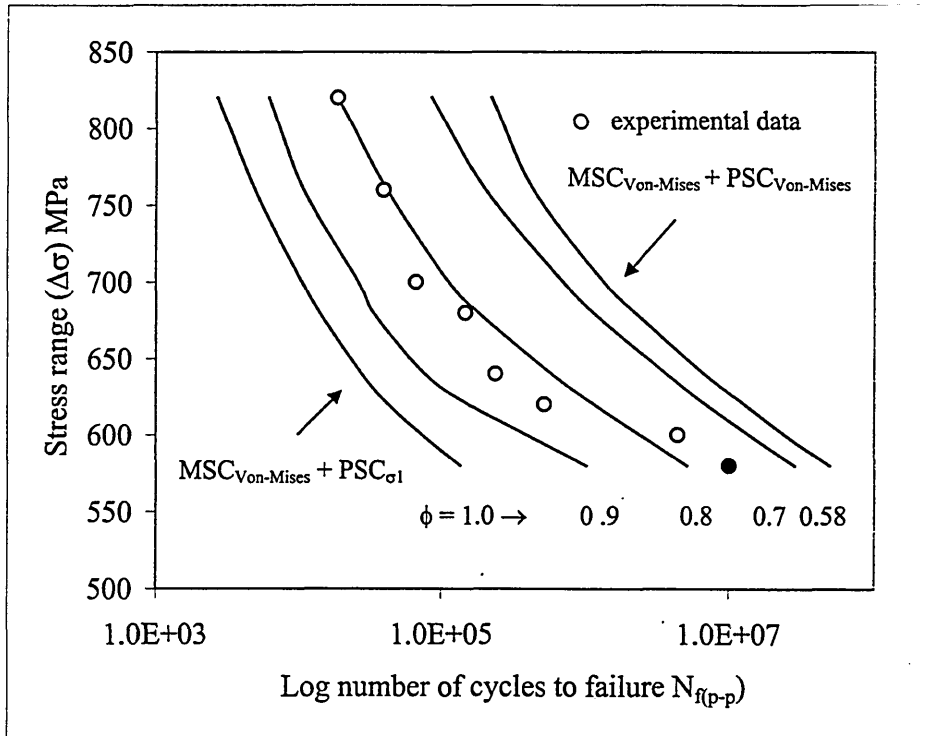
Fig. 6.3 Predicted fatigue endurance curves for $MSC_{Von-Mises}$ and for

PSC for different values of ϕ

From Figs. 6.2 and 6.3 it could be argued that to obtain a suitable fatigue criterion to

model the different stress states, it has to take account of the different crack growth

behaviours. Therefore, it could be reasoned that the orientation of cracks plays a

significant role in the determination of fatigue lifetimes for the different stress states.

Since crack initiation and subsequent propagation are in different directions and on

different planes for torsion and push pull loading as shown in Fig. 6.4. However, to

relate crack growth behaviour to a change in stress state, can be difficult to model

considering planes of crack advance alone. Different material constants have been used in short crack growth equations to reconcile the differences in crack growth behaviour, but the appropriateness of this approach seems questionable, since crack directionality should have no effect in an isotropic material.

Notably here, to unify the torsion and push-pull fatigue data, the model predictions were obtained by changing the stress coefficient (ϕ) for PSC, which gave acceptable predictions. Whereas, changing the stress coefficient (β) for MSC were found to give less satisfactory predictions, where the change in the curves were not as expected in comparison to the S-N curve.

A further point is that the propagation of fatigue microcracks in push-pull may also be influenced by the involvement of Mode I and II. The mixed mode condition may assist in the progressive development of Stage I crack growth and the earlier transition to Stage II crack growth, because a normal stress (σ_n) exists on the operative slip planes in push-pull loading (see Fig 6.4), whereas there is none in pure torsion loading. Since there is no tensile stress on the crack plane, there is a possibility of crack interlocking in torsion. The mechanical interlocking between the crack faces produces high frictional forces and as a consequence the stresses and strains at the crack tip are reduced and are purported to result in a lower crack growth rate. But, in tension loading the stresses perpendicular to the shear crack opens the crack surfaces and reduces or eliminates the frictional effect. Therefore, the stresses and strains at the crack tip will be higher and result in increased crack growth rates [136].
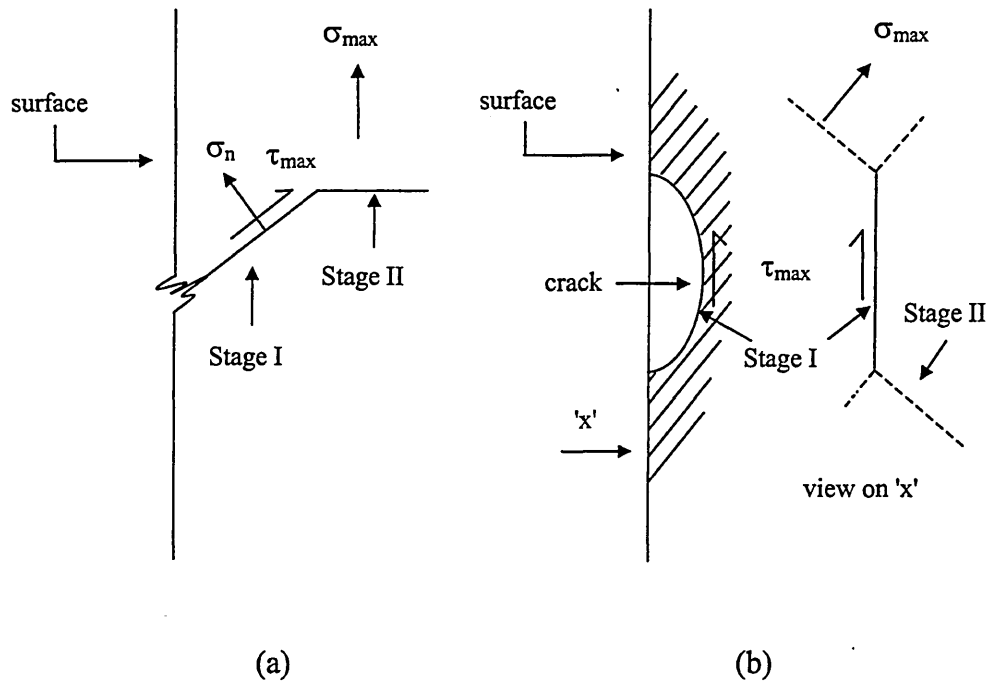
Fig. 6.4 Crack initiation and growth shown schematically for .

(a) push-pull loading and (b) torsion loading

6.2.2 Fatigue Lifetime - Multi-Phase Loading

The multi-phase crack growth model was capable of predicting the fatigue life in cases which where dominated by uninterrupted crack growth as shown by the results in Table 5.3. In this case where the crack growth rate increased, it could be argued that the less densely populated short Stage I cracks created by the initial torsion loading combined with the effects of the higher push-pull load interruption resulted in an earlier transition to a Stage II crack.

However, the model was not able to predict the fatigue life where the push-pull load interruption affected crack growth behaviour to such an extent that the crack growth rate was significantly retarded. The retardation in crack growth rate could be due to many contributory factors such as crack growth interaction, localised residual stresses, secondary crack initiation, the effects of crack blunting and cyclic strain hardening. One if not more of these factors may affect the behaviour of short fatigue cracks, since it is very difficult to isolate any individual contribution that could be influential, or not, in crack growth retardation. Especially for the work here, since the damage of the push-pull interruptions were relatively small and therefore the retardation effect on existing or new cracks can be difficult to establish with the absence of any distinguishable microstructural features. Since as discussed later, the observations of micrographs revealed a preponderance of surface extrusions generally aligned in a direction parallel to the specimen axis, but with only torsion Stage I cracking systems present.

The model gave conservative predictions for all the multi-phase loading conditions used in the testing programme as shown in Fig.6.5. The predictions were comparable with the experimental results for the tests with the higher push-pull interruption stress amplitudes, in particular where the prior torsion cycle ratio was small. However, the model significantly underestimated the fatigue damage for the lower interrupted loading, because the model does not account for interrupted crack growth i.e. the effect the crack-load interaction has to cause crack growth retardation. Nevertheless it should be emphasised that in fact the model was capable of predicting the fatigue life for the multi-phase loading that caused an acceleration of fatigue damage, which is important in view of safety.
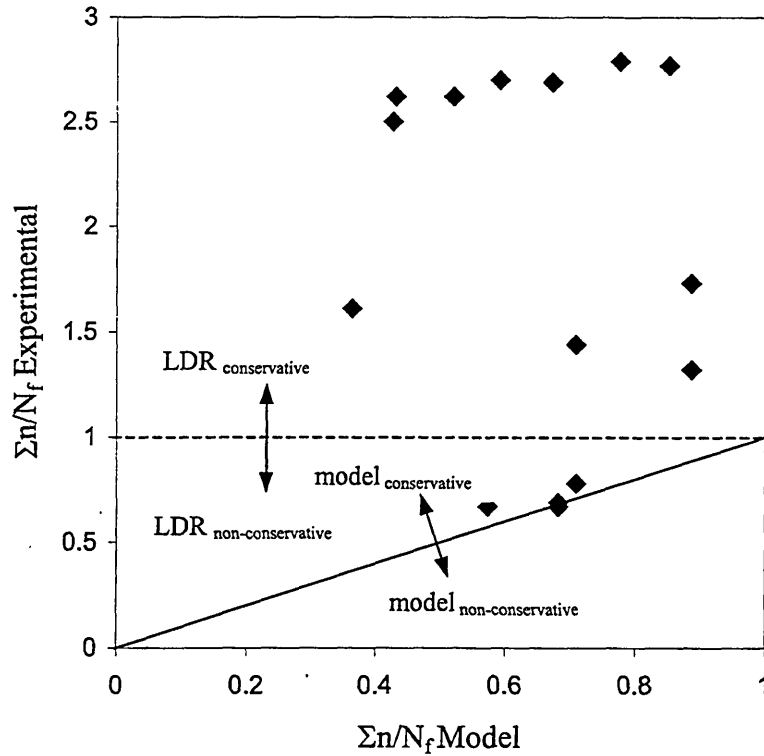
Fig. 6.5 Experimental results compared with model predictions

The mean of total damage summation of all the loading phases (n/Nf) tends to increase as the cycle ratio for Phase 1 torsion loading increased as shown by the solid lines in Fig. 6.6. This is evident for both the experimental and model predictions. The increase in gradient of the trend line is somewhat less for the model predictions than the experimental results, although for the experimental tests this might have been different if a pre-determined endurance limit Σ n/Nf $\geq$ 2.45 had not been invoked.

135
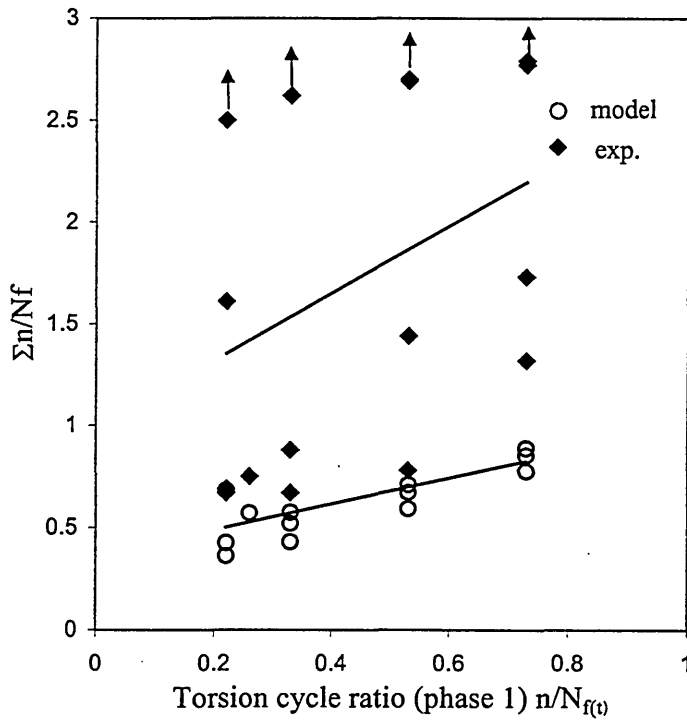
Fig. 6.6 Experimental and model trend predictions

Considering the trend of the model predictions statistically, the damage summation is not so significant since it has a standard deviation of only 0.158 $\Sigma n/N_f$ considering all Phase 1-torsion loading cycle ratio ($n/N_{f(t)}$) values. The statistical results do however decrease as the $n/N_{f(t)}$ increases, but not with any significance. In so much that for all the push-pull load interruptions applied after a cycle ratio of $0.22n/N_{f(t)}$ the standard deviation calculated is $0.168\Sigma n/N_f$, whereas after a cycle ratio of $0.73n/N_{f(t)}$ the standard deviation was only 0.052 $\Sigma n/N_f$. Thus indicating that the fatigue lifetime predictions are very close for all $n/N_{f(t)}$ values and push-pull load stress amplitude. But, this is unrepresentative of the experimental results, since the model does not account for interrupted crack growth due to the crack-load interaction as discussed earlier.

This is evident by the closeness of the standard deviations for statistical evaluations for all the push-pull stress amplitudes, since for all cases the model predicts transition to Stage II crack growth after Phase 1 torsion loading. This is because the computed crack lengths after Phase 1 torsion loading, are of a size that meet the condition set by the model for immediate transition to Stage II crack growth at the onset of the push-pull cycling. Or more precisely the computed crack length is $\approx 141 \mu m$ after the lowest Phase 1 torsion cycle ratio ($0.22 n/N_{f(t)}$), which is longer than the longest computed transitional crack length ($a_t \approx 106 \mu m$), for the push-pull load interruption phase.

The comparisons of the computed transitional crack length (a_t) for all the push-pull stress amplitudes to the computed torsion crack length (a) after the prior torsion loading are given in Table 6.3.

Table 6.3 Computed crack lengths - a_t (push-pull) and a (torsion - Phase1)

Push-Pull		Torsion ($\Delta\tau = 410$ MPa)	
$\Delta\sigma$	transitional crack length a_t (μm)	crack length a (μm)	cycle ratio $n/N_{f(t)}$
600	105.62	141.14	0.22
640	63.45	199.17	0.33
760	16.51	304.70	0.53
820	10.40	373.53	0.73

For comparative purposes the experimental Stage I crack lengths of the dominant cracking systems for multi-phase loading are presented in Table 6.4. For information the Stage I cracks were measured using a travelling microscope and the crack lengths were approximated to the nearest one tenth of a mm.

It is worth noting here that there are slight increases in Stage I crack lengths for increasing prior torsion cycle ratios, but these are not unexpected. Since, increased torsion cycling should promote the development of longer Stage I cracks by the coalescence of Stage I microcracks. The exception to this (specimen S10) could be explained by the local differences in microstructure (ferrite and pearlite) for this 0.42% carbon steel. Since for this non-uniform material the transitional crack length from Stage I to Stage II is somewhat random as discussed previously in Chapter 2.

Table 6.4 Stage I crack lengths for failed specimens under multi-phase loading

Specimen No	Torsion ($\Delta\tau = 410$ MPa) n_1/N_{f1}	Push-Pull $\Delta\sigma$ (MPa)	Exp.Stage I crack length (mm)
S1	0.22	600	2.1
S9	0.22	760	2.1
S10	0.26	760	1.0
S11	0.33	760	2.1
S12	0.53	760	2.2
S13	2.73	760	2.6
S14	0,22	820	2.2
S15	0.33	820	2.4
S16	0.53	820	2.7
S17	0.73	820	2.7

As shown in Table 6.4 the longest experimental dominant Stage I crack is 2.7 mm (2700 μm) compared to the longest computed torsion Stage I crack length of 335 μm for $\Delta\tau$ 410 MPa (see a_t appendix 5). The comparative evaluation is not totally explicit, but it does suggest that although the model is capable of reasonably predicting the lifetime of uninterrupted crack growth, the model predictions of Stage I crack growth are not representative of actual Stage I crack lengths.

6.3 Interaction of Short Fatigue Cracks

The nucleation and early growth of fatigue cracks are considered responsible for a substantial part of the fatigue life of an engineering component. This is attributable to the development and behaviour of MSC, which is fundamentally the important fatigue crack growth process in HCF. The behaviour of short cracks varies considerably depending on the local microstructure and in particular the applied stress level, where the dependency increases with decreasing stress level [137]. Also the mechanisms and interactive relationship between individual short cracks are complex and the non-uniformity in local microstructure can cause differences in fatigue life for the same loading condition [138]. The development of short fatigue cracks generally exhibits a collective behaviour, which is quite different to that of a single long crack. Several workers [82] [83] [135] have observed that in the MSC growth stage that the density of fatigue cracks increases with fatigue cycling. Such that the progressive accumulative behaviour of microcracks continues until at the transition point into the PSC stage where it reaches a maximum value and then decreases as cycles to failure.

The generation and accumulation of microcracks were evident on test specimens that were examined by SEM and the observations of the micrographs indicated similar formations of microcrack patterns as discussed above. The micrographs show that the crack density and length of microcracks change as the number of torsion cycles applied in Phase 1 increased i.e. 0.22-0.73 $N_{f(t)}$ as shown in Fig. 6.7 (a)-(d).

From observations of the micrographs it appears that the density of microcracks increase up to a torsion cycle ratio of $0.53N_{f(t)}$ (see Figs 6.7 (a), (b) and (c)), after which for the torsion cycle ratio of $0.73N_{f(t)}$ (see Fig. 6.7 (d)) the micro-cracks become longer but the crack density decreases. The accumulation of microcracks in this case is consistent with the network of longitudinal microcracks that have been found to develop under torsion loading and where frequent coalescence was reported [17].
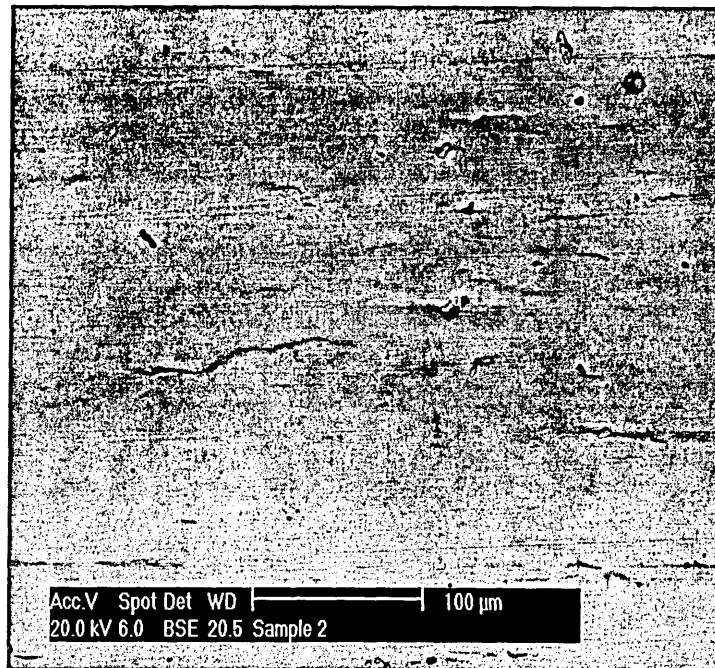
Fig.6.7 (a) Torsion loading $\Delta\tau = 410$ MPa ($0.22N_{f(t)}$)

140
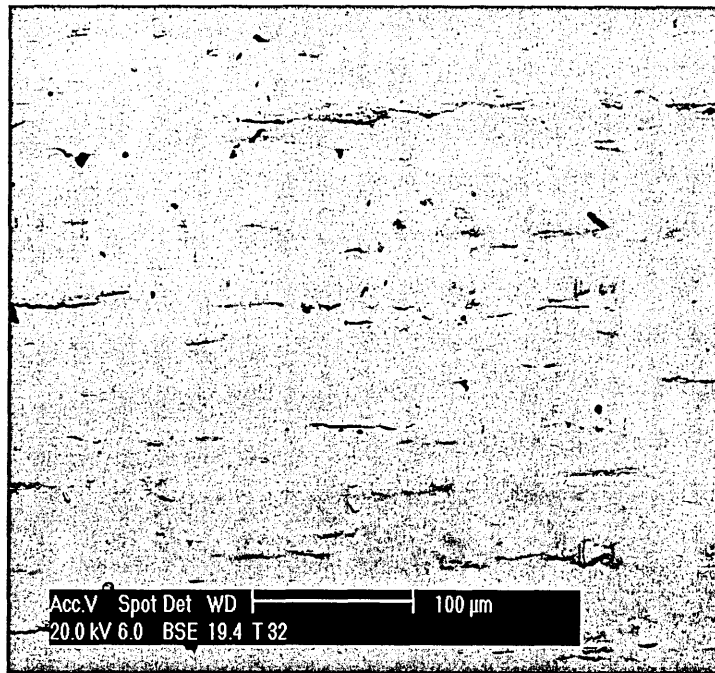
Fig.6.7 (b) Torsion loading $\Delta\tau = 410$ MPa ($0.33N_{f(t)}$)
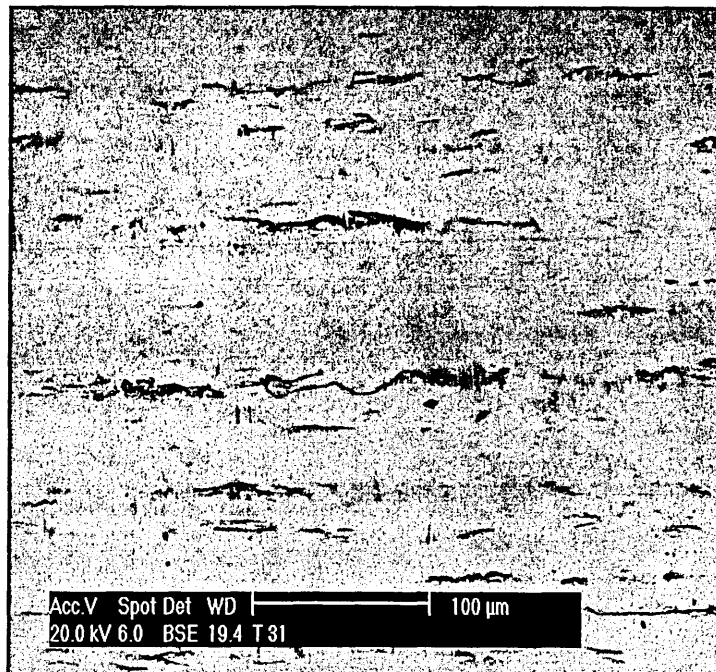
Fig.6.7 (c) Torsion loading $\Delta\tau = 410$ MPa ($0.53N_{f(t)}$)
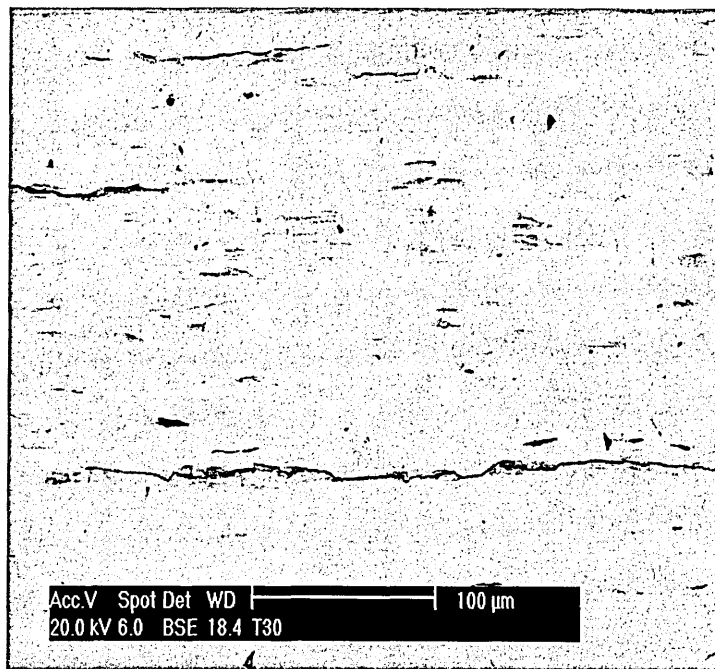
Fig. 6.7 (d) Torsion loading $\Delta\tau = 410$ MPa ($0.73N_{f(t)}$)

The effect of accelerating coalescence of microcracks as fatigue cycling increases is also similar to the interactive behavioural concepts put forward by Zhao [137], where the formation of individual micro-cracks tend to interact and coalesce to become regions where so called dominant effective short fatigue cracks are formed. Although for this work the effects of the apparent differences in crack density during Phase 1 did not reflect any significant changes in the cumulative fatigue lifetimes after the application of the other two Phases (2 & 3). In fact, the lowest cycle ratio values applied for the prior torsion loading ($0.22N_{f(t)}$) actually gave the lowest total cumulative fatigue lifetimes for the higher push-pull load interruptions. Indicating that whilst increased fatigue cycling in the MSC stage may result in increased interactive behaviour of short fatigue cracks, this is not necessarily the dominant activity that effects cumulative fatigue lifetime for this case.

It would therefore suggest from these tests that the application of the push-pull load interruption is an influential factor on crack growth and thus seemingly affects the controlling fatigue mechanism and the final damage summation. The interactive effect the push-pull load interruption had on subsequent crack growth rate was found to be dependent on the applied stress level. For the higher load interruption i.e. $\Delta\sigma >$ 760 MPa the crack growth rate was increased significantly, having a lesser effect as the prior torsion loading cycle ratio increased. Whereas for the lower interruption loads i.e. $\Delta\sigma <$ 640 MPa the crack growth rate was reduced dramatically irrespective of the extent of the prior torsion loading.

The significance of the above effects must be related to the behaviour of short cracks under the different loading conditions, where the mechanisms of crack advance whilst different are complementary or non-complementary to the prevailing fracture process for the current work. How this occurs is probably best understood by examining the individual fracture process under push-pull and torsion loading conditions. From which an evaluation of the crack growth behaviour resulting from the push-pull load interruption maybe considered to substantiate the above effects. To aid this evaluation, representation of the Stage I and Stage II crack orientations with respect to the specimen surface for push-pull and fully reversed torsion loading are shown in Fig. 6.8 [139].

Maximum   Stage I   Transition
shear stress planes   planes and cracks   to Stage II cracks

(a)

(b)
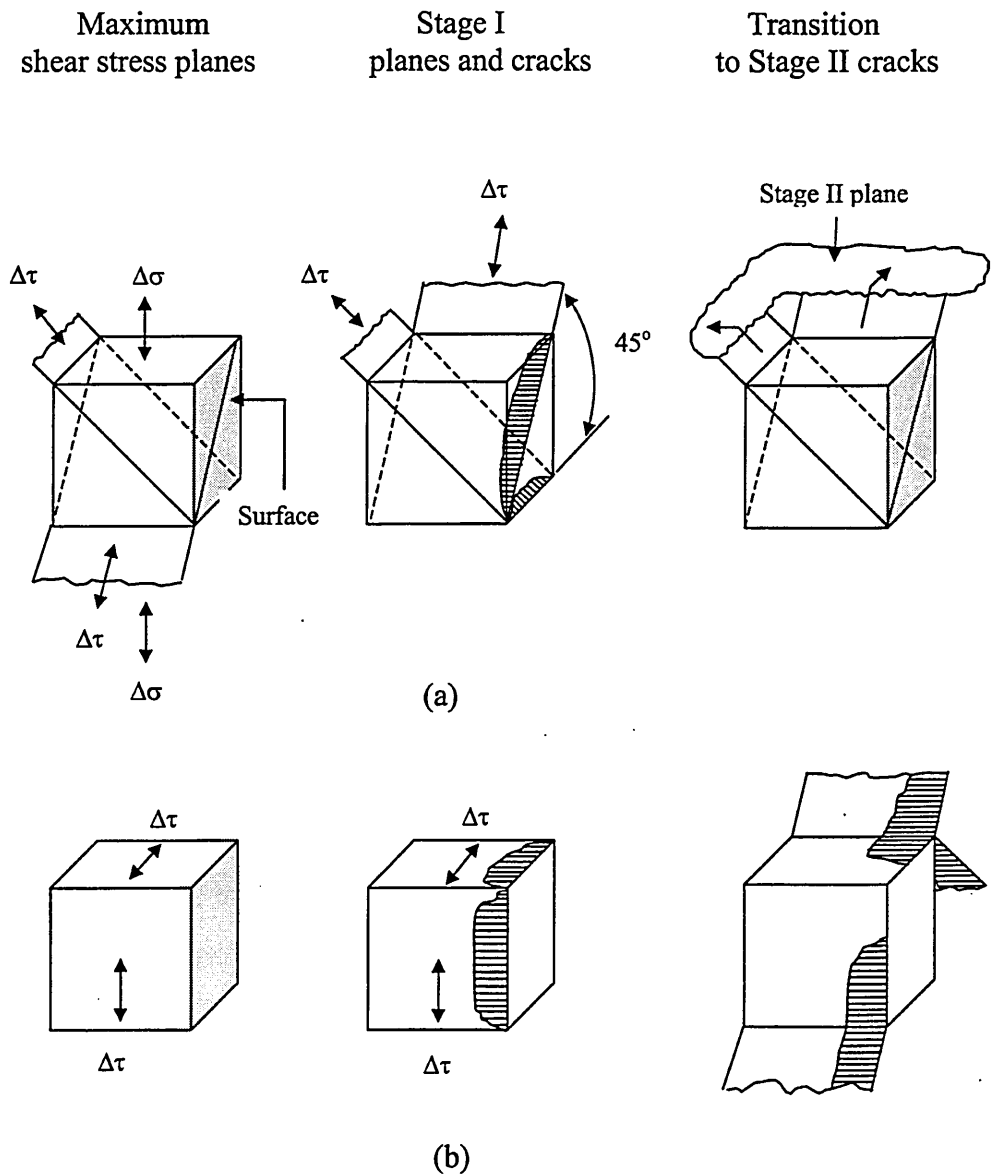
Fig. 6.8 Stage I and StageII crack orientations with respect to the surface of the

specimen for (a) push-pull and (b) reversed torsion loading modes [138]

Now considering the fracture process here, the initial development of Stage I cracks

under torsion loading have maximum shear planes with distinctive orientations, and

one of these orientations coincides with the same orientation as the Stage II crack in

push-pull. It is therefore possible for a dominant torsion Stage I crack to advance

under the influence of the higher push-pull loading, such that the transitional stage under the application of the final torsion loading is encouraged and thus reducing the lifetime of the specimen. However, for the lower push-pull loading no Stage II crack development occurred, but, less favoured slip activation could result to promote the blocking of any future torsion Stage I crack advance. This is considered possible because of the application of the marginal push-pull cycle ratio (4% $N_{f(p-p)}$) and the lower stress amplitude, since the development of Stage I cracks in push-pull can take up to 20% of the lifetime to initiate [50]. Also the relatively fine grain size ($d_{mean} = 6\mu m$) of the specimen material, could have had an influence on the size of Stage I cracks, because finer grained material has been found to exhibit a decrease in crack propagation rate and a smaller non-propagating crack limit [79].

6.4 The Effect of Material Constants on Model Predictions

As discussed in Chapter 5, the material constants were obtained using short crack growth models to obtain an iterative best fit to the fatigue endurance curve for torsion. The models developed were capable of predicting experimental fatigue data for both stress states as shown in Figs. 5.3 and 5.4. The model does not predict a distinguishable fatigue limit even though a fatigue limit threshold was invoked for PSC growth. Consequently the model predictions at or close to the fatigue limit are more conservative compared to the experimental values. Although the error between the predicted and model results may have been somewhat closer if a greater number of experimental results had be achieved and statistically evaluated. Since significant scatter is apparent in S-N curves and scatter tends to increase as the stress amplitude decreases [140]. However, above the experimental fatigue limit both model curves

gave good agreement with the experimental data, suggesting that the procedures for deriving the material constants give good approximations. The derivation of which indicated that the short crack growth equations could adequately reflect the uniaxial and torsion fatigue characteristics of this 0.42% carbon steel.

The use of the computer software to obtain the material constants by iteration and interpolating the model S-N curve to the experimental data proved an extremely capable technique. The sensitivity in which each parameter affected the model curve made it easy to achieve good correlation to the experimental data. This was evident by the closeness of curve fitting achieved by different persons that was carried out independently and having only a known base value of parameters taken from other experimental work obtained for a similar material.

To demonstrate the sensitivity of the iteration technique used and the effect the changes the material constants had on the torsion model fatigue curve; each material constant is changed independently as shown in the following figures. For instance in Fig. 6.9 the material constant A is increased in two steps, leaving all the other constants to remain the same.

(Note :- for greater clarity the data points have been included for the original model fatigue curve in all corresponding figures).
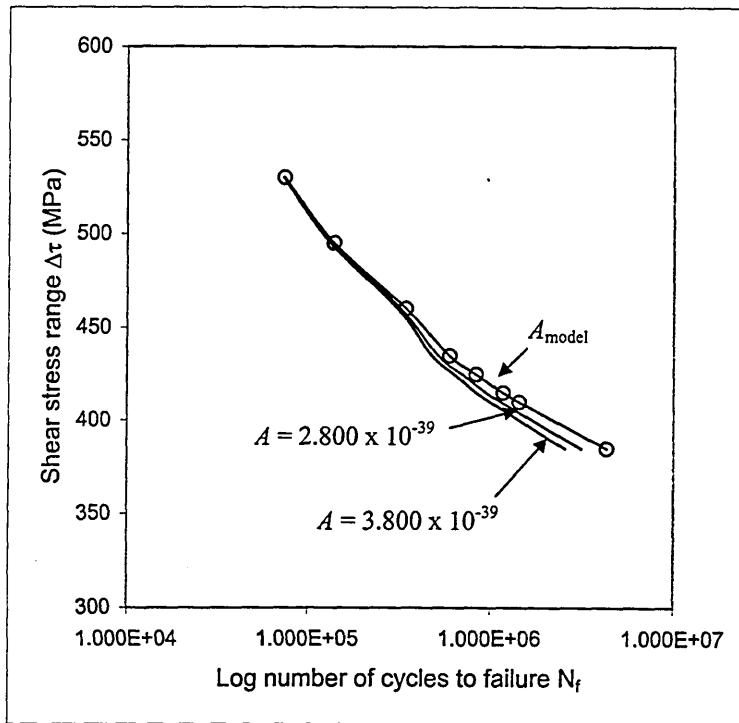
Fig. 6.9 Effect on model torsion endurance curve of changes in material constant A

The changes in the fatigue curves in Fig. 6.9 are more significant at the lower stress amplitudes, showing the increased effects of MSC dominance. Changes, which are expected since the material constant A, are a microstructural coefficient for MSC growth. Whereas, the influence is to the contrary for changes in the material constant B, since this has greater effect on PSC growth and is more pronounced at higher stress amplitudes. The decreasing influences of MSC growth and the increasing influences on PSC growth are reflected by the changes in the model fatigue curve as shown in Fig. 6.10.
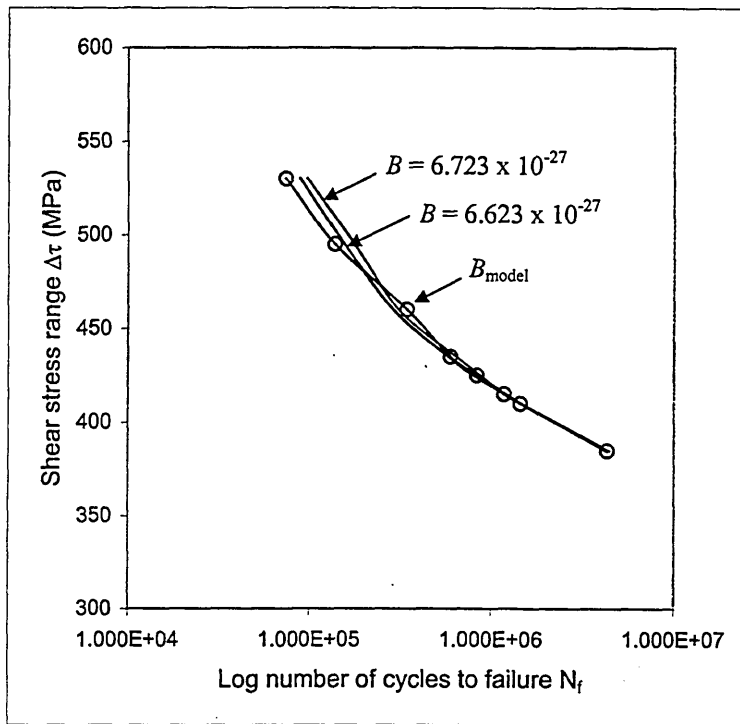
Fig. 6.10 Effect on model torsion endurance curve of changes in material constant B

As discussed earlier in Chapter 5 on page 108 the material constant D is normally derived empirically from crack growth data and reportedly [50] the projected crack length (a_{th}) (see Fig 5.2) is associated with the start of a PSC crack and represents the short crack threshold since $da_{th}/dN = 0$. The parameter D is solely dependent on the physical properties of the material and since it is associated with this threshold condition for PSC growth (Stage II crack growth) it is a stress independent parameter. The effects on the model curve of changes in the parameter D are shown in Fig 6.11. It can be seen in Fig 6.11 that small changes in the parameter D give noticeable changes in the model curve and these effects are consistent with a relative increase in the material's fatigue strength, which are in this instance proportionate to the increases in the parameter D.

148
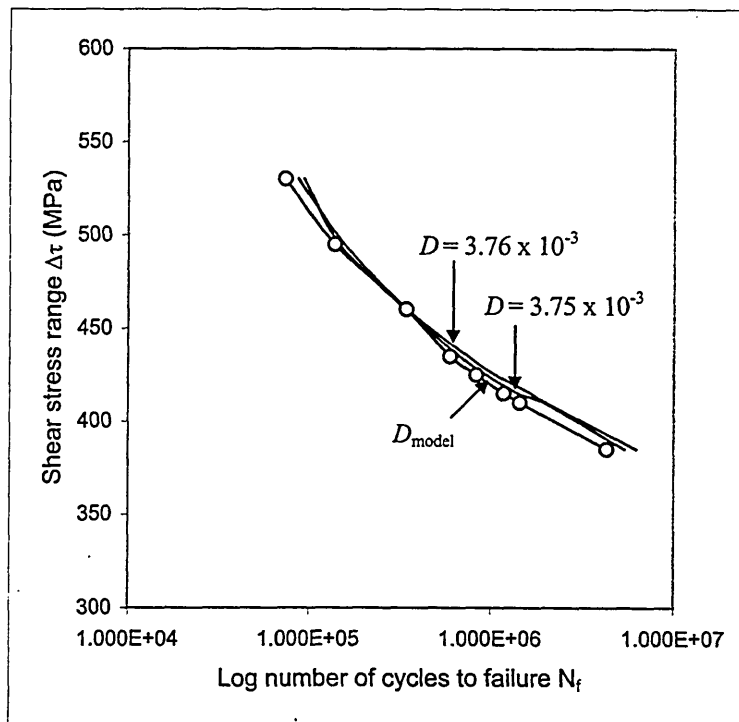
Fig. 6.11 Effect on model torsion endurance curve of changes in material constant D

The material parameter m and n are exponents of the MSC and PSC growth equations respectively and they reflect the non-linearity relationship of crack growth for these separate and distinctive crack growth phases. Such that, the material constant m reflects the retardation in crack growth associated with the presence of microstructural barriers of the shear dominant Stage I crack growth phase. Whereas the material constant n reflects acceleration in crack growth associated with PSC growth, at the start of the tensile dominant Stage II crack growth phase. The values for these exponents depend on the physical properties of the material under these separate conditions of crack growth and differ for different materials.

The effect on the model curve of changes of the exponent m and n are shown in Fig. 6.12 and 6.13 respectively.

149
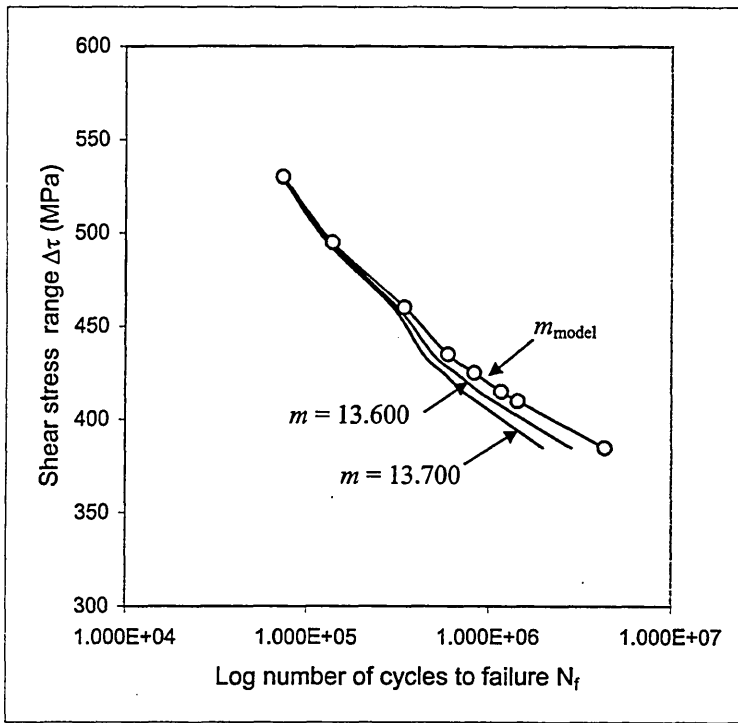
Fig. 6.12 Effect on model torsion endurance curve of changes in material constant *m*
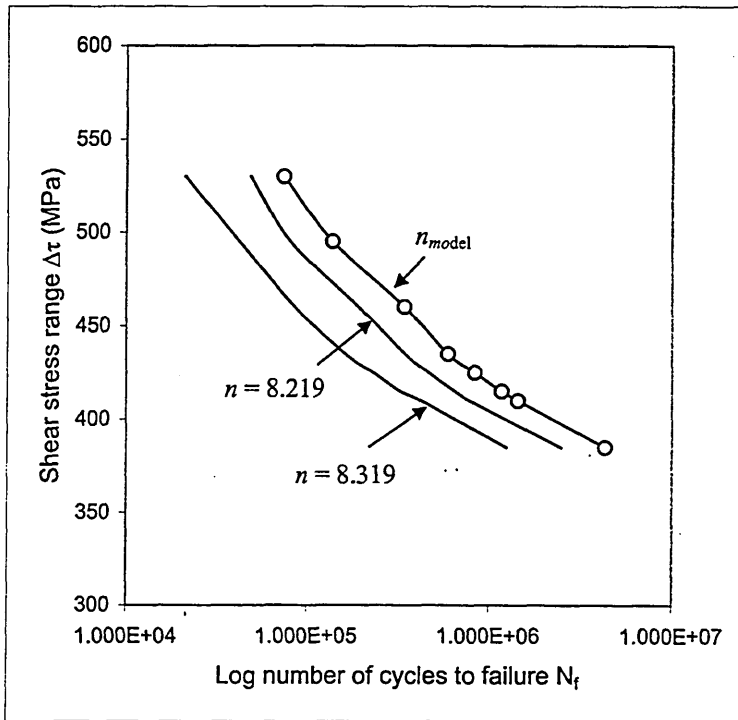
Fig. 6.13 Effect on model torsion endurance curve of changes in material constant *n*

It can be seen from the above figures the effect on the model fatigue curve that changes of all these material constants are noticeable. The material constants show distinguishable but differing effects which allows for ease of attaining interpolated data to experimental data. This is emphasised particularly strongly by changes in the material constant n, where only marginal changes in n have a dramatic effect on the model fatigue curve (see Fig. 6.13).

The changes in the material constant have been carried out to examine the effects each has on the model fatigue curve for simplicity, but the collective effect of the material constants is obviously more involved. This is because the derivation of the model fatigue calculations are cumulative of the short and long crack growth equations for all stress amplitudes above the model's fatigue limit threshold. Therefore the material constants can have an interactive effect and as such have to be set within the overall experimental fatigue data. However, not withstanding this point it has been shown that material constants can be approximated adequately by this iterative method.

Although only cases for increased values for the material constants have been considered the effects on the model fatigue curve for decreased values are similar, but have opposite effects on the model curve to those shown

6.5 The Effect of α on the Model Predictions

The model parameter d for this work was calculated from the statistical evaluation of ferrite grain size measurements from a sectioned sample of an untested specimen as

discussed in section 5.2.1. The value of d was taken to be representative of the ferrite grain sizes (upper and mean) of the material and used in the model in the MSC growth equation da/dN $= A\Delta\sigma^m(d_i\text{-}a)$. The controlling parameter for MSC growth into the next grain is a function of the value αd_i, which reflects the position of crack growth that equates to the point immediately before transition occurs into the next grain. The value of $\alpha = 0.95$ taken for this work recognised that a degree of micro-plastic deformation existed ahead of the crack tip and reached a critical size which equated in principle to the unlocking mechanisms of plastic slip into the next grain [133]. This is a fatigue process that is acknowledged as a prerequisite for the continuation of crack growth into the next grain, but at what precise position in the grain this occurs is difficult to ascertain as discussed earlier in Chapter 5. The effect on the model curve of different values of α for torsion loading is shown in Fig. 6.14.
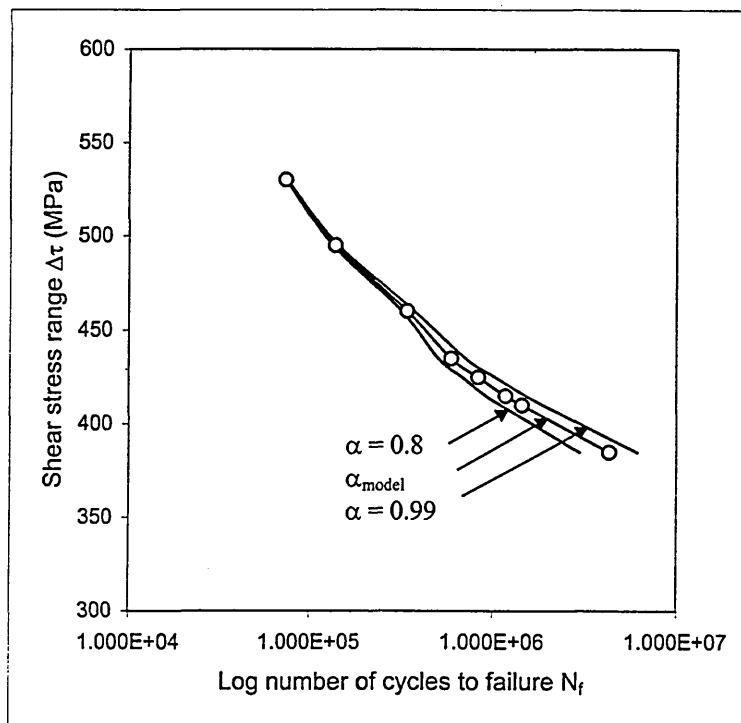
Fig. 6.14 The effect on fatigue lifetimes of different values of α

In Fig.6.14 the comparisons to the model fatigue lifetime for torsion loading of $\Delta\tau$ 410 MPa and $\alpha = 0.95$ give differences in lifetimes of -24% and +30% for $\alpha = 0.80$ and $\alpha = 0.99$ respectively for the same torsion stress amplitude. Obviously there are wide variations in the values of N_f for different values of α, but, the difference $\rightarrow 0$ as the stress amplitude increases, due to the reducing influence of MSC growth. This influence on MSC growth is because the function $f(\alpha) = \alpha d_i$ used in the model, is taken to represent the crack length which equates to a proposed equilibrium position. A position where the localised stress concentration at the crack tip corresponds to the microstructural strength of the material near the grain boundary or some other microstructural feature. This therefore reflects a higher or lower fatigue lifetime to correspondingly higher or lower value of α for MSC growth for a given stress amplitude.

However, the differences in the model fatigue lifetimes may appear significant for changes in α, but they are not unrepresentative of the scatter in experimental fatigue lives that are prevalent at or near the fatigue limit. A factor that is associated mainly with localised differences in microstructural properties of the material and as such affect MSC growth [20]. Although, the degree of scatter can differ for different materials, but generally ductile materials such as the medium carbon steel used here exhibit a greater degree of scatter.

For simplicity the value α in the model was taken to remain constant irrespective of crack length, but this is idealistic rather than realistic since the stress concentration will increase as the crack length increases and therefore α should decrease. Although the degree of stress concentration is complex to resolve for an advancing crack on a

microscopic scale. Especially through a non-uniform grain structure such as the material used for the current work. The computer program does however, allow for the easier derivation of the value of α to be used in the evaluation of the model endurance curves. This was reflected by the good approximation of the predicted to the experimental fatigue lifetimes for this material as shown by calculated fatigue lifetimes in Table 5.1 and 5.2.

6.6 Use of Neural Networks for the Determination of d

Neural networks is another computational method that has been used increasingly in a range of engineering applications such as condition monitoring and process control to extract key characteristics from large complex sets of data. Recently neural networks have been used [141] to model the chaotic behaviour of the growth of short fatigue cracks, which was exclusively trained and tested on experimental data obtained by Hobson [93][94]. The neural network used in this study was the multilayer perceptron neural network using the back-propagation algorithm as detailed in reference [142]. Seed and Murphy [140] used the neural network simulation for the determination of the parameters α, d and C of the non-linear short crack growth equation [93] of the form given below,

$$da/dN = Ca^{\alpha}(d-a)^{1-\alpha} \ \dots\dots\dots\dots\dots\dots\dots\dots\dots\dots\dots\dots (6.9)$$

The parameter d was reportedly [140] derived by eliminating α and C from equation (6.1) to obtain the following expression,

154

$$\ln\left[(da/dN)_2\,(d-a_1)/(da/dN)_1(d-a_2)\right]\ln[(a_3(d-a_2)/a_2(d-a_3)] -$$

$$\ln[(da/dN)_3\,(d-a_2/(da/dN)_2(d-a_3)]\ln[(a_3(d-a_1)/a_2(d-a_2)]$$

$$= 0 \quad\dots\dots\dots\dots\dots\dots\dots\dots\dots\dots\dots\dots\dots\dots\dots\dots\dots\dots\dots \text{(6.10)}$$

where subscripts 1, 2 and 3 indicate the three different samples points. Equation (6.10) is then solved by iteration using the Newton-Raphson method.

The predictions of parameter d by this method i.e. $63 < d < 400$ (μm), increased considerably as the stress amplitude increased. Notably different from that taken by Hobson, who equated $d = 116\mu$m the mean ferrite plate length. The differences are probably not unexpected since the effect on short crack growth decreases as the stress amplitude increases and as such the short crack growth data is less significant and therefore errors are more pronounced. However, even the predictions $63 < d < 219$ (μm) for the lower stress amplitude (639 MPa) are somewhat under and over approximated. The above approximations for d appear too conservative and non-conservative to give reasonable fatigue lifetime predictions. Since only slight changes in the value of d affects the fatigue curve quite considerably as shown in Figs. 6.15 and 6.16. Which supports the comments made by Seed and Murphy [139] that "although the determination of an exact value of d is difficult, it is important that d is not underestimated when performing lifetime predictions".

Neural networks is obviously best suited for analysing large amounts of chaotic data and it maybe a valuable computational technique for short crack growth analysis if specifically adapted for low stress amplitude conditions.
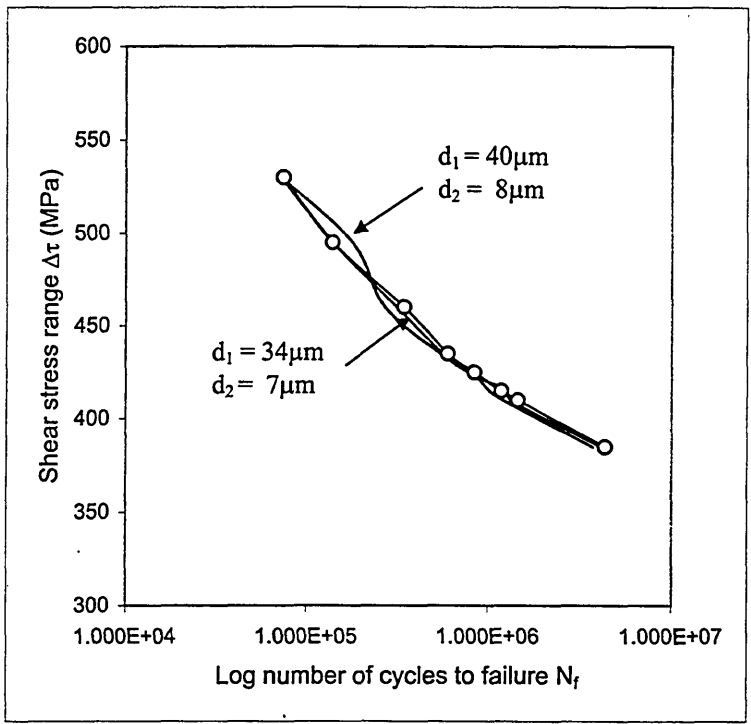
Fig. 6.15 Parameter d increasing of reversed torsion loading
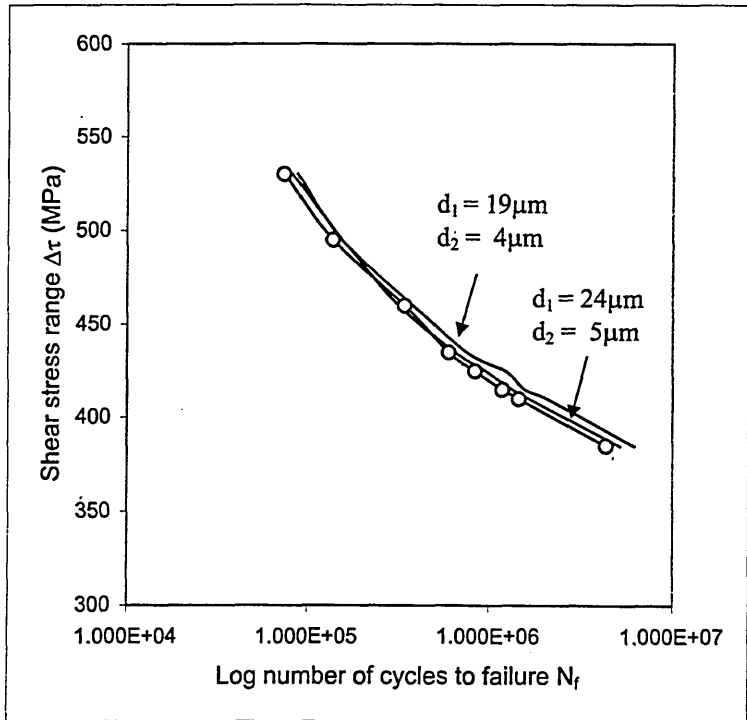
Fig. 6.16 Parameter d decreasing of reversed torsion loading

156

6. 7.1 Introduction

The crack patterns of specimens subjected to the different multi-phase loading conditions were analysed by taking micrograph observations of microcrack development and fracture of the fatigued specimens using a SEM. The micrographs observations were mainly of microcracks that had developed at positions within close proximity to the dominant cracking systems. This was necessary particularly to record crack initiation sites within the grain structure since reversed torsion loading promotes frictional surface contact of the dominant crack faces and generally destroys the crack initiation site.

Micrographs of sectioned specimens were taken to observe the differences in crack growth behaviour of non-propagation and propagation of shear dominated cracks. Micrographs were also taken of the fracture surface of a specimen subjected to a multi-phase loading regime, to examine the fracture process from the crack initiation site to complete fracture.

6.7.2 Fatigue Crack Development

It was found that the dominant fatigue crack system of failed specimens for the multi-phase loading is similar to that of pure torsion loading. A micrograph of the dominant crack profile of a failed specimen subjected to multi-phase loading (torsion - push-pull - torsion loading to failure sequence), is shown in Fig. 6.17.
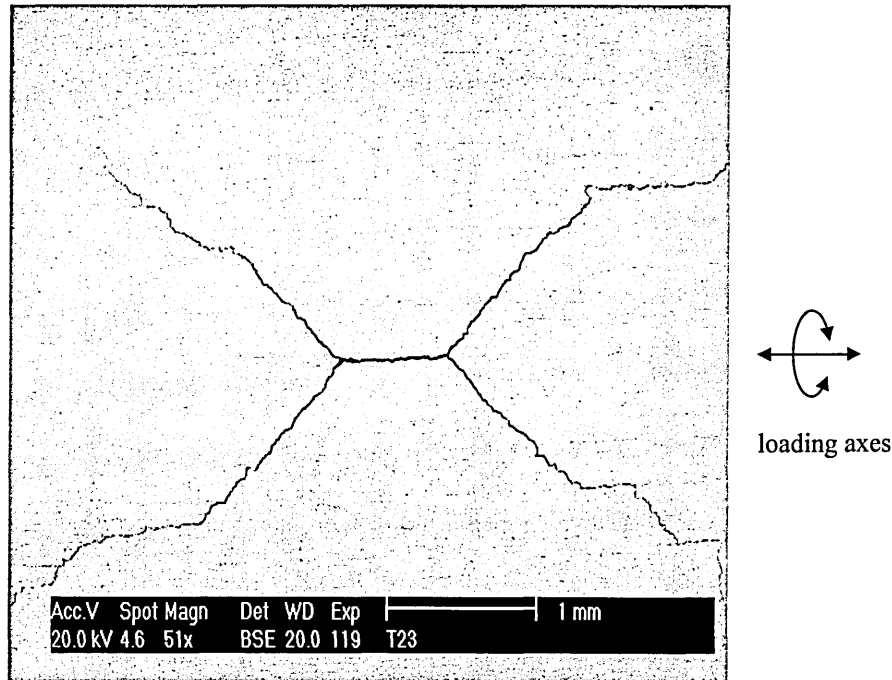
loading axes

Fig. 6.17 Dominant crack system for multi-phase loading sequence

$$(0.26 \ n/N_{f\,(t)\,410\,MPa} - 0.04 \ n/N_{f(p\text{-}p)\,760\,MPa} - n/N_{f\,(t)\,410\,MPa} \rightarrow)$$

The fatigue crack system of the failed specimens for the multi-phase tests being similar to that of pure torsion loading are probably not unexpected in this case because of the low cycle ratio (4% $N_{f(p\text{-}p)}$) of the push-pull load interruption. The only difference was usually a longer Stage I crack length which could extend up to 2.7 mm before branching into the Stage II crack planes, that generally related to the increasing effect of the prior torsion cycle ratio. Where the exceptions to this could be as a result of the effect of the push-pull load interruption on MSC growth and possibly some localised differences in the microstructure of the material.

It was discussed in section 5.2.1 that ferrite grains are generally the sites for crack initiation for a medium carbon steel since the ferrite grains are much weaker than the

158

pearlite grain structure. However, as stated in the introduction of this chapter the crack initiation sites are usually impossible to determine because of frictional rubbing of the crack faces, due to the action of shear crack growth as a result of reversed torsion loading. Also in some cases it was found that the predominance of the torsion loading caused a degree of 'spalling' of material that occurred around the initiation site which could be seen to develop on a macroscopic scale by the use of a magnifying glass whilst the test was in progress. Fig. 6.18 shows a micrograph of the frictional disturbance that has been somewhat extreme because of the interaction of Mode I and Mode II crack growth causing crack branching. The combination of such a localised concentrated crack growth pattern would in effect make it particularly problematic to distinguish the crack initiation site. The specimen in this case was subjected to multi-phase loading (torsion - push-pull - torsion loading to failure).

specimen axis
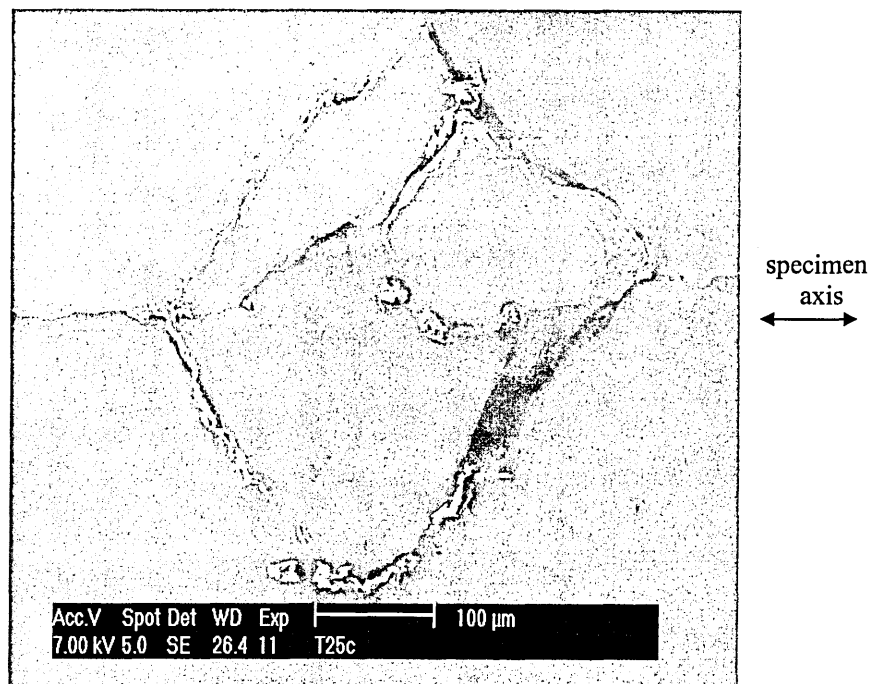
Fig. 6.18 The effects of crack branching and frictional disturbance

$(0.33 \ [n/N_{f\,(t)}]_{410\,MPa} - 0.04 \ [n/N_{f(p-p)}]_{820\,MPa} - [n/N_{f(t)}]_{410\,MPa} \rightarrow)$

159

It was discussed in Chapter 3 that ferrite grain sizes would be taken as parameter d_i for the MSC growth model equation (5.22). This was substantiated to be correct since it was found that for all the micrographs taken, cracks had initiated in ferrite grains.

The majority of Stage I microcracks observed were generally aligned longitudinally to the specimen axis with very few in the transverse plane, probably due to the effects of grain directionality of the material. Fig. 6.19 and Fig. 6.20 are micrographs of the surface of the specimen subjected to multi-phase loading, which show clearly torsion Stage I cracks that have initiated in a ferrite grain, but in different planes relative to the specimen axis.
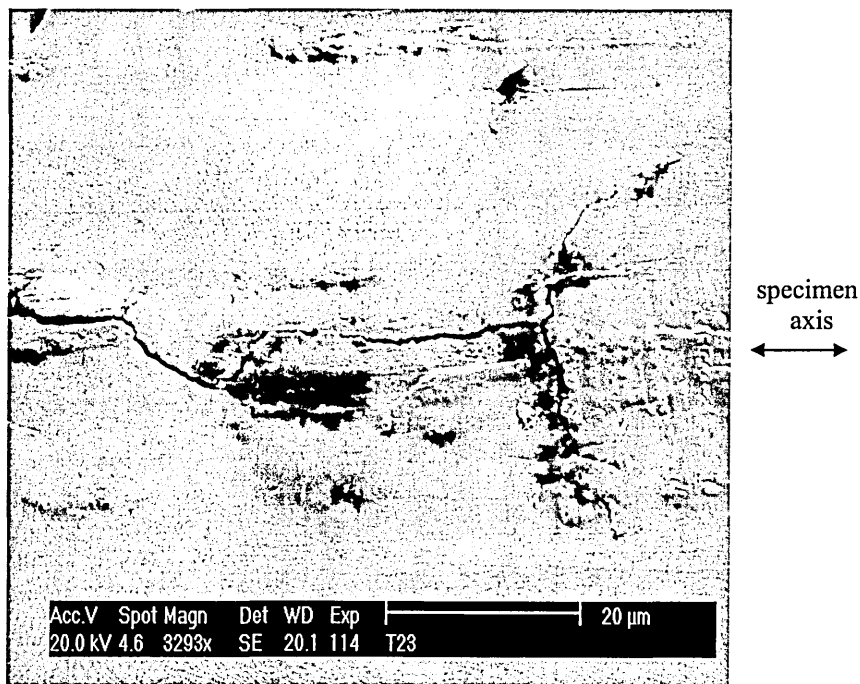
Fig. 6.19 Torsion Stage I crack in a ferrite grain (longitudinal plane)

$(0.26 \, [n/N_{f\,(t)}] \, _{410\,MPa} - 0.04 \, [n/N_{f(p-p)}] \, _{760\,MPa} - [n/N_{f\,(t)}] \, _{410\,MPa} \rightarrow)$
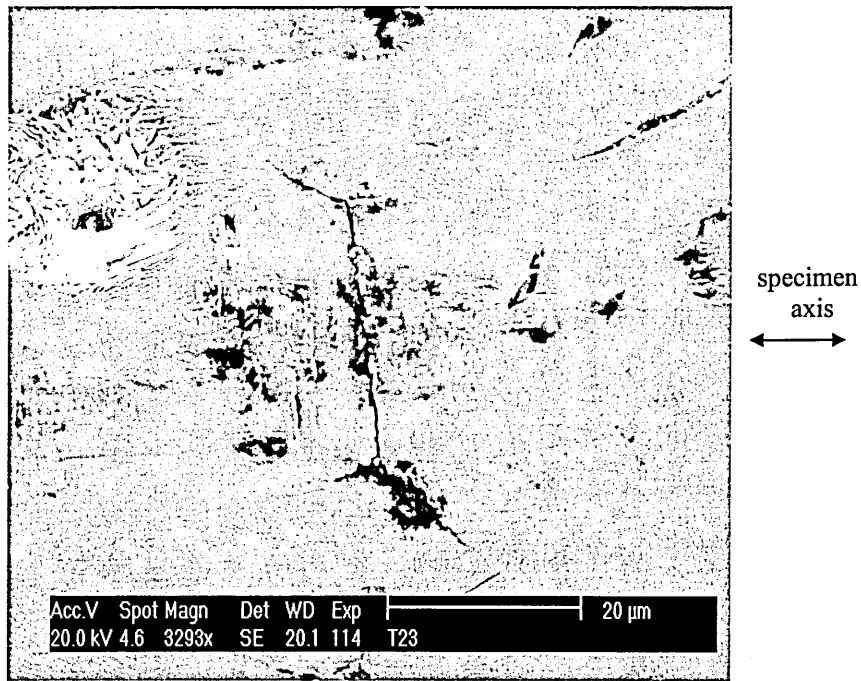
Fig. 6.20 Torsion Stage I crack in a ferrite grain (transverse plane)

$(0.26 \ [n/N_{f\,(t)}] \ _{410\,MPa} - 0.04 \ [n/N_{f(p-p)}] \ _{760\,MPa} - [n/N_{f\,(t)}] \ _{410\,MPa} \rightarrow)$

Figs. 6.19 and 6.20 show fatigue cracks that are in positions that reflect the complimentary torsion shear planes and transitional stage from Stage I to Stage II crack growth which is transgranular. The micrograph also shows the possible arrest position for these secondary-cracking systems (not associated with the dominant crack) which are typical for this material. In so much that a crack initiated in the weaker ferrite grain and in overcoming the grain boundary developed into a Stage II crack which then is retarded or arrested by the stronger pearlite grain structure.

The development of a Stage I crack in a ferrite grain can also be seen in the micrograph of specimen subjected to multi-phase loading, but, which did not fail as shown by Fig 6.21. Interestingly the Stage I crack appears to be associated with the boundary of the ferrite platelet.

161

specimen axis
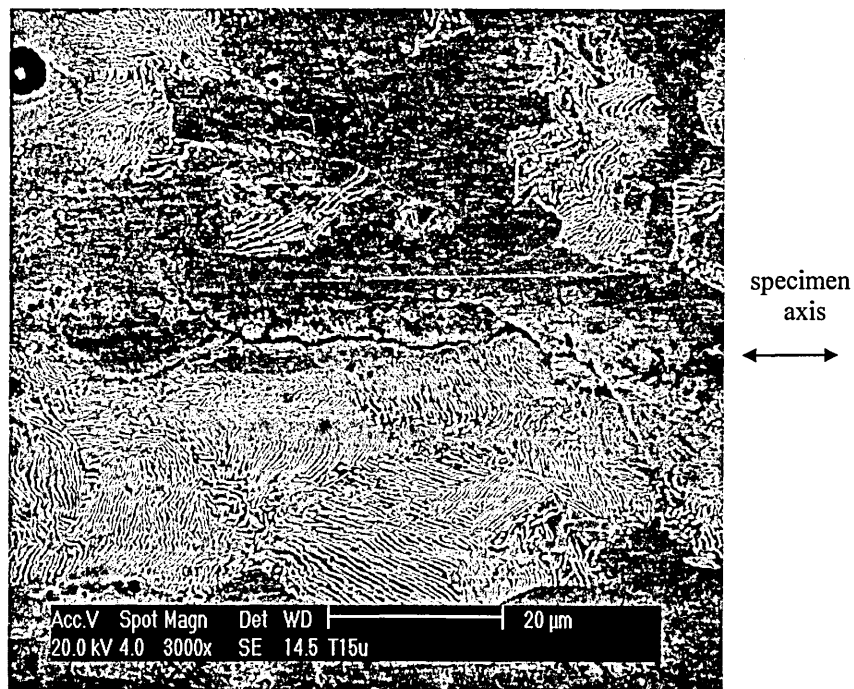
Fig. 6.21 Stage I crack (specimen not failed)

$$(0.22 \ [n/N_{f\,(t)}] \ _{410\,MPa} - 0.04 \ [n/N_{f(p-p)}] \ _{640\,MPa} - [n/N_{f\,(t)}] \ _{410\,MPa} \rightarrow)$$

Observations were also carried out of surface microcracks of specimens that did not

fail through the development of a dominant Stage II crack, but, which did however

reach a pre-determined fatigue endurance limit i.e. $\Sigma n/N_f > 2.45$. It would be expected

that specimens that had undergone such high fatigue cycles that non-propagating

Stage I crack growth should be a prominent feature. This was substantiated by the

detailed examination of surface area of the specimens and no apparent Stage II crack

growth was observed. Although, this may have been different if the practicality of

allowable testing time had not been a factor then the Phase 3 torsion loading fatigue

cycles could have been greater.

The micrographs of the specimens that were subjected to multi-phase loading and did

not fail, revealed signs of considerable plastic deformation which extended over the

162

surface area of the specimens The positions of these intrusions and extrusions were generally coincidental with the directions of the longitudinal torsion shear planes. These extrusions are visibly dominant on the surface of the specimens as shown by the micrograph in Fig. 6.22.
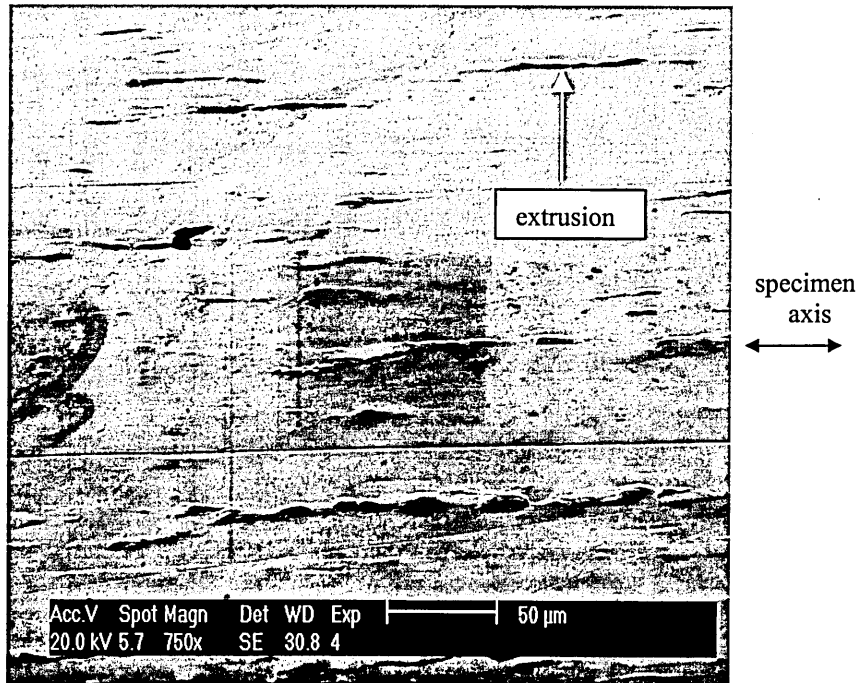

Fig 6.22 Surface extrusions on a specimen (not failed) subjected to multi-phase loading $(0.53\ [n/N_{f\,(t)}]\ _{410\,MPa} - 0.04\ [n/N_{f(p\text{-}p)}]\ _{600\,MPa} - [n/N_{f\,(t)}]\ _{410\,MPa} \rightarrow)$

It can be seen more clearly in Fig. 6.23 that the initiation of the torsion crack in this instance is related to a localised area of plastic deformation. Showing that the plastic deformation is part of the evolutionary process for multi-phase fatigue cycling and subsequently is the likeliest birthplace for Stage I cracks.

specimen
axis

Acc.V Spot Magn Det WD Exp   20 μm
20.0 kV 4.5 3456x SE 30.9 2
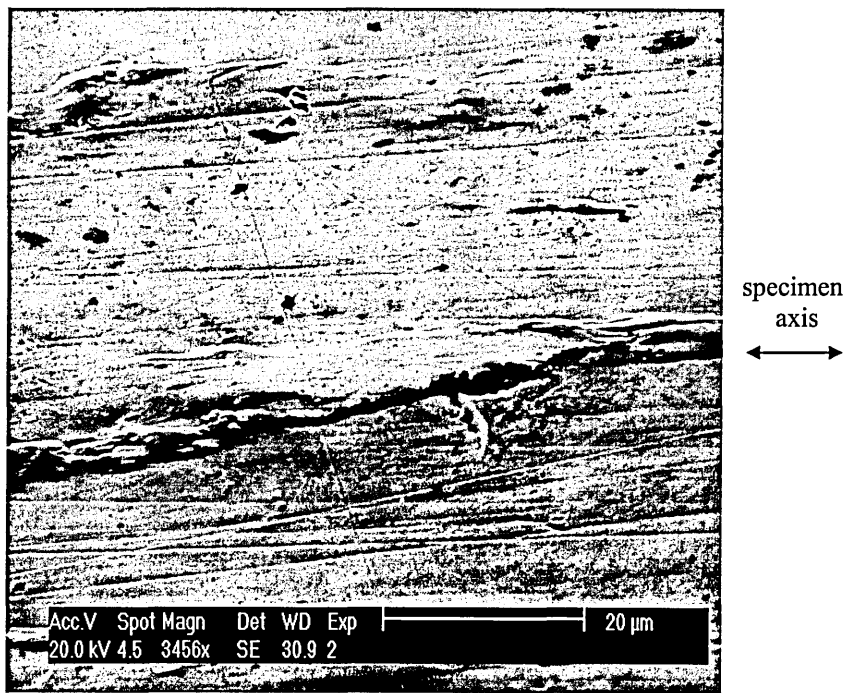
Fig. 6.23 Stage I crack initiation site of a specimen (not failed) subjected to multi-phase loading (0.53 $[n/N_{f\,(t)}]$ 410 MPa - 0.04 $[n/N_{f(p-p)}]$ 600 MPa - $[n/N_{f\,(t)}]$ 410 MPa →)

It was evident from observations of the micrographs of the surface of specimens that did not fail that only torsion Stage I cracks of a varying lengths were present and Fig. 6.24 shows one of the longer Stage I cracks found, which is approximately 200 μm in length. Although the profile of this crack has sharp defined minor changes in directionality, which could suggests that its length be attributed to the coalescence of smaller microcracks.

specimen
axis

⟷
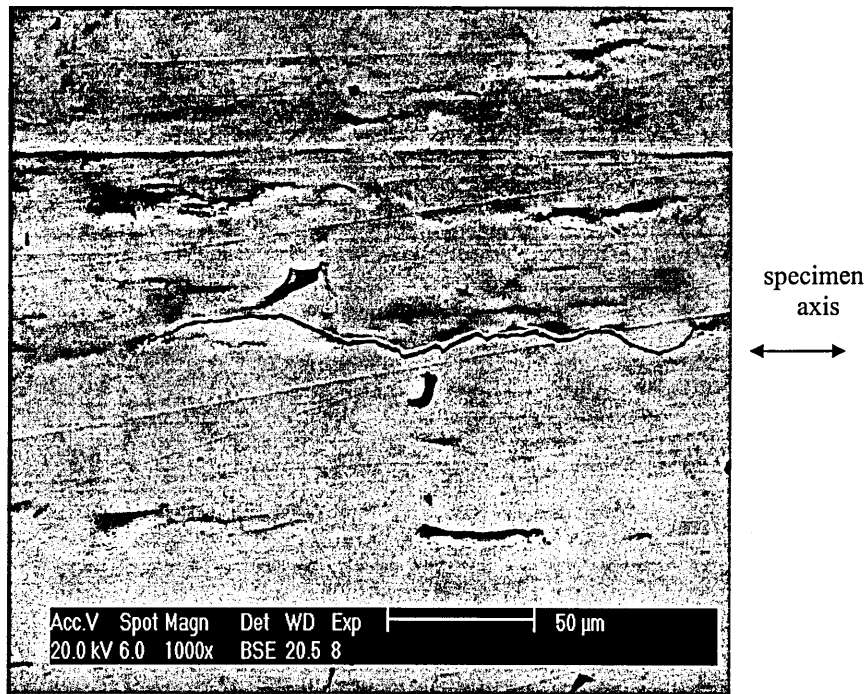
Fig.6.24 A long Stage I crack of a specimen (not failed) subjected to multi-phase loading ($0.53 \ [n/N_{f\,(t)}]$ 410 MPa $- \ 0.04 \ [n/N_{f(p-p)}]$ 600 MPa $- \ [n/N_{f\,(t)}]$ 410 MPa $\rightarrow$)

It is evident from the micrograpghs taken that the surface of the specimens changes considerably by the fatigue process under multi-phase loading. However, the changes in the surface topography of the specimens were not only confined to the specimens that had not failed and had undergone relatively extensive cumulative fatigue cycles ($>2.25 \ n/N_f$), but were also evident on specimens that had failed.

The changes in the surface topography, which show surface extrusions and Stage I crack growth present around and integrated into the Stage II crack system of a specimen subjected to multi-phase loading that failed, is illustrated in Fig. 6.25

165
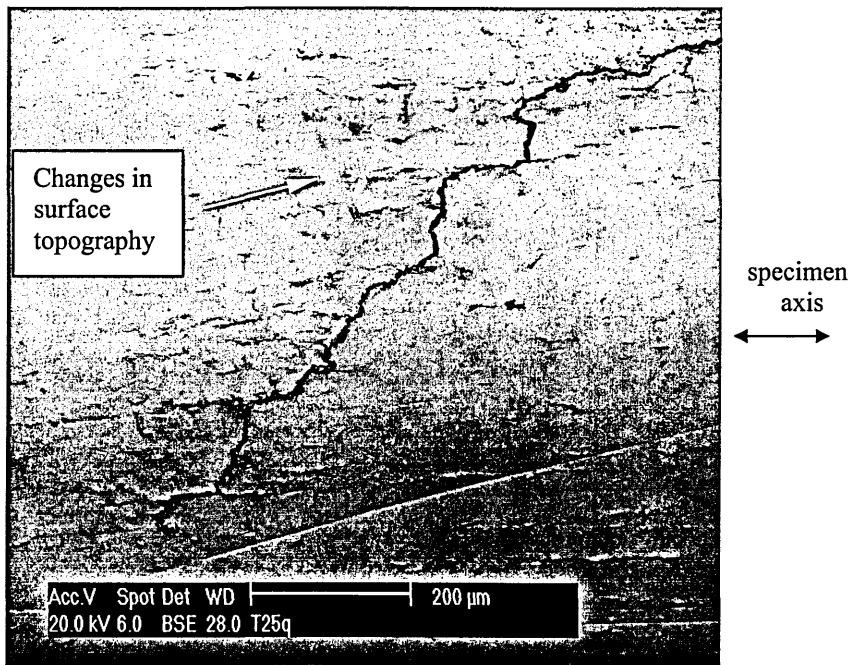
Fig. 6.25 Extrusions around a Stage II crack system

$(0.33\ [n/N_{f\,(t)}]\ _{410\,MPa} - 0.04\ [n/N_{f(p\text{-}p)}]\ _{820\,MPa} - [n/N_{f\,(t)}]\ _{410\,MPa} \rightarrow)$
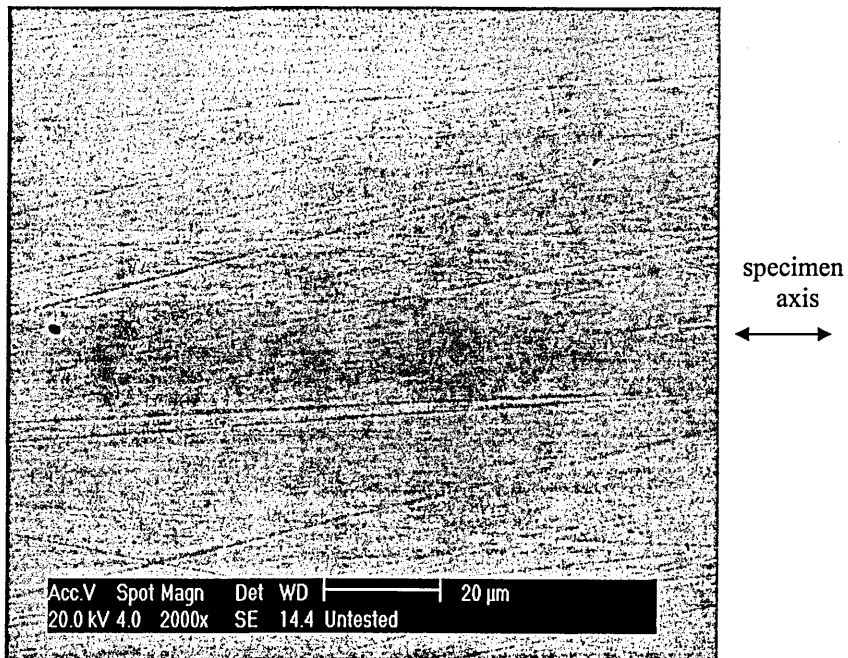

Fig. 6.26 Surface of an untested specimen

For comparative purposes to show the extent of the surface deformation process that occurs on the surfaces of specimens subjected to multi-phase fatigue cycling, the surface of an untested specimen is shown in Fig. 6.26.

6.7.3 Crack Growth through Section of Specimen

Specimens were sectioned to examine how cracks had developed in the material for specimens that had not failed and failed in accordance with the failure definition for the multi-phase tests outlined in section 3.5.1. For the specimen that did not fail the specimen was carefully sectioned at the centre of the hourglass section where Stage I cracks were dominant. Whereas, for the specimen that had failed this was sectioned in such a manner that both the Stage I (section x-x) and Stage II (section y-y) crack systems could be examined as shown in Fig 6.27.
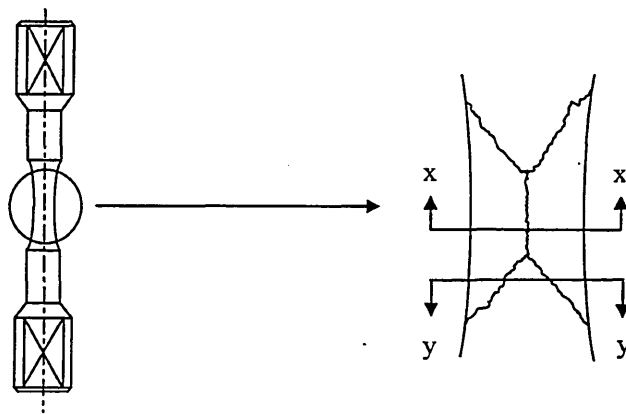
Fig.6.27 Schematic of specimen section positions

The micrographs of cracking system of a sectioned specimen that did not fail are shown in Fig. 6.28 (a) and (b).

167
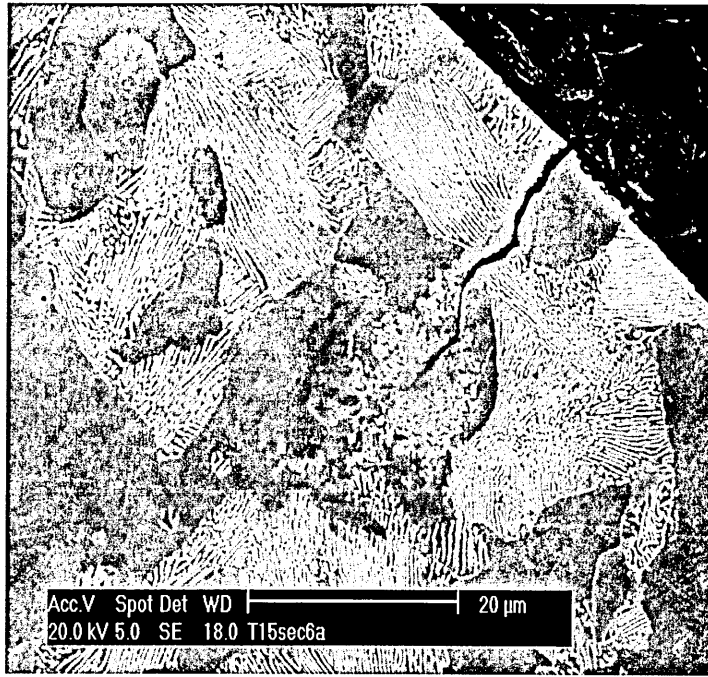
(a)
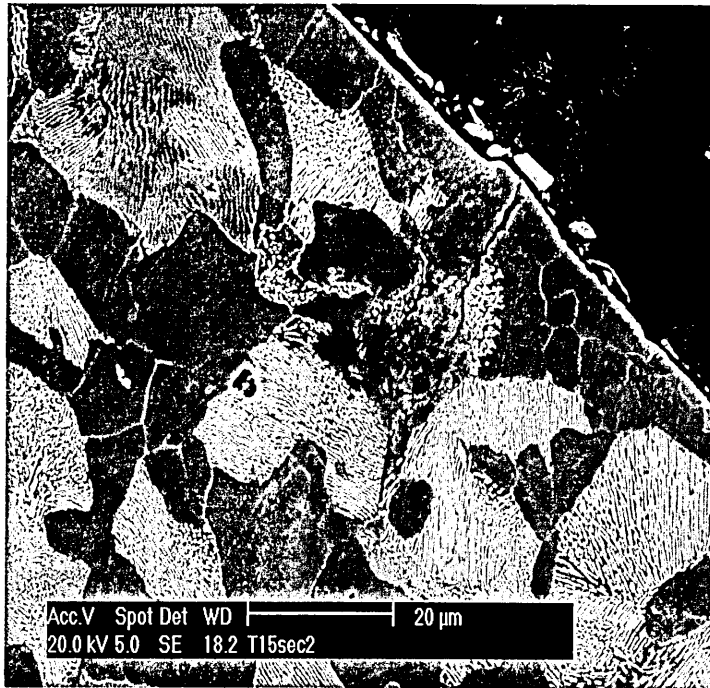
(b)

Fig. 6.28 (a) and (b) Stage I crack (specimen not failed)

$(0.22\ [n/N_{f\,(t)}]\ _{410\ MPa} - 0.04\ [n/N_{f(p\text{-}p)}]\ _{640\ MPa} - [n/N_{f\,(t)}]\ _{410\ MPa} \rightarrow)$

168

It can be seen in Figs 6.28 (a) and (b) that the shear cracks generally extended into the material for approximately 20 μm for the specimens that did not fail. It can also be seen in Figs 6.28 (a) and (b) that the Stage I microcracks have negotiated preferential routes along the grain structure to align with the weaker ferrite material.

In Fig. 6.29 again of a specimen that did not fail some degree of branching has occurred, to suggest that the push-pull load interruption has affected the prior torsion crack profile.
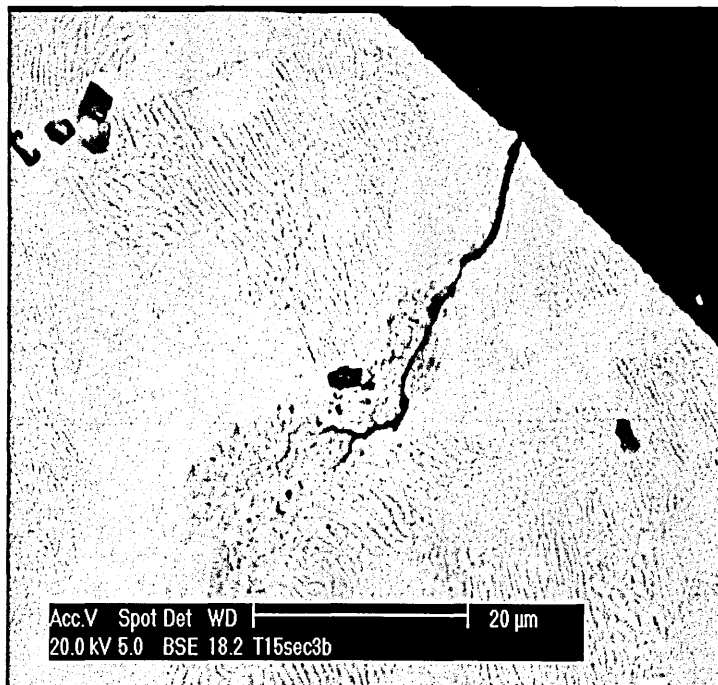

Fig. 6.29 Crack branching associated with the interrupted push-pull loading

$(0.22\ [n/N_{f\,(t)}]\ _{410\,MPa} - 0.04\ [n/N_{f(p-p)}]\ _{640\,MPa} - [n/N_{f\,(t)}]\ _{410\,MPa} \rightarrow)$

The changes in direction of the crack are coincident with the orientation of a Stage I crack in push-pull and this could explain why the crack did not continue to propagate at resumption of the torsion cycling. That no other cracks of this section have similar branching characteristics could be because of the different crack orientation normally associated push-pull Stage I crack and thus excluded by the sectioning process. Alternatively, the effect on the prior torsion crack growth by the push-pull load interruption is much more localised because of the complexity of the microstructure of the material creating a non-overload crack blunting effect.

The shear cracks for the specimens that failed extended into the material considerably further compared to those that did not fail as shown by Fig. 6.30.


Fig. 6.30 Stage I crack (specimen failed)

$(0.33 \: [n/N_{f\,(t)}] \: _{410\,MPa} - 0.04 \: [n/N_{f\,(p-p)}] \: _{820\,MPa} - [n/N_{f\,(t)}] \: _{410\,MPa} \rightarrow)$

The progressive development of the shear cracks illustrated in Fig.6.29 is in fracture mechanics terminology by Mode III into the specimen. The continuation in crack growth in this case is because the higher push-pull stress amplitude is of sufficient magnitude to promote a change in crack orientation favourable for the Stage I (push-pull) to Stage II (torsion) transition.

Fig. 6.31 shows a Stage II crack that has branched considerably as the Stage II crack penetrates the material which is different from the surface Stage II crack path which exhibited coalescence with Stage I microcracks (see Fig. 6.25).
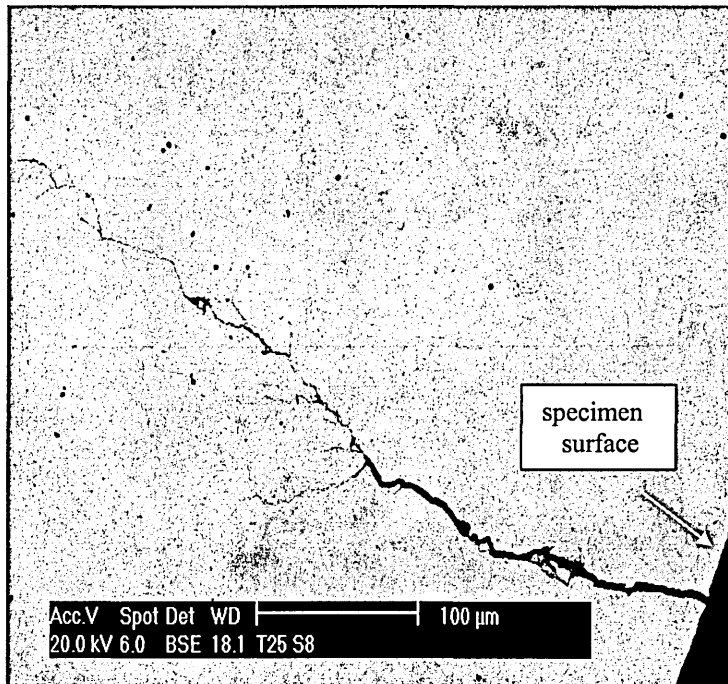

Fig. 6.31 Stage II crack showing microcrack branching in the material

$(0.33 \ [n/N_{f(t)}] \ _{410\,MPa} - 0.04 \ [n/N_{f(p-p)}] \ _{820\,MPa} - [n/N_{f(t)}] \ _{410\,MPa} \rightarrow)$

The microcrack branching from the Stage II crack into the material as illustrated in Fig. 6.31, could be caused by the increasing stress concentration at the crack tip with crack depth and or weak microstructural features that enables subsidiary cracks to propagate from the main crack as it advanced. However, the microcrack branching in this case may not have had any significant effect on crack retardation since the branched cracks are relatively small. It is worth noting that the cumulative lifetime for this specimen was Σ n/Nf = 0.67.

6.7.4 Fractography

Micrographs were taken of the fracture surface of a specimen that was subjected to multiphase loading i.e. torsion - push-pull - torsion sequential loading. The fracture surface cannot usually provide any indication of crack initiation sites under torsion loading, due to frictional contact of the fracture surfaces during cycling. This is evident from the micrograph of the fracture face of a specimen subjected to multiphase loading as shown in Fig. 6.32. It can be seen in Fig. 6.32 that some oxidation of the fracture surface is apparent, which is reflected by the area of the micrograph that appears to have some blurring of the image. This surface texture is attributed to the frictional damage process as a result of the shear mechanism of the reversed torsion loading and the high resilient closure forces of the material at the early stages of crack propagation.

specimen
axis
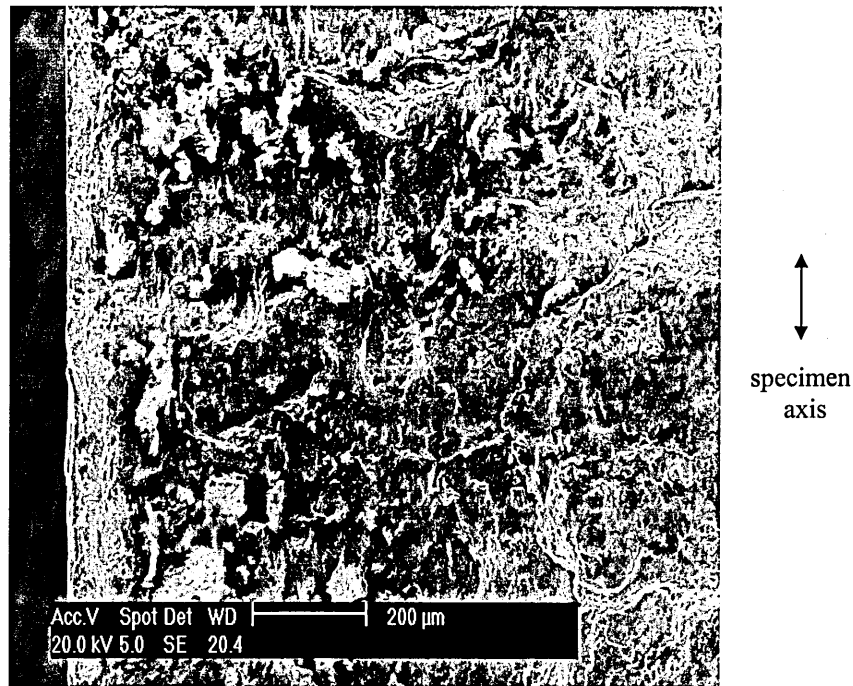
Fig. 6.32 Oxidation on the fracture surface by the shear mechanism of the torsion

loading and material closure effects

$(0.73 \, [n/N_{f\,(t)}]_{410\,MPa} - 0.04 \, [n/N_{f\,(p\text{-}p)}]_{760\,MPa} - [n/N_{f\,(t)}]_{410\,MPa} \rightarrow)$

The Stage I and Stage II crack growth process in fracture mechanics terminology -

Mode II and Mode III shear and Mode I tensile, modes of fracture are shown in Fig

6.33. It can also be seen in Fig, 6.33 that the specimen failed in the latter stages by

the continuation of the Stage II crack, which grew along planes of 45° and 135° to the

longitudinal or transverse directions, consistent with the planes exhibiting the

maximum normal stress amplitude.

This crack growth pattern was found to be similar for all the specimens that were

taken to complete failure.
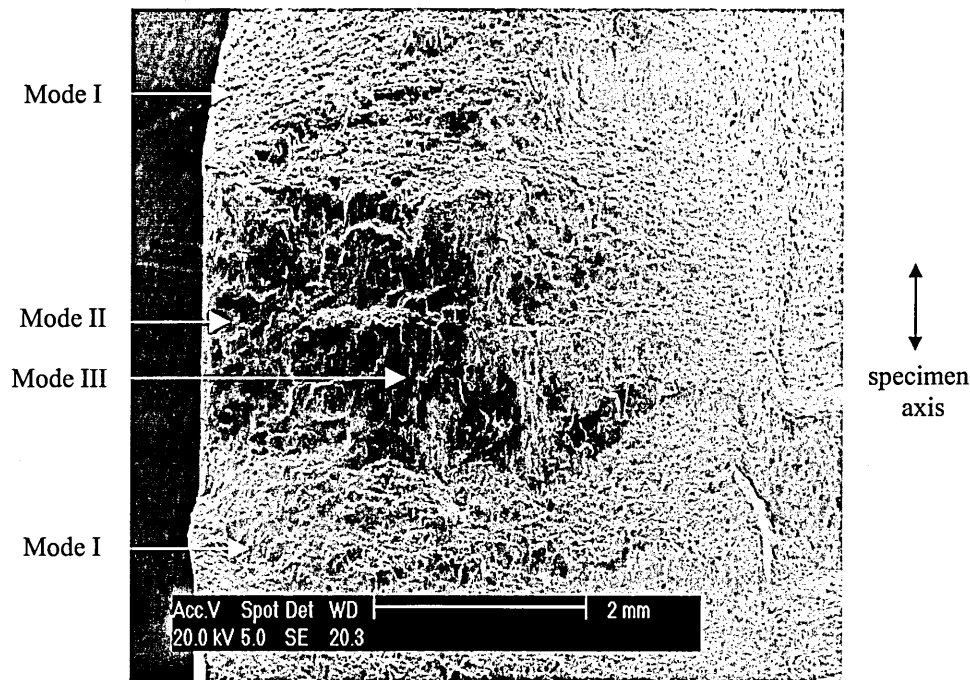
Fig. 6.33 Fracture surface of a specimen subjected to multi-phase loading

$(0.73 \, [n/N_{f(t)}] \, _{410 \, MPa} - 0.04 \, [n/N_{f(p-p)}] \, _{760 \, MPa} - [n/N_{f(t)}] \, _{410 \, MPa} \rightarrow)$

Although the crack growth pattern shown in Fig. 6.33 was found to be consistent for all the specimens that were taken to complete failure, fatigue crack growth in torsion has however, been reported [126] to exhibit no transition to Stage II crack growth. Where for this case [126] crack growth in fracture mechanics terms was reportedly by Mode II along the specimen surface and by Mode III into the specimen. Although this crack growth pattern was for the material BS 970 605H32 (EN16) which had been heat-treated to obtain a martensitic microstructure.

Chapter 7

Conclusions

1. The introduction of a push-pull load interruption significantly affected the torsion fatigue life of 0.42% carbon steel. The fatigue life was increased or decreased depending on the magnitude of the push-pull load interruption and the prior torsion cycle ratio. For the higher interruption stress ranges ($\Delta\sigma$ 760 and 820 MPa) the torsion fatigue lifetime was reduced and conversely for the lower interruption stress ranges ($\Delta\sigma$ 600 and 640 MPa) the torsion fatigue lifetime was enhanced.

2. The reduction or enhancement of the torsion fatigue lifetime was considered to be attributable to crack interaction as a result of the push-pull load interruption. The decrease in fatigue lifetime is attributed to the generation of push-pull Stage I cracks under the higher interrupted stress amplitudes. Since Stage I crack planes for push-pull are complimentary to torsion Stage II cracks and the introduction of the push-pull load interruption can lead to the early transition and the formation of a dominant crack. The increase in fatigue life is probably due to a blocking effect of the torsion Stage I cracks by localised microstructural changes i.e. unfavourable crystallographic slip band formation in the grains ahead of Stage I cracks.

3. The Palmgren-Miner linear damage rule could not account adequately for the multi-phase loading sequences used in this work, even though the push-pull load

interruption only represented 4% damage according to the LDR. This highlighted the inadequacy of the LDR to account for crack-load interactions that result in interrupted crack growth under this non-proportional multi-phase loading.

4. Fatigue failure of the specimens used for the multi-phase loading tests produced dominant fatigue crack paths similar to that of those specimens subjected to pure torsion fatigue. For this type of loading the length of the Stage I crack at the transition tends to increase as the prior torsion cycle ratio ($n/N_{f(t)}$) is increased.

5. The fatigue cracks observed on the surface of the specimens subjected to pure torsion loading showed that the density Stage I cracks increased as the torsion cycle ratio increased from 0.22 $n/N_{f(t)}$ to 0.53$n/N_{f(t)}$. The crack density reached saturation as the cycle ratio approached 0.53 $n/N_{f(t)}$. However, as the cycle ratio approached 0.73$n/N_{f(t)}$ the crack density appeared to decrease with the coalescence of Stage I cracks.

6. Longer and less populated network of Stage I cracks were observed with the introduction of the higher push-pull interruptions. Whereas shorter and greater number of Stage I cracks were observed for the lower push-pull load interruption.

7. A crack growth model was proposed that reflected the physical characteristics of Stage I and Stage II crack growth based on the MSC and PSC growth equations of the form,

for MSC growth (Stage I)

$$da/dN = C_m(d_i - a)$$

and for PSC growth (Stage II)

$$da/dN = C_p \, a \, -D$$

where C_m and C_p are stress state dependent, d_i is a microstructural barrier length, D is a material constant and a is crack length.

The model parameters were obtained using torsion constant amplitude S-N fatigue data for 0.42% carbon steel. The crack growth model developed was used to predict uniaxial constant amplitude fatigue lifetimes. The accuracy of the torsion predictions ranged from $\approx$ 2-17% error, and for push-pull $\approx$ 7-57% error. It should be noted that the model was derived using limited fatigue data and it is thought that the accuracy could have been improved if more data had been used. Also generally higher error is expected at or near the fatigue limit, which may reconcile the highest percentage error predicted for the push-pull loading.

8. The crack growth model gave non-conservative predictions for the higher push-pull load interruptions, where uninterrupted crack growth was evident. However for the lower push-pull load interruptions the model considerably underestimated the fatigue lifetime. This was because the model did not account for any crack-load interaction that could affect interrupted crack growth.

9. The microstructural parameter d_i used in model for MSC growth was taken as mean of the ferrite grain sizes obtained from statistical analysis of the microstructure for the 0.42% carbon steel. This approach was found to work well since the model predictions for constant amplitude loading were in good agreement with the experimental fatigue lifetime results. Furthermore since torsion Stage I cracks were observed to initiate and propagate in ferrite grains, this also justified the principle of the method used for the determination of the parameter d_i.

References

[1] Braithwaite F., 1854, On fatigue and consequent fracture of metals, Ints. Civil Engrs., Proc., Vol. 2, pp 463-474

[2] Schutz W, 1996, A history of fatigue, Engng. Fracture Mech. Vol. 54, No. 2, pp 263-300

[3] Albert W.A.J., 1838, Uber Treibseile am Harz. Archive fur Mineralogie, Geognosie, Bergbau und Huttenkunde,10, pp 215-34

[4] First Report Safe Manriding in Mines, HSE, 1976, Introduction, Pub.HMSO

[5] Professional Engineering Magazine, IMech.E., 2000, Vol. 13, No. 21, p 7

[6] Miller K.J., Proc. Inst. Mech. Eng. ,1991, Vol. 205, pp 291-304

[7] Kitagawa H., Yuuki R., Tohgo K. and Tanabe M., 1982, ΔK-Dependency of fatigue crack growth of single and mixed mode cracks under biaxial stress, ASTM STP 853, pp 164-183

[8] Brown M.W., 1989, Multiaxial fatigue failure, Advances in Fatigue Science and Technology, (Eds.), C. Moura Branco and L. Guerra Rosa, Pub, Kluwer Academic, pp 339-361

[9] Diboine A., Fatigue assessment of components under complex loadings, Fourth International Conference on Biaxial/Multiaxial Fatigue, St Germain en Laye (France), Vol. 1, pp 93-109

[10] Briggs G.A.D., de los Rios E.R. and Miller K.J., How to observe short surface cracks by acoustic microscopy, The Behaviour of Short Fatigue Cracks, Eds. K.J.Miller and E.R.de los Rios, EGF 1, Mech. Eng. Pub. Ltd London, pp 539-535

[11] De Lange R.G. 1664, Plastic replica method applied to a study of fatigue crack propagation in steel 35CD4 and 26 SE aluminium alloy, Trans. AIME, 230 pp 644-648

[12] Lowis J.M. and Fearnehough G.D., 1971, The detection of slow crack growth in crack opening displacement specimens using an electrical potential method, Engng Fracture Mech.,3, pp 103-108

[13] Berkovits A. and Fang D., 1995, Study of fatigue characteristics by acoustic emission, Engng, Fracture Mech. Vol. 3, pp 401-416

[14] Haworth W.L., Singh V. K. and Mueller R.K., 1977, Fatigue damage detection in 2024-T3 aluminium, titanium and low carbon steel by optical correlation, J. Engng. Mater. Technol. Trans. ASME, Series H, 99, 319

[15] Baxter W.J., 1979, Exoelectron measurements of the rate of development of fatigue, Fatigue Engng. Mater. Struct. Vol. 1, pp 343-

[16] Fisher B.C. and Sherrat F., 1973, Random load fatigue damage accumulation in mild steel, Proc. Inst. Mech. Engrs. 187, 285

[17] Doquet V., 1997, Crack initiation mechanisms in torsional fatigue, Fatigue Fract. Engng. Mater. Struct. Vol. 20, No. 2, pp 227-235

[18] Forsyth P.J.E., 1969, The Physical Basis of Metal Fatigue, Blackie

[19] de los Rios E. R., Tang Z. and Miller K. J., 1983, Short crack fatigue behaviour in a medium carbon steel, Fatigue Engng. Mater. Struct. Vol. 7, pp 97-108

[20] Frost N.E., Marsh K.J. and Pook L.P., Metal Fatigue, Clarenden Press, Oxford

[21] Smallman R.E., 1980, Modern Physical Metallurgy, Third Edition, Butterworths London, pp 201-212

[22] Thompson N., Wadsworth N. J. and Louat N., 1956, The Origin of Fatigue Fracture in Copper. Phil. Mag.,Vol. 1, pp 113-126

[23] Neumann P. and Tonnessen., 1987, Cyclic deformation and crack initiation, Fatigue 87, Vol. 1, Editors Richie and Starke. EMAS, pp 3-22

[24] Lankford J. 1976 Inclusion-matrix debonding and fatigue crack initiation in low alloy steels. Int. J. Fract., 12, pp 155-157

[25] Kunnio J., Shimizu M., Yamanda K., Sakura K. and Yamamoto J. 1981., The early stage of fatigue crack growth in martensitic steel, Int. J. Fract., 17, pp 111-119

[26] Murtaza G. and Akid R., 1995, Modelling short fatigue crack growth in a heat-treated low-alloy steel, Fatigue Engng. Mater. Struct. Vol. 17, pp 207-214

[27] Morris W.L., James M.R. and Buck O. 1980 Computer simulation of fatigue crack initiation. Engng. Fract. Mech., Vol. 13, pp 213-221

[28] Kompek G., Matzer F.E. and Maurer K.L., 1982, Crack initiation and crack propagation by torsional fatigue in low carbon steel, Fracture and role of microstructure, Eds. K.J. Maurer and F.E.Matzer, EMMAS, Vol.2, pp 398-406

[29] Brown M. J. and Miller K.J.,1979, Initiation and Growth of Cracks in Biaxial Fatigue, Fatigue of Engineering Materials and Structures, 1, pp 231-246

[30] Miller K.J., Mohamed H. J. and de los Rios E. R., 1986, Fatigue damage accumulation above and below the fatigue, The Behaviour of Short Fatigue Cracks, Eds. K.J.Miller and E.R.de los Rios, EGF 1, Mech. Eng. Pub. Ltd London, pp 491-511

[31] Radhadakrishman V.M. and Mutoh Y, 1986, On fatigue crack growth in Stage I, The Behaviour of Short Fatigue Cracks, Eds. K.J.Miller and E.R.de los Rios, EGF 1, Mech. Eng. Pub. Ltd London, pp 87-99

[32] Miller K.J. and O'Donnell W.J., 1999, The fatigue limit and its elimination, Fatigue Engng. Mater. Struct. Vol. 22, pp 545-557

[33] Miller K. J. The Two Thresholds Of Fatigue Behaviour, 1993, Fatigue Fract. Engng. Mater. Struct. Vol. 16, No 9, pp 93-939.

[34] Suresh S., 1991, Fatigue of Materials, Cambridge University Press

[35] Forsyth P.J.E. and Ryder D.A., 1960, Aircr. Engng. 32, 96

[36] Socie D., 1991, Critical plane approach for multiaxial fatigue damage assessment, ASTM Syposium on Multiaxial Fatigue

[37] McDowell D.L., 1997, An engineering model for the propagation of small fatigue cracks in fatigue, Engng. Frac. Mech. Vol. 56, No 3, pp 357-377

[38] Tanaka K., Akiniwa Y., Nakai Y. and Wei R.P., 1986, Modelling of Small Fatigue crack growth interacting with grain boundary, Engng. Frac. Mech., Vol. 24, No. 6, pp 803-819

[39] Brown M.W. and Miller K.J. 1973, A theory for fatigue failure under multiaxial stress strain conditions, Proc. IMechE; 187, pp 745-755

[40] Fatemi A. and Socie D.F., 1987, A critical plane approach to multiaxial fatigue damage including out-of-phase loading, Fatigue Fract. Engng. Mater. Struct. Vol. 11, No. 3, pp 429-446

[41] Gough H.J. and Pollard H.V., 1935, The strength of metals under combined alternating stress, Proc. Inst.Mech. Engrs.,131 (3), pp 3-54

[42] McDowell D.L., 1996, Basic issues in the mechanics of high cycle metal fatigue, Int. J. of Fracture, 80, pp 149-165

[43] Guest J.J., 1943, The problem of combined stress , Engineering, London. ..

[44] Stulen F.B. and Cummings H.N., 1954, A failure criterion for multiaxial fatigue stresses, Proc. ASTM 54, pp 822-835

[45] Findley W.N., 1959, A theory for the effect of mean stress on fatigue of metals under combined torsion and axial load or bending, J. of the Engng. Ind., pp 301-306

[46] Krempl E. and Lu H., 1984, The hardening and rate-dependent behaviour of fully annealed AISI type 304 stainless steel under in-phase and out-of-phase strain cycling at room temperature, ASME J. Engnr. Mater. Tech., 106, pp 376-382

[47] Chen X., Gao Q. and Sun X.F., 1994, Damage analysis of low cycle fatigue under nonproportional loading, Int. J. Fatigue, 16, pp 211-215

[48] Gao H. and Fernando U.S., 1994, Effect of non-proportional overload on fatigue life, Fourth International Conference on Biaxial/Multiaxial Fatigue, St Germain en Laye (France), Vol. 1, pp 211-221

[49] Ibrahim M.F.E., 1981 Early damage accumulation in metal fatigue, Ph.D. thesis, University of Sheffield

[50] Zhang W., 1991, Short fatigue crack behaviour under different loading conditions, Ph.D. thesis, University of Sheffield

[51] Brown M.W., Miller K.J., Fernando U.S., 1994,Yates J.R. and Suker D.K., Aspects of Multiaxial fatigue crack growth, Fourth International Conference on Biaxial/Multiaxial Fatigue, St Germain en Laye (France), Vol. 1, pp 3-16

[52] Irwin G.R.,1957, Analysis of stresses and strains near the end of a crack traversing a plate, Journal of Applied Mechanics, 24, pp 361-364

[53] Knott J.F., 1973, Fundamentals of Fracture Mechanics, Butterworth, London

[54] Paris P.C. and Erdogan F., 1963, A critical analysis of crack propagation laws, Journal of Basic Engineering, 85, pp 528-534

[55] Brown M.W., 1988, Aspects of fatigue crack growth, Proc. Instn. Mech. Engrs. Vol. 202, No. C1, pp 19-29

[56] Miller K.J., 1987, The behaviour of short fatigue cracks and their initiation Part II - A general summary, Fatigue Fract. Engng. Mater. Struct. Vol. 10 No. 2, pp 93-113

[57] Tokaji K., Ogawa T., Harada Y. and Ando Z., 1986, Limitations of linear elastic fracture mechanics in respect of small fatigue cracks and microstructure, Fatigue Fract. Engng. Mater. Struct. Vol. 99, No. 1, pp 1-14

[58] Allen R.J. and Sinclair J.C., 1982, The behaviour of short cracks, Fatigue Fract. Engng. Mater. Struct. Vol. 5 No. 4, pp 343-347

[59] Pearson S., 1975, Initiation of fatigue cracks in commercial aluminium alloys and the subsequent propagation of very short cracks, Engng Fract, Mech. 7, pp 235-247

[60] Kitagawa H. and Takahashi S., 1976, Applicability of fracture mechanics to very small cracks or cracks in the early stage, Proceedings of the 2nd International Conference on the behaviour of Materials, Boston, p 627

[61] Miller K.J., 1982, The short crack problem, Fatigue Engng. Mater.. Struct. Vol. 5, No 3, pp 223-232

[62] Newman J.C., Wu X.R., Swain M.H., Zhao W., Phillips E. P. and Ding C.F., 2000, Small-crack growth and fatigue life predictions for high-strength aluminium alloys. part II: crack closure and fatigue analyses, Fatigue Fract. Engng. Mater. Struct. 23, pp 59-72

[63] del los Rios E.R., Tang Z. and Miller K.R., 1984, Short crack fatigue behaviour in a medium carbon steel, Fatigue Fract. Engng. Mater. Struct. Vol. 7 No. 2, pp 97-108

[64] EL Haddad M.H., Smith K.N. and Topper T.H., 1979, Fatigue crack propagation of short cracks, J. Engng. Mater. Technol. Trans. ASME H, 101, pp 42-46

[65] Morris W.L., James M.R. and Buck O.,1981, Growth rate models for short surface cracks in Al 2219-T851, Metall. Trans., 12A, pp 57-64

[66] Morris W.L., 1980, The non-continuum crack tip deformation of surface microcracks, Metall. Trans. 11A, pp 1117-1123

[67] Lankford J., Cook T.S. and Sheldon G.P., 1981, Fatigue crack growth in a nickel-based superalloy, Int. J. Fracture, 17, pp 143-155

[68] Suresh S. and Richie R.O., 1984, The propagation of short fatigue cracks. Int. Met. Rev. 29, pp 445-476

[69] Brown W.F. and Strawley J.E., 1966 Plain strain crack testing of high metallic materials, ASTM, S.T.P. 410

[70] Kitagawa H. and Takahashi S., 1976, Applicability of fracture mechanics to very small cracks at the cracks in the early stage, Proc. 2nd Int. Conf. Mech. Behaviour of Materials, Boston, pp 627-631

[71] Miller K.J., 1985, Initiation and growth rates of short fatigue cracks. IUTAM Eshelby Memorial Symposium. Fundamentals of Deformation and Fracture (Edited by Bilby B.A., Miller K.J. and Willis J.R.) Cambridge University Press, pp 477-500

[72] Duggan T. V. and Byrne J., 1977, Fatigue as a Design Criteria, The MacMillan Press, London

[73] Miller K.J., Mohamed H.J., Brown W.M. and del los Rios E.R., 1986, Barriers to short fatigue crack propagation at low stress amplitudes in a banded ferrite-pearlite structure, Small Fatigue Cracks, Edited by Ritchie R.O. and Lankford J., The Metallurgical Society, pp 639-656

[74] Taylor D., 1986, Fatigue of short cracks: the limitations of fracture mechanics, The Behaviour of Short Fatigue Cracks, Eds. K.J.Miller and E.R.de los Rios, EGF 1, Mech. Eng. Pub. Ltd London, pp 479-490

[75] Taylor D. and Knott J.F., 1981, The fatigue crack propagation behaviour of short cracks; the effect of microstructure, Fatigue Fract. Engng. Mater. Struct.4, pp 147

[76] James M. R. and Morris W. L., 1983. Effect of fracture surface roughness on growth of short fatigue cracks, Met. Trans. 14A, 153

[77] del los Rios E.R., Mohamed H.J., and Miller K.J., 1985, A micro-mechanics analysis for short fatigue crack growth, Fatigue Fract. Engng. Mater. Struct. Vol. 8, No. 1, pp 49-63

[78] Hong Y., Qiao Y. and Zheng X., 1998, The effect of grain size on collected damage of short cracks and fatigue life estimation for a stainless steel, Fatigue Fract. Engng. Mater. Struct. 21, pp 1317-1325

[79] Kage M., Miller K.J. and Smith R.A., 1992, Fatigue crack initiation and propagation in a low-carbon steel of two different grain sizes, Fatigue Fract. Engng. Mater. Struct. Vol.15, No.8, pp 763-774

[80] Chan K., Lankford J. And Davidson D., 1986, A comparison crack-tip field parameters for large and small fatigue cracks, Basic Questions in Fatigue Vol. 1. ASTM STP 924, Editors J.T. Fong and R.T. Fields, pp 206-213

[81] Tanaka K., 1987, Short-crack fracture mechanics in fatigue conditions, in Current Research on Fatigue Cracks, Editors T.Tanaka, M.Jono and K. Komai. Vol.1., Pub. Elsevier, pp 93-117

[82] Polak J. and Liskutin P., 1990, Neucleation and short crack growth in fatigued polycrystalline copper, Fatigue Fract. Engng. Mater. Struct. 13, pp 119-133

[83] Hyspecky P. and Strnadel B., 1992, Conversion of short fatigue cracks into a long crack, Fatigue Fract. Engng. Mater. Struct. Vol.15, No 9, pp 845-854

[84] Hong Y.S. Lu Y.H. and Zheng, 1991, Orientation preference and factual character of short fatigue cracks in a weld metal, J. Mater. Sci., 26, pp 1821-1826

[85] Beretta S. and Clerici P., 1996, Microcrack propagation and microstructural parameters of fatigue damage, Fatigue Fract. Engng. Mater. Struct. Vol. 19, No. 9, pp 845-854

[86] Nisitani H. and Goto M., 1986, A small-crack growth law and its application to the evaluation of fatigue life, The Behaviour of Short Fatigue Cracks, Eds. K.J.Miller and E.R.de los Rios, EGF 1, Mech. Eng. Pub. Ltd London, pp 461-478

[87] Skelton R.P., 1982, Growth of short fatigue cracks during high strain fatigue and thermal cycling, ASTM STP 770, pp 337-381

[88] Ibrahim M.F.E. and Miller K.J., 1980, Determination of fatigue crack initiation life, Fatigue Fract. Engng. Mater. Struct. Vol. 2, No., pp 351-360

[89] Hunter M.S. and Frick W.M.G., 1956, Fatigue crack propagation in aluminium alloy, Pro. ASTM, 56 pp 1038-1046

[90] Bilby B.A., Cottrell A.H. and Swinden K.H., 1963, The spread of plastic yield from a notch, Proc. R. Soc., Lond. A272, pp 304-314

[91] Weeterman J., 1966, Rate of growth of fatigue cracks calculated from the theory of infinitesimal dislocations distributed on a plane. Int. J. Fract. Mech., 2, pp 460-467

[92] Cox B.N. and Morris W.L., 1987, Model-based statistical analysis of short fatigue crack growth in Ti 6Al-2Sn-4Zr-6Mo, Fatigue Fract. Engng. Mater. Struct. Vol. 10, No. 6, pp 429-446

[93] Hobson P.D. 1986, The growth of short fatigue cracks in a medium carbon steel, Ph.D. thesis, University of Sheffield

[94] Hobson P.D., 1982 The formulation of a crack growth equation for short cracks, Fatigue Fract. Engng. Mater. Struct. Vol. 5, No. 4, pp 323-327

[95] Lankford J., 1982, The growth of small fatigue cracks in 7075-T6 aluminium, Fatigue Fract. Engng. Mater. Struct. Vol. 5, No. 3. , pp 233-248

[96] Carbonell P. and Brown M.W., 1985, A study of short fatigue crack growth in torsional low cycle fatigue for a medium carbon steel, Fatigue Fract. Engng. Mater. Struct. Vol. 9, No. 1. , pp 15-23

[97] Hobson P.D., Brown M.W. and del los Rios E.R., 1986, Two phases of short crack growth in a medium carbon steel, The Behaviour of Short Fatigue Cracks, Eds. K.J.Miller and E.R.de los Rios, EGF 1, Mech. Eng. Pub. Ltd London, pp 479-490

[98] Murtaza G. and Akid R., 1995, Modelling of short fatigue crack growth in a heat-treated low alloy steel, Int. J. Fatigue Vol. 17 No. 3, pp 207-214

[99] Blom A.F., Hedlund A., Zhao W., Fathulla A., Weiss B. and Stickler R., 1986, Short fatigue crack growth behaviour in Al 2024 and Al 7475, The Behaviour of Short Fatigue Cracks, Eds. K.J.Miller and E.R.de los Rios, EGF 1, Mech. Eng. Pub. Ltd London, pp 37-66

[100] Klesnil M. and Lukas P., 1972, Eng. Fract. Mech., 4, pp 77

[101] Palmgren A. 1924, Endurance of ball bearings, Z.Verdt. Ing. Die Lebensdauer von Kugellagern. Verfahrenstechinik, Berlin, vol. 68, pp 339-341.

[102] French H. J. 1933, Fatigue and hardening of steels. Transactions , American Society of Steel Treatment, 21, 899-946.

[103] Langer B.F.1937, Fatigue failure from stress cycles of varying amplitude. ASME Journal of Applied Mechanics, 59, A160-A162.

[104] Miner M.A. 1945 Cumulative damage in fatigue , J. Áppl. Mech., Vol. 12, pp A159-A164

[105] Miller K.J. and Ibrahim M.F.E. 1981, Damage accumulation during initiation and short crack growth regimes, Fatigue of Engineering Materials and Structures, Vol. 4, No. 3, pp 263-277

[106] Ibrahim M.F.E. 1981, Early damage accumulation in metal fatigue, Ph.D. thesis, University of Sheffield

[107] Fatemi A. and Yang L. Cumulative fatigue damage and life prediction theories: a survey of the state of the art for homogeneous materials, 1998, Int. J. Fatigue Vol. 20, No 1. pp 9-34. Elsevier Science Ltd.

[108] Miller K. J. 1970, An experimental linear cumulative-damage law. J. Strain Analysis, Vol. 5 , No 3, pp 177-184

[109] Manson S.S. and Halford G.R. 1986 Re-examination of cumulative fatigue damage analysis - an engineering perspective. Engng. Fract. Mech., Vol. 25, pp 539-571

[110] Thang B.Q., Dubuc J., Bazergui A. and Biron A., 1971, Cumulative fatigue damage under strain controlled conditions, J. of Materials, JMLSA 6, pp 718-737

[111] Hashim Z. and Rotem A. 1978, A cumulative damage theory of fatigue failure, Materials Sci. Engng. 34, p147

[112] Hashim Z. and Laird C., 1980, Cumulative damage under two level cycling: Some theoretical predictions an test data, Fatigue Engng. Mater. Struct. 2, 345

[113] Manson S.S., Freche J.C. and Ensign C.R. 1967, Application of a double linear damage rule to cumulative fatigue. ASTM STP 415, pp 384-412

[114] Grover H. J. 1960, Fatigue of aircraft structures , ASTM STP 274, pp 120-124

[115] Wheeler O. E., 1972, Spectrum loading and crack growth, J. of Basic Engng. 94, 181-186

[116] Willenborg J. Engle R.M. and Wood H., 1971, A crack growth retardation model using an effective stress intensity concept. Tech. Rep. TFR 71-701. Los Angeleles: North American Rockwell

[117] Hudak S. J., Davidson D. L., Chan K. S., Howland A. C. and Walsch M. J. 1988, Growth of small fatigue cracks in aeroengine disc materials, Report no. AFWAL-TR-88-4090, Dayton: Air Force Wright Aeronautical Laboratories

[118] Cowles B., 1996, High cycle fatigue in aircraft turbines-an industry perspective, Int. J. Fract.80, pp 147-163

[119] Miller K.J. and Zachariah K.p., 1977, Cumulative damage laws for fatigue crack initiation and Stage I propagation, J. Strain Anal., 12, 262

[120] Miller K.J. and Ibrahim M.F.E., 1981, Damage accumulation during initiation and short crack growth regimes, Fatigue Fract. Engng. Mater. Struct. Vol. 4, No. 3, pp 263-277

[121] Miller K. J. Mohamed H. J. and de los Rios E. R., 1986, Fatigue damage accumulation above and below the fatigue limit, Ed. Miller K. R. and de los Rios E. R., EGF Pub.1, pp 491-511

[122] Fernando U.S., 1987, A new multiaxial testing facility, Ph.D. Thesis, University of Sheffield

[123] Brown M.W, 1975, High temperature multiaxial fatigue, Ph.D.. thesis, University of Cambridge

[126] Hurd N.J. and Irving P.E., 1985, Smooth specimens fatigue lives and microcrack growth in torsion, Multiaxial fatigue, ASTM STP 853, pp 267-284

[127] Williams R.A., Placek R.J., Klufos O., Adams S. L., Gonyea D.C., 1982, Biaxial/torsional fatigue of turbine-generator rotor steels, Multiaxial Fatigue Symposium, San Francisco, ASTM STP 853, pp 441-462

[128] Angelova D. and Akid R., 1998, A note on modelling short fatigue crack behaviour, Fatigue Fract. Engng. Mater. Struct. 21, pp 771-779

[129] Mohamed H.J., 1986, Cumulative fatigue damage under varying stress range conditions, Ph.D. thesis, University of Sheffield

[130] Xin X., 1992, Experimental and theoretical aspects of microstructural sensitive crack growth in Al-Li 8090 alloy, Ph. D. thesis, University of Sheffield

[131] Bilby B. A., Cottrell A. H. and Swinden K.H., 1963, The spread of plastic yield from a notch, Proc. R. Soc. (London), A272, 304

[132] Taira S, Tanaka K. and Nakai Y., 1978, A model of a crack-tip band blocked by grain boundary, Mech. Res. Commun., 5, 375

[133] Navarro A. and de los Rios E.R., 1986, A model for short fatigue crack propagation with an interpretation of the short-long crack transition, Fatigue Fract. Engng. Mater. Struct. Vol 10, No. 2, pp 169-186

[134] Hashin Z. and Laird C., 1980, Cumulative damage under two level cycling: some theoretical predictions and test data, Fatigue Fract. Engng. Mater. Struct. Vol 2, pp 345-350

[135] Shi Z.-F., Wang D.-J. and Xu H., 1992, Two-stage damage cumulative rule, Int. J. Fatigue, 14, No 6, pp 395-398

[136] Socie D., 1987, Multiaxial fatigue damage models, J. Engng. Mater. Technol. Trans. ASME, Vol. 109, pp 293-293

[137] Tokaji K., Ogawa T., and Osako S., 1988, The growth of microstructurally small fatigue cracks in a ferritic-pearlitic steel, Fatigue Fract. Engng. Mater. Struct. Vol. 11, No. 5, pp 331-342

[138] Zhao Y.-X., Gao Q. and Wang J.-N., 1999, Interaction and evolution of short fatigue cracks, Fatigue Fract. Engng. Mater. Struct. 22. pp 459-467

[139] Zhang W. and Miller K.J., 1996, A study of the accumulation of fatigue damage under variable loading-mode conditions, ESIS Conference Proceedings: Short Fatigue Cracks, Sheffield

[140] Goto M., 1994, Statistical investigation of the behaviour of small cracks and fatigue life in carbon steels with different ferrite grain sizes, Fatigue Fract. Engng. Mater. Struct. Vol. 17, No. 6, pp 635-649

[141] Seed G.M. and Murphy G.S., 1997, The applicability of neural networks in modelling the growth of short fatigue cracks, Fatigue Fract. Engng. Mater. Struct. 21, pp 183-190

[142] Bishop. C. M., 1995, Neural Networks for Pattern Recognition, Oxford University Press, Oxford
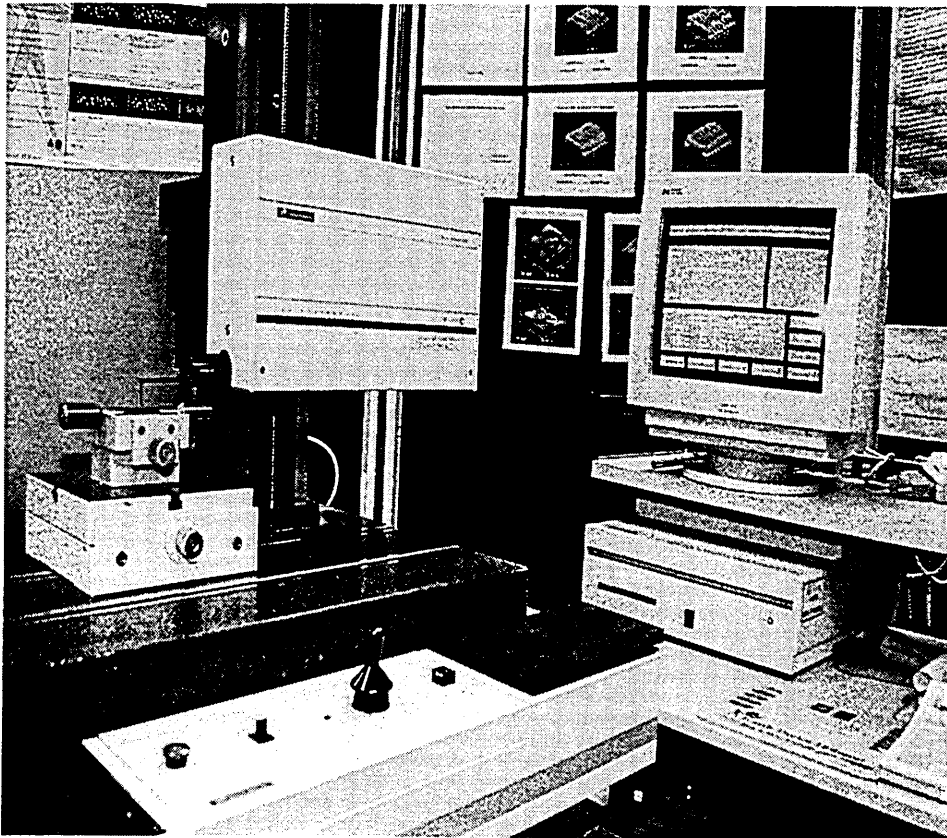
Apendix 1. Taylor Hobson Surface Measuring Machine

Apendix 2. Societe Genovoise MU-214B Universal Measuring Machine

Machine actuator load cell

Diagonal load lines
for torsion loading

Torque plate outline
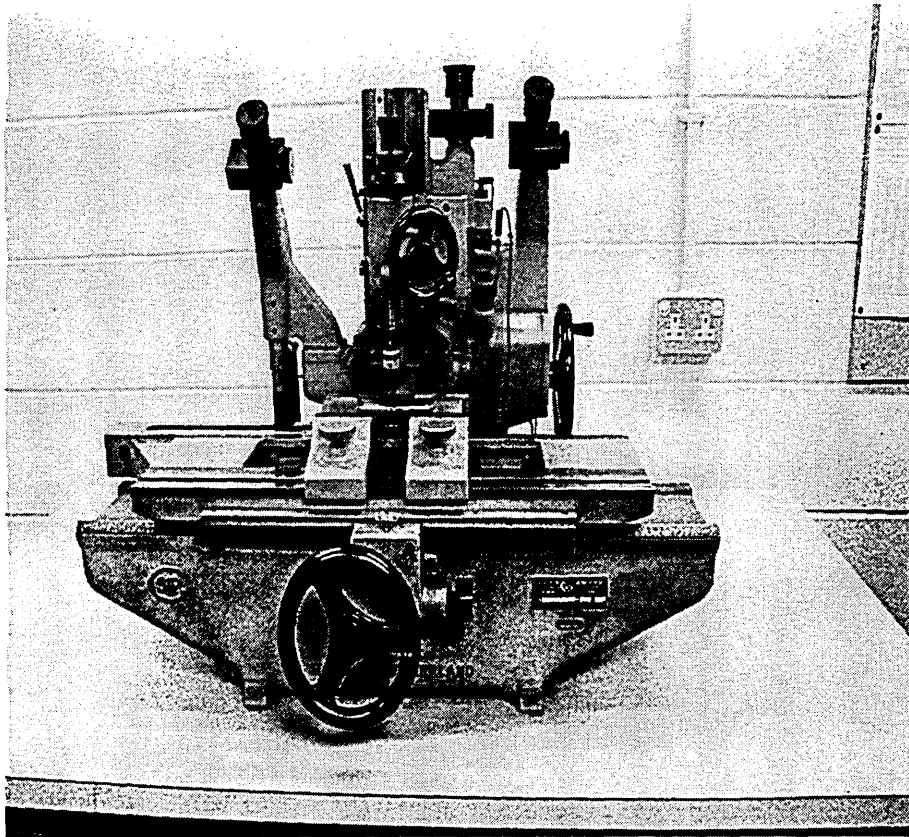
Push-Pull load line
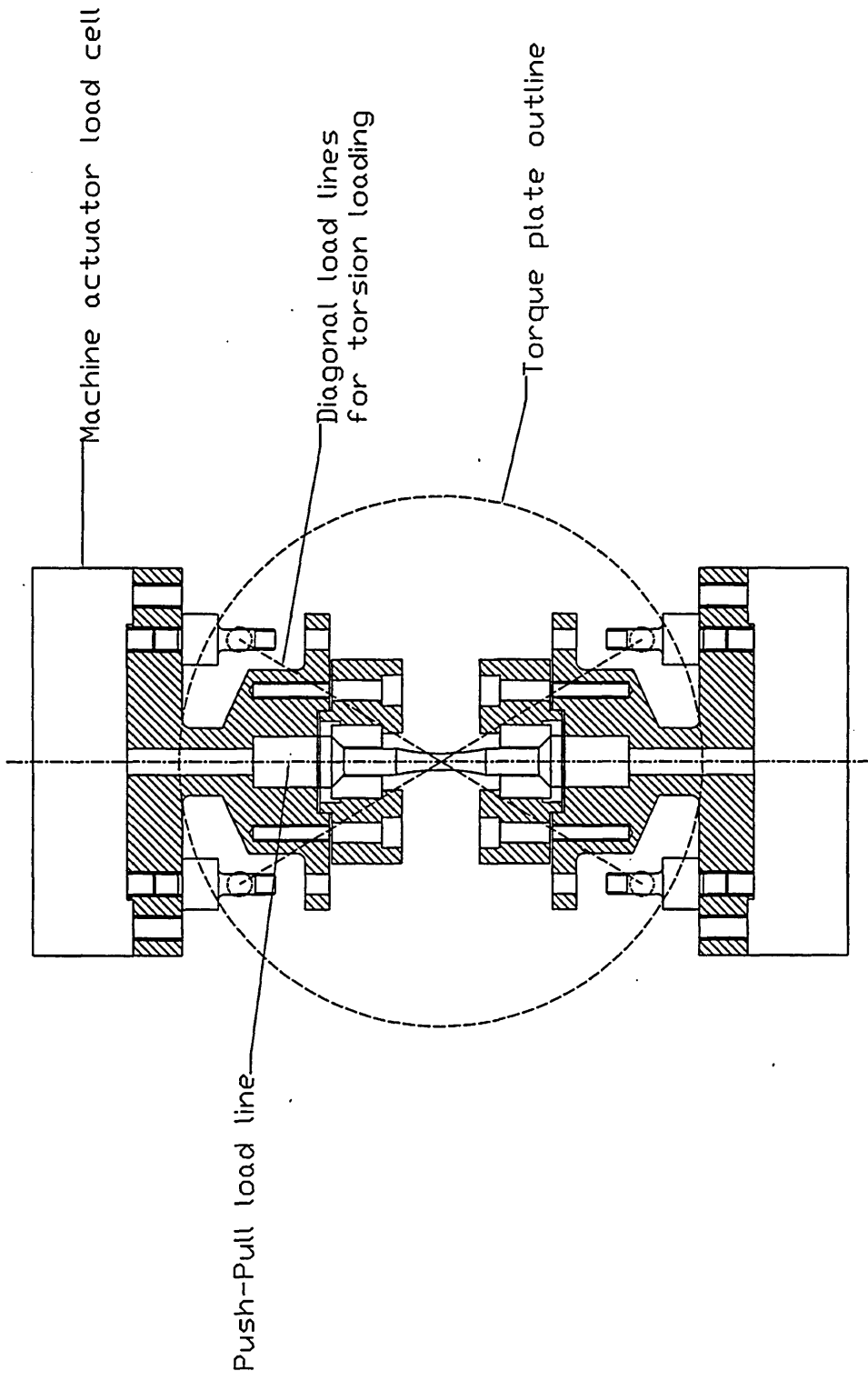
ASSEMBLY OF SPECIMEN AND LOAD LINES

Section Y-Y

15

50

15

Hole drilled 8.5 dia
and threaded M10
× 1.5p I.S.□. metric
coarse, 25 deep

Ground finised bar material

Threaded 10 × 1.5p
I.S.□. metric coarse

131

ø10

73

30

15

ø13

Y

Y

60

30

90

Holes drilled 8.5
dia and threaded
M10 × 1.5p I.S.□.
metric coarse
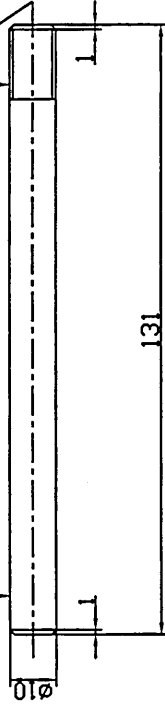
Dimensions in mm
Material − brk. BS 080 M42
Number required − 4 sets

STABILISER BRACKET ASSEMBLY

Section X-X

20

Dimensions in mm
Material BS 080 M42
Number reuired – 4

STABILISER ARM

95

62.4crs

35

15

40

90

60

Φ13

Φ15
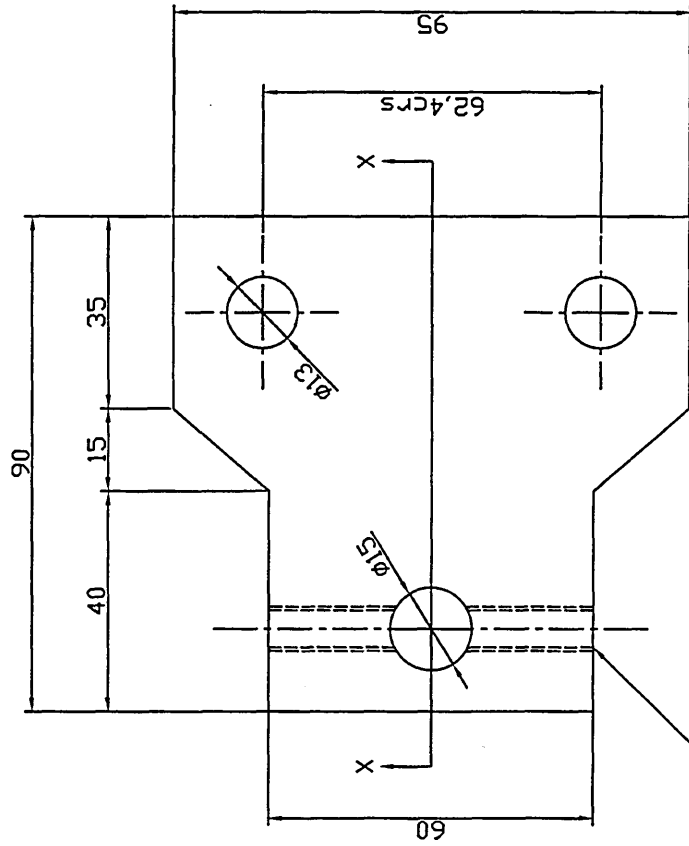
Holes drilled 6.5 dia and
threaded M8 × 1.25p I.S.□.
metric coarse

X

X
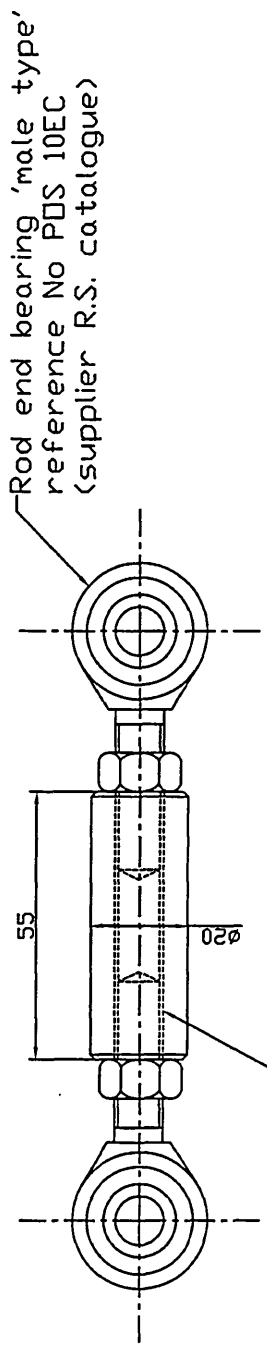
Rod end bearing 'male type'
reference No PDS 10EC
(supplier R.S. catalogue)

Bar drilled 8.5 dia and
threaded M10 x 1.5p
I.S.O. metric coarse

55

ø20

Dimensions in mm
Material – BS 817 M40 'T'

ROD END BEARING TORQUE ARM

Holes threaded M12 x
1.75p I.S.O. metric coarse

Holes drilled through
plate 12 dia

Ø260

120crs

200crs

Section C-C

163crs

Ø135

20.3
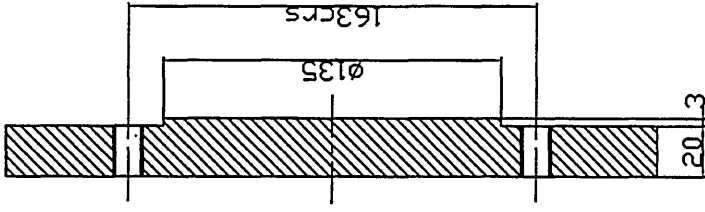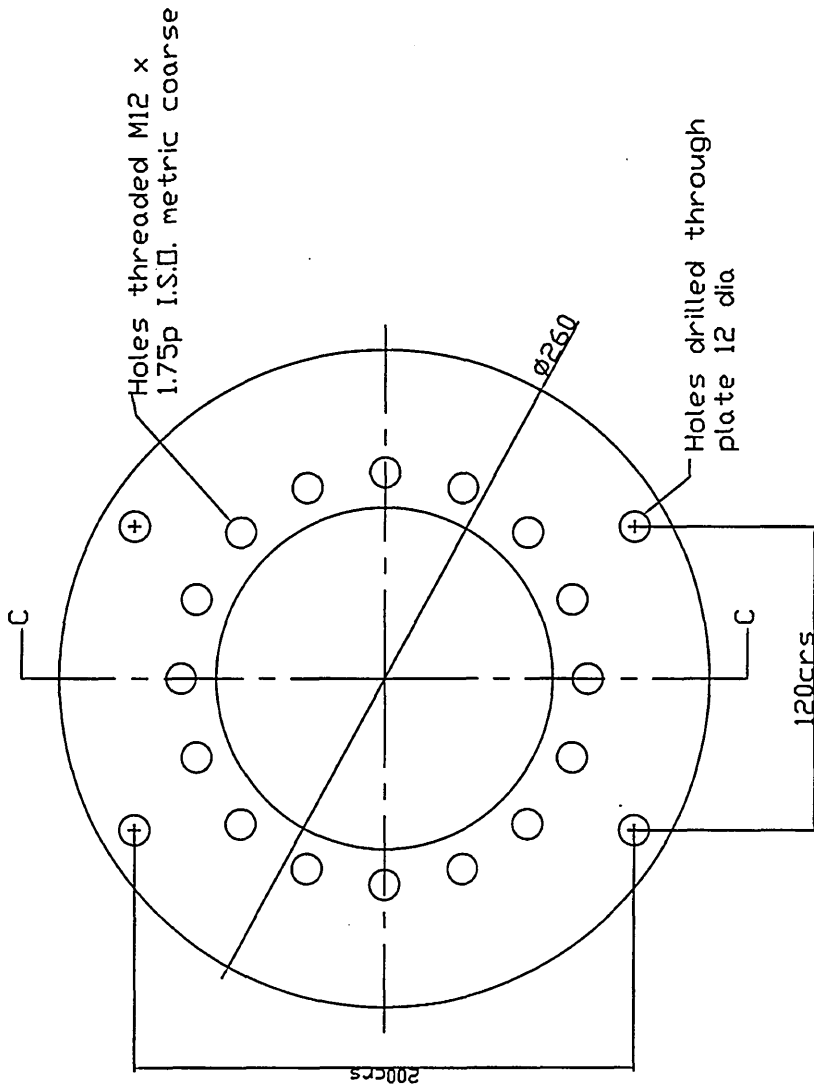
TORQUE PLATE

Dimensions in mm
Material - BS 817 M40 'T'
Number required - 2

TORQUE PIN

90

87

2

Ø10

1

Hole drilled 4.2 dia.,
18 deep and
threaded M5 x 0.8p
I.S.O. metric coarse

Material – BS 830 M31 'V'
Number required – 4

SPLIT RING

Machined split
face

25

Ø36 0-0.015

Ø14

45°
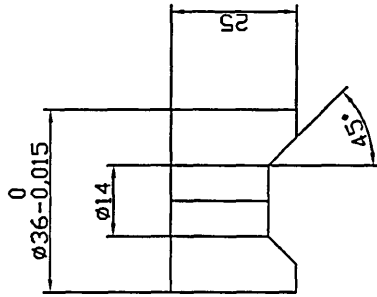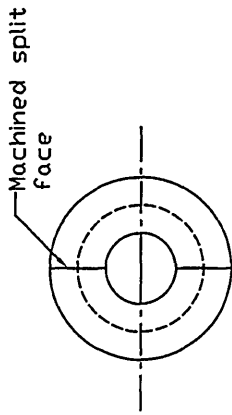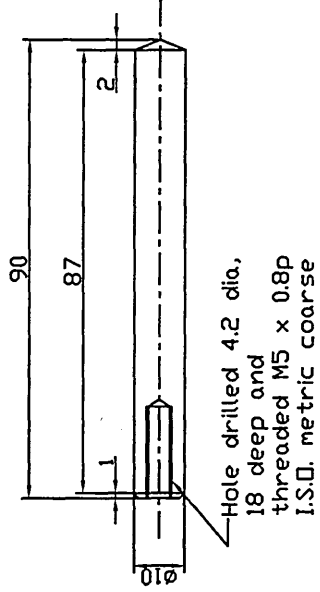
Material – BS 830 M31 'V'
Number required – 2 sets

All dimensions in mm

SPECIMEN HOUSING

Section Y-Y

∅145
∅90
70crs
∅50 +0.000 / -0.000
∅25 +0.020 / +0.000
38
R4
R4
∅13
120crs
∅135
163crs
∅190
33
40
33
24
3
100
12
38
6

Dimensions in mm
Material – BS 817 M40 'T'
Number required – 2 (top and Bottom)

Section X-X
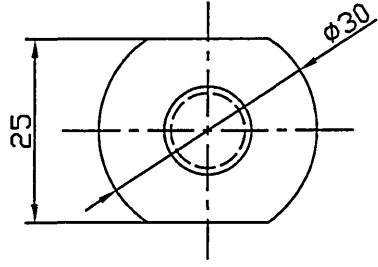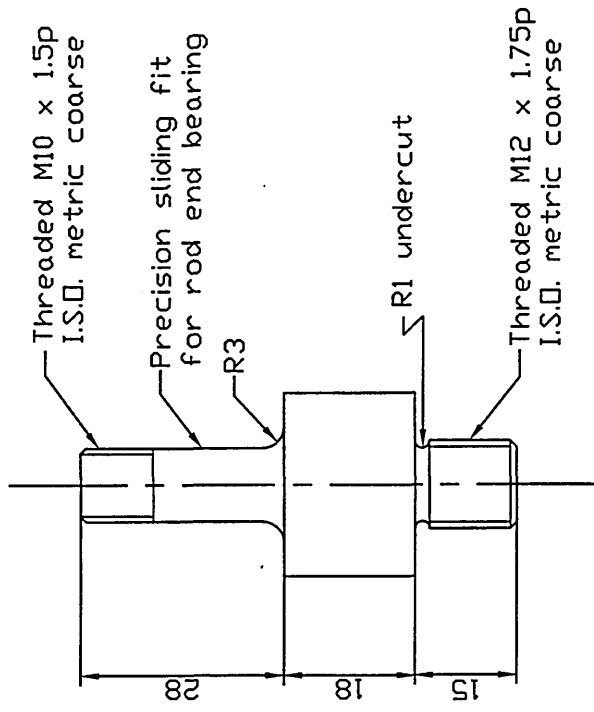
Holes threaded M12 x 1.75p I.S.O. metric coarse

Holes threaded M8 x 1.25p I.S.O. metric coarse

Holes drilled 9.5 and reamed 10

M20 x 2.5p I.S.O. metric coarse thread

24

Ø30

25

Dimensions in mm
Material – BS 817 M40 'T'
Number required – 4

Threaded M10 × 1.5p
I.S.O. metric coarse

Precision sliding fit
for rod end bearing

R3

R1 undercut

Threaded M12 × 1.75p
I.S.O. metric coarse

28

18

15

PIVOT SCREW

Ø100

70crs

Ø28

Ø36
Ø40
Ø50

10

10

41

35

6

Section A-A

Holes counterbored
15 dia, 10 deep

A

A

Holes drilled 10 dia
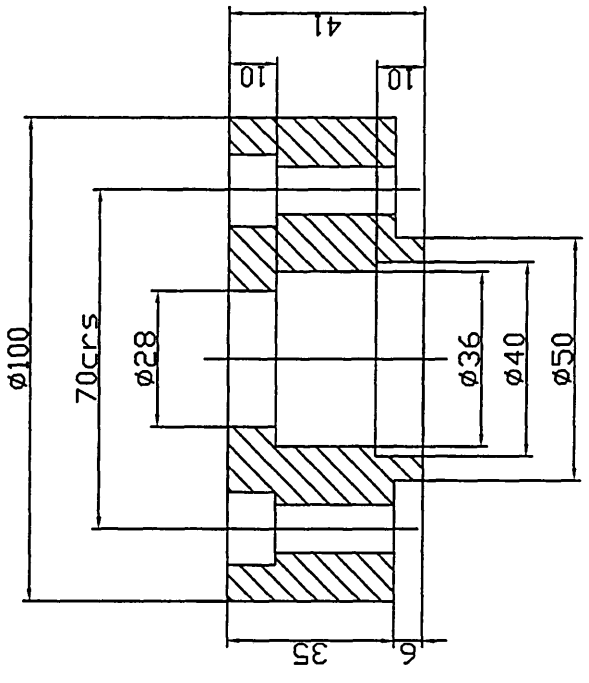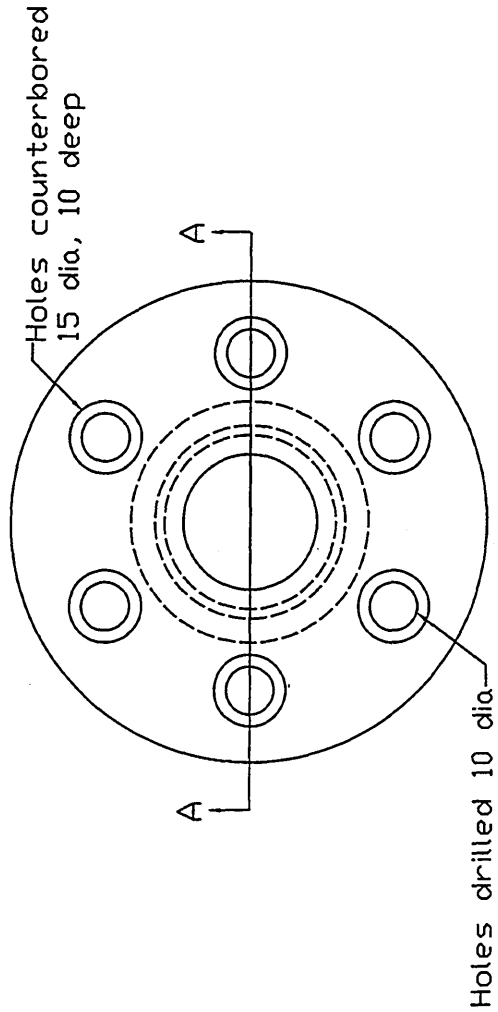
LOAD RING

Dimensions in mm
Material - BS 817 M40 'T'
Number required - 2

Ø32

15

Dimensions in mm
Material – BS 817 M40 'T'
Number required – 4

Through
hole drilled
9.5 and
reamed 10

10

30

2

5

97

R5

65

Threaded M10 × 1.5p
I.S.O. metric coarse

2
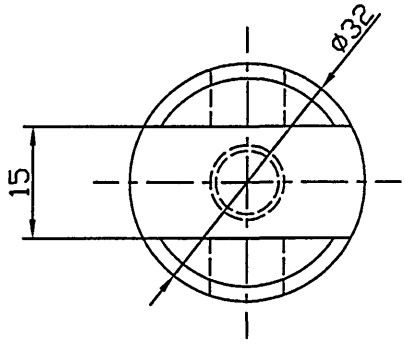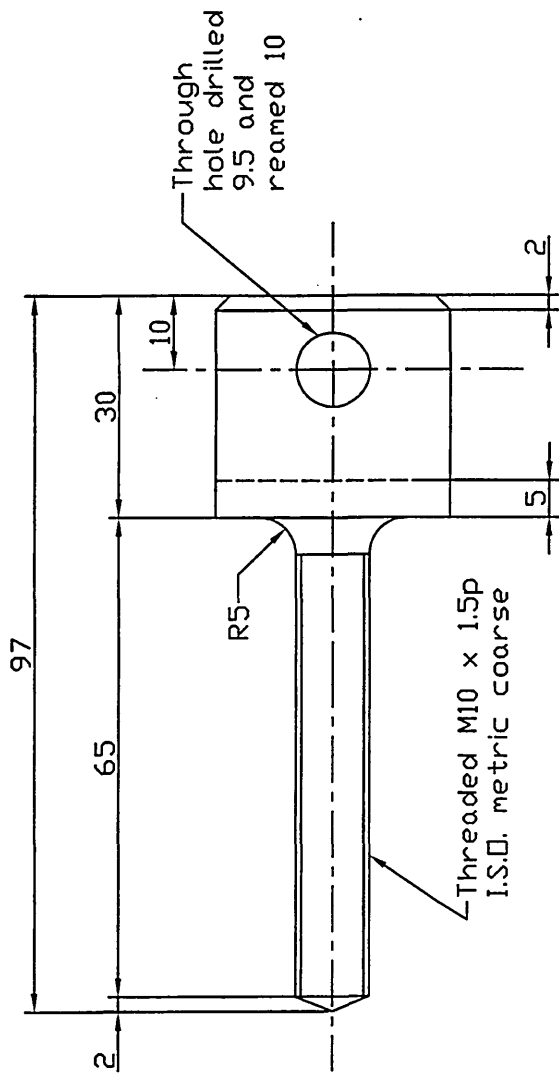
SCREW

The computer program (part) represents crack growth for multi-phase loading (torsion - push-pull - torsion → failure) where crack propagation starts from the onset of fatigue cycling and continues for each of the successive loading regimes.

Computer program notation

n_1 = number of cycles selected - phase 1 loading

n_{s1} = number of cycles for small crack growth for grain 1 - phase 1 loading

n_{s2} = number of cycles for small crack growth for grain 2 - phase 1 loading

n_{sith} = number of cycles for small crack growth for the ....ith grain (from n_{s2} to n_{st})

n_{st} = number of cycles for the transition grain from small to long crack growth

n_{sp} = number of cycles for long crack growth - phase 1

a_{s1} = crack length for grain 1 - phase 1 loading (μm)

a_{s2} = crack length for grain 2 - phase 1 loading (μm)

a_{sith} = crack length for ....ith grain (μm)

a_{st} = crack length for the transition grain (μm)

a_{p1} = crack length for long crack regime (μm)

a_{2s1} = crack length for grain 1 - phase 2 loading (μm)

a_{2s2} = crack length for grain 2 - phase 2 loading (μm)

a_{2sith} = crack length for the ....ith grain (μm)

a_{2p2} = crack length for long crack regime (μm)

n_2 = number of cycles selected - phase 2

I

n_{3s1} = number of cycles for small crack growth for grain 1 - phase 3 loading

n_{3s2} = number of cycles for small crack growth for grain 2 - phase 3 loading

n_{3sith} = number of cycles for small crack growth for the ....ith grain (from n_{3s2} to n_{2st})

n_{3st} = number of cycles for the transitional grain from short to long crack growth

n_{p3} = number of cycles for long crack - phase 3 loading

d = length of grain 1 (μm)

d_m = length of mean grain size (μm)

....

$n_{s1} = IF(a_t < \alpha d, 0, 1/(A*\Delta\tau^\wedge m)*LN((d-d_m)/(d-\alpha*d)))$

$n_{s2} = IF(n_{s1} > 10^\wedge 6, 0,$

$\quad (If (a_t < \alpha*d, 0, 1/(A*\Delta\tau^\wedge m)*LN((d+d_m-\alpha*d)/(d+d_m)-(d+\alpha*d_m)))))$

$n_{sith} = IF(n_{s1} > 10^\wedge 6, 0,$

$\quad IF(a_t < d+d_m+\alpha*d_m, 0, 1/(A*\Delta\tau^\wedge m)*LN((d+2*d_m)-(d+\alpha*d)$

$\quad /(d+2*d_m)-(d+d_m+\alpha*d_m))))*INT((a_t-d-d_m)/d_m)$

$n_{st} = IF(a_t < \alpha*d, 1/(A*\Delta\tau^\wedge m)*LN((d-a_o)/(d-a_t))),$

$\quad IF(a_t < d, 1/(A*\Delta\tau^\wedge m)*LN((d+d_m-\alpha*d)/(d+d-a_t))), 1/(A*\tau^\wedge m)*$

$\quad (LN(((INT((a_t-d)/d_m)*d_m+d+d_m-(INT((a_t-d)d_m)*d_m+d-d_m+\alpha*d_m))$

$\quad /INT((a_t-d)/d_m)*d_m+d+d_m-a_t))))))$

$n_{p1} = IF(a_t >= a_f, 0,$

$$\text{IF}(n_{s1}>10^{\wedge}6,0,1/(A*\Delta\tau^{\wedge}n\ )*LN((a_f-(D/B*\Delta\tau^{\wedge}n)))/a_t-(\ B*\Delta\tau^{\wedge}n))))))$$

$$Nf_{(t)} = n_{s1}+ n_{s2}+ n_{s3} + n_{st} + n_{p1}$$

....

$$a_{s1} = \text{IF}(n_1>n_{s1},\alpha*d,$$

$$\text{IF}(n_1< n_{s1},d-((d-a_o)/(EXP(n_1*A*\Delta\tau^{\wedge}m))),\ d-((d-a_o)/(EXP(n_{s1}*A*\Delta\tau^{\wedge}m)))))$$

$$a_{s2} = \text{IF}(n_1>n_{s1},0$$

$$\text{IF}(a_{s1}<\alpha*d,0$$

$$\text{IF}(n_1-n_{s1}<n_{s2},(d+d_m)-(((d+d_m-\alpha*d))/(EXP((n_1-n_{s1})*A*\Delta\tau^{\wedge}m)))-a_{s1},$$

$$(((d-d_m)-\ (((d+d_m-\alpha*d))/(EXP((n_{s2})*A*\Delta\tau^{\wedge}m)))-a_{s1})))$$

$$a_{sith} = \text{IF}(at<d,0,$$

$$\text{IF}(a_{s1}<\alpha*d,0,$$

$$\text{IF}(n_1<=n_{s1}+n_{s2},0$$

$$\text{IF}(n_1-n_{s1}-n_{s2}<n_{sith},((d+2*d_m)-((d+2*d_m-(d+\alpha*d_m))/(EXP((n_1-n_{s1}-$$

$$n_{s2})*A*\Delta\tau^{\wedge}m)))/INT((a_t-d-d_m)/d_m)))-a_{s1}-a_{s2})+(INT((a_t-d-2*d_m)$$

$$/(d_m)*d_m*((n_1-n_{s1}-n_{s2})/n_{sith})),((d+2*d_m)-((d+2*d_m)-(d+\alpha*d))$$

$$/(EXP((n_{sith}*A*\Delta\tau^{\wedge}m)))/INT((at-d-d_m)/d_m))))-a_{s1}-a_{s2}$$

$$+INT((a_t-d-d_m)/(d_m)*d_m)))))$$

$$a_{st} = \text{IF}(n_1<n_{s1}+n_{s2}+n_{sith},0,$$

IF($a_{s1} < \alpha * d$, 0,

 IF($a_t < d$, $(d + d_m - (d + d_m - \alpha * d) / (EXP(n_{st} * A * \Delta\tau^\wedge m))) - a_{s1}$,

 INT($(a_t - d_m + d + d_m - (a_{s1} + a_{s2} + a_{sith})) / (EXP((n_{st} * A * \Delta\tau^\wedge m)))$))))

a_{p1} = IF($n_1 < n_{s1} + n_{s2} + n_{sith} + n_{st}$, 0.($a_t - (C/B * \tau^\wedge n)))*EXP(((n_1 - n_{s1} - n_{s2} - n_{sith} - n_{st})$

 $*(B*(\Delta\tau^\wedge n))) + (C/B * \Delta\tau^\wedge n)) - (a_{s1} + a_{s2} + a_{sith} + a_{st}))$

a_{1total} = $a_{s1} + a_{s2} + a_{sith} + a_{st} + a_{p1}$

....

a_{2s1} = IF($a_{1total} >= 3000$, 0,

 IF($a_{1total} >= \alpha * d$, 0,

 IF($a_{1total} = 0$, $d - ((d - a_o) / (EXP(W28 * A * \Delta\sigma^\wedge m)))$,

 IF($a_{1total} < \alpha * d$, 0, $d - ((d - a_{1total}) / (EXP(W28 * A * \Delta\sigma^\wedge m)))$)))))

W28 = IF($n_{2s1} > n_2$, n_{2s1}, n_2

a_{2s2} = IF($a_t < d + \alpha * d_m$, 0,

 IF($a_{1total} >= 3000$, 0,

 IF($a_t < d$, 0,

 IF($a_{1total} + a_{2s1} > d + d_m$, 0,

 IF($a_{2s1} = 0$, $(d + d_m) - (((d + d_m - a_{1total})) / (EXP((X48 * A * \Delta\sigma^\wedge m)))) - a_{1total}$,

 IF($a_{2s1} < \alpha * d$, 0, $(d + d_m) - (((d + d_m - \alpha * d_m)) / (EXP((n_2 - n_{2s1})$

IV

$$* A*\Delta\sigma\char`\^m)))-a_{2s1})))))))$$

$$X28 = IF(a_{1total} + a_{2s1} > d + d_m, 0,$$

$$IF(n_2 > n_{2s1} + n_{2s2}, n_{2s1}$$

$$IF(n_2 > n_{2s1} + n_{2s2}, 0, 1/(A*\Delta\sigma\char`\^m)*LN((d+d_m-(a_{1total})/((d+d_m)-(d+\alpha*d_m)))))))))$$

$$a_{2ith} = IF(n_2 < X48, 0,$$

$$IF(a_t < d + \alpha*d_m, 0,$$

$$IF(a_{2s1} + a_{2s2} = 0, ((d+2*d_m)-((d+2*d_m))/(EXP((Y48*A*\Delta\sigma\char`\^m)))$$

$$- a_{1total} - a_{2s1} - a_{2s2}),$$

$$IF(n_2 < X48 + Y48, ((d+2*d_m)-(EXP((Y48*A*\Delta\sigma\char`\^m)))-a_{2s1}-a_{2s2}- a_{1total})$$

$$*INT((at-d-d_m)/d_m), 0, ((d+2*d_m)-((d+2*d_m-(d+\alpha*d)$$

$$/(EXP((Y48)*A*\Delta\sigma\char`\^m)))-a_{2s1}-a_{2s2}- a_{1total})*INT(a_t-d-d_m)d_m))))))$$

$$Y28 = IF(a_{1total}+a_{2s1}+a_{2s2} > d + \alpha*d, 0, (1/(A*\Delta\sigma\char`\^m))LN((d+2*d_m)-(a_{1total} -a_{2s2}))$$

$$/((d+2*d_m)-(d+d_m+\alpha*d_m))))$$

$$a_{2t} = IF(a_{2s1}+a_{1total} < \alpha*d, D-((d-a_o)/EXP(Z48**A*\Delta\sigma\char`\^m)))$$

$$IF(a_{1total} >= 3000, 0,$$

$$IF(a_{1total} > a_t, 0,$$

$$IF(n_2 > X48 + Y48, ROUNDUP((a_t-d)/d_m, 0)*d+d_m- a_{1total} -a_{2s1}-a_{2s2}-a_{2ith})$$

$$/(EXP((Z48*A*\Delta\sigma\char`\^m)))- a_{1total},$$

$$IF(a_{1total} +a_{2s1}+a_{2s2}+a_{2ith} < a_t, 0, INT((a_t-d_m)d_m)*d_m+d-(INT((a_t-d_m)d_m)$$

$$*d_m+d+d_m-(\alpha*d_m+INT(a_t-d)/EXP((n_{2ith})*A*\Delta\sigma\char`\^m)))))))))$$

$Z28 = IF(at< a_{1total} +a_{2s1}+a_{2s2}+a_{2ith},0,$

$\quad IF(a_{2s1}+ a_{1total}<\alpha*d,1/(A*\Delta\sigma^{\wedge}m)*LN(d-ao)/(d-at)$

$\quad\quad IF(at<\alpha*d,1/(A*\Delta\sigma^{\wedge}m)*LN((d+d_m-\alpha*d)/(d+d_m-a_t))),$

$\quad\quad 1/(A*\Delta\sigma^{\wedge}m)*LN(((INT((at-d)/d_m)*d_m+d+d_m- a_{1total} -a_{2s1}-a_{2s2}-a_{2ith}))$

$\quad\quad /INT((a_t-d(/d_m)*d_m+d+d_m-a_t)))))))$

$a_{2p} = IF(\sigma<580,0,$

$\quad IF(a_{1total}>at,(a_{1total}-(D/B*\sigma^{\wedge}n)))*EXP(((n_2* B*\Delta\sigma^{\wedge}n))-(a_{2s1}+a_{2s2}+a_{sith}+a_{2t}),$

$\quad (a_t-(D/B*\sigma^{\wedge}n)))*EXP(((n_2*W48-X48-Y48-Z48)*(B*\sigma^{\wedge}n)+ (D/B*\Delta\sigma^{\wedge}n))$

$\quad -(a_{2s1}+a_{2s2}+a_{2ith}+a_{2t}))))$

$a_{2total} = a_{2s1}+a_{2s2}+a_{2sith}+a_{2st}+a_{2p}$

....

$n_{3s1} = IF(a_{2total}<\alpha*d,0,$

$\quad IF(a_{2total}=0, 1/(A*\Delta\tau^{\wedge}m)*LN((d-a_o)/(d-\alpha*d))),1/(A*\Delta\tau^{\wedge}m)$

$\quad *LN((d- a_{2total})/(d-\alpha*d)))))$

$n_{3s2} = IF(a_{2total}>a_t,0,$

$\quad IF(at<\alpha*d,0,$

$\quad\quad IF(a_{2total}>d+\alpha*d,0,$

$\quad\quad\quad IF(a_{2total}>\alpha*d,1/(A*\Delta\tau^{\wedge}m)*LN((d+d_m)- a_{2total})/((d+d_m)-(d+\alpha*d_m))),$

$\quad\quad\quad 1/(A*\Delta\tau^{\wedge}m)*LN(((d+d_m)- (\alpha*d))/((d+d_m)-(d+\alpha*d_m)))))))$

n_{3sith} = IF(a_t<d,0,

IF(a_{2total}>=a_t,0,

IF(a_{2total}>INT(((at-d/d_m)*d_m+α*d_m,0,

IF(a_{2total}>=d+α*d_m,1/(A*$\Delta\tau$^m)*LN((ROUNDUP((a_{2total} -d)/d_m),0)

d_m+d+d_m- a_{2total})/((ROUNDUP((a_{2total} -d)/d_m,1)d_m+d+d_m-

(ROUNDUP((-d)/d_m,1)*d_m+d+α*d_m)))+1/(A*$\Delta\tau$^m)*LN((d+3*d_m)-

(d+d_m+α*d_m))/((d+3*d_m)-(d+2*d_m+α*d_m)+INT((a_t-d-3*dm)/d_m,

1/(A*$\Delta\tau$^m)*LN((d+2*d_m)-(d +α*d_m))/((d+2*d_m)-(d +d_m+α*d_m)))

*INT((at-d-d_m)d_m)))))

n_{3st}= IF(a_{2total}>=a_t,0,

IF(a_{2total}>INT((a_t-d)/d_m+d, 1/(A*$\Delta\tau$^m)*LN((INT((a_t-d)/d_m)*d_m

+d+d_m-a_{2total})/ INT((a_t-d)/d_m)*d_m+d+d_m-a_t))), 1/(A*$\Delta\tau$^m)*LN

((INT((a_t-d)/d_m)*d_m+d+d_m-(INT((a_t-d)/d_m)*d_m+d+d_m-d_m+αd_m))

/ INT((a_t-d)/d_m)*d_m+d+d_m-a_t))))))

n_{3p} = IF(a_{2total}>=a_f,0,

IF(a_{2total}>a_t,1/(B*$\Delta\tau$^n)))*LN((a_f-(D/B*$\Delta\tau$^n)))/(a_{2total} -(D/B*$\Delta\tau$^n))))),

(1/(B*$\Delta\tau$^n)))*LN((a_f-(D/B*$\Delta\tau$^n)))/(a_t-(D/B*$\Delta\tau$^n)))))))

$N_{f3(t)}$ = n_{3s1}+ n_{3s2}+ n_{3sith} + n_{3st} + n_{3p1}

VII

A = 1.800E-39
B = 6.523E-27
C = 3.74E-03
n = 8.129
m = 13.4
β = 0.59
ϕ = 0.79
d_1 = 29 μm
d_2 = 6 μm
α = 0.95
a_o = 2 μm
a_f = 4000 μm

$\Delta\tau_1$ (MPa)	n_{s1}	n_{s2}	n_{sith}	n_{st}	n_{sp}	N_f	a_t
530	508	557	528	731	71342	7.367E+04	46.9
495	1268	1393	7919	1706	125775	1.381E+05	76.9
460	3387	3720	52891	5783	277895	3.437E+05	131.0
435	7161	7866	208761	8398	367290	5.995E+05	208.8
425	9780	10743	356372	11452	450743	8.391E+05	250.8
415	13456	14780	616389	13977	524958	1.184E+06	304.7
410	15829	17387	807494	17198	596567	1.454E+06	334.7
385	36777	40398	3292845	32761	950278	4.353E+06	556.5

$\Delta\sigma$ (MPa)	n_{s1}	n_{s2}	n_{sith}	n_{st}	n_{sp}	N_f	a_t
820	0	0	0	229	16587	1.682E+04	10.40
760	0	0	0	1308	33170	3.448E+04	16.51
700	14941	16412	0	5878	57014	9.425E+04	33.01
680	22033	24203	0	11600	77610	1.354E+05	39.65
640	49647	54535	206752	23794	129939	4.647E+05	63.45
620	75972	83452	553670	36461	171720	9.213E+05	81.45
600	117889	129496	1350106	61275	232073	1.891E+06	105.62
580	185680	203962	3286364	42168	280497	3.999E+06	139.76

**Computed results for push-pull and torsion
(constant amplitude loading)**

Appendix 5

CRACK LENGTHS FOR n_1 VALUE							
n_1 / N_{f1}	a_{s1}	a_{s2}	a_{sith}	a_{st}	a_{sp}	$a_{1\ TOTAL}$	$\Delta\tau_1$(MPa)
0.22	27.55	7.15	106.44	0.00	0.00	141.14	410
0.33	27.55	7.15	164.47	0.00	0.00	199.17	410
0.53	27.55	7.15	269.00	0.00	0.00	303.70	410
0.73	27.55	7.15	294.00	6.04	38.80	373.53	410
0.22	27.55	7.15	106.44	0.00	0.00	141.14	410
0.33	27.55	7.15	164.47	0.00	0.00	199.17	410
0.53	27.55	7.15	269.00	0.00	0.00	303.70	410
0.73	27.55	7.15	294.00	6.04	38.80	373.53	410

CRACK LENGTHS FOR n_2 VALUE							
n_2 / N_{f2}	a_{2s1}	a_{2s2}	a_{2tith}	a_{2t}	a_{2p}	$a_{2\ TOTAL}$	$\Delta\sigma_1$(MPa)
0.04	0	0	0	0	652.71	793.86	600
0.04	0	0	0	0	1524.67	1723.84	600
0.04	0	0	0	0	3095.29	3398.99	600
0.04	0	0	0	0	3626.47	4000.00	600
0.04	0	0	0	0	305.97	447.11	640
0.04	0	0	0	0	484.77	683.94	640
0.04	0	0	0	0	806.83	1110.53	640
0.04	0	0	0	0	1022.00	1395.53	640

n_{3s1}	n_{3s2}	n_{3sith}	n_{3t}	n_{3p}	N_{3f}	a_{3TOTAL}	$\Sigma n/N_f$
0	0	0	0	182826	1.828E+05	4000	0.386
0	0	0	0	85557	8.556E+04	4000	0.429
0	0	0	0	15804	1.580E+04	4000	0.581
0	0	0	0	0	0.000E+00	4000	0.770
0	0	0	0	304696	3.047E+05	4000	0.469
0	0	0	0	206748	2.067E+05	4000	0.512
0	0	0	0	136811	1.368E+05	4000	0.664
0	0	0	0	109297	1.093E+05	4000	0.845

Computed results for multi-phase loading
$\Delta\sigma$ (600 MPa and 640 MPa)

Appendix 6

	CRACK LENGTHS FOR n_1 VALUE						
n_1 / N_{f1}	a_{s1}	a_{s2}	a_{sith}	a_{st}	a_{sp}	$a_{1\ TOTAL}$	$\Delta\tau_1$(MPa)
0.22	27.55	7.15	106.44	0.00	0.00	141.14	410
0.33	27.55	7.15	164.47	0.00	0.00	199.17	410
0.53	27.55	7.15	269.00	0.00	0.00	303.70	410
0.73	27.55	7.15	294.00	6.04	38.80	373.53	410
0.22	27.55	7.15	106.44	0.00	0.00	141.14	410
0.33	27.55	7.15	164.47	0.00	0.00	199.17	410
0.53	27.55	7.15	269.00	0.00	0.00	303.70	410
0.73	27.55	7.15	294.00	6.04	38.80	373.53	410
	CRACK LENGTHS FOR n_2 VALUE						
n_2 / N_{f2}	a_{2s1}	a_{2s2}	a_{2tith}	a_{2t}	a_{2p}	$a_{2\ TOTAL}$	$\Delta\sigma_1$(MPa)
0.04	0	0	0	0	191.66	332.81	760
0.04	0	0	0	0	273.00	472.17	760
0.04	0	0	0	0	419.50	723.20	760
0.04	0	0	0	0	517.37	890.91	760
0.04	0	0	0	0	188.59	329.73	820
0.04	0	0	0	0	267.35	466.52	820
0.04	0	0	0	0	409.20	712.90	820
0.04	0	0	0	0	503.97	877.50	820

n_{3s1}	n_{3s2}	n_{3sith}	n_{3t}	n_{3p}	N_{3f}	a_{3TOTAL}	$\Sigma n/N_f$
0	0	0	11487	596567	6.081E+05	4000	0.678
0	0	0	0	287505	2.875E+05	4000	0.568
0	0	0	0	197443	1.974E+05	4000	0.706
0	0	0	0	166026	1.660E+05	4000	0.884
0	0	0	16227	596567	6.128E+05	4000	0.681
0	0	0	0	291101	2.911E+05	4000	0.570
0	0	0	0	199791	1.998E+05	4000	0.707
0	0	0	0	168164	1.682E+05	4000	0.886

Computed results for multi-phase loading
$\Delta\sigma$ (760 MPa and 820 MPa)

Appendix 7